Western Graduate&PostdoctoralStudies

Western University
Scholarship@Western

Electronic Thesis and Dissertation Repository

4-13-2022 2:00 PM

Plasmonically-Active Nanomaterials for Enhanced Second-Harmonic Generation and Chemical Reactions

Denis AB Therien, *The University of Western Ontario*

Supervisor: Lagugné-Labarthet, François, *The University of Western Ontario*

A thesis submitted in partial fulfillment of the requirements for the Doctor of Philosophy degree in Chemistry

© Denis AB Therien 2022

Follow this and additional works at: https://ir.lib.uwo.ca/etd

Part of the Physical Chemistry Commons

Recommended Citation

Therien, Denis AB, "Plasmonically-Active Nanomaterials for Enhanced Second-Harmonic Generation and Chemical Reactions" (2022). *Electronic Thesis and Dissertation Repository*. 8536.
https://ir.lib.uwo.ca/etd/8536

This Dissertation/Thesis is brought to you for free and open access by Scholarship@Western. It has been accepted for inclusion in Electronic Thesis and Dissertation Repository by an authorized administrator of Scholarship@Western. For more information, please contact wlswadmin@uwo.ca.

Abstract

Upon excitation by an electromagnetic field, metallic nanomaterials will produce highly localized areas of electromagnetic enhancement, a phenomenon known as localized surface plasmon resonance (LSPR), which can be applied to a variety of techniques including second-harmonic generation (SHG) and surface chemistry. These tunable LSPRs can be modelled prior to fabrication by finite-difference time-domain (FDTD) calculations and observed experimentally by SHG microscopy (SHGM). In this thesis, two types of nanomaterials were characterized using SHGM: plasmon-active dendritic fractals (dendrimers) and transition-metal dichalcogenides (TMDs). Dendrimers with specific geometries and LSPRs were used to demonstrate how nanomaterial symmetry affects SHG as well as how local non-centrosymmetric instances can induce SHG responses in otherwise forbidden circumstances. This introduces an in-depth analysis on the effects of plasmon active dendrimers with specific geometries, and how to enhance their nonlinear optical properties. TMDs were analyzed using polarization-dependent SHG and were subsequently functionalized with an organic dye to visualize its effect on the SHG signal. Commercial applications of nonlinear optical processes from plasmonic metamaterials or crystalline materials open a wealth of applications in fiber-optic communications, sensing in biology, photonics filters as well as efficient light conversion and tuning.

Laser-induced periodic surface structures (LIPSS) are generated upon irradiation at the surface of a material with repeating features. Reported in this thesis are LIPSS created on glass with a single wavelength, followed by substrates prepared by nanosphere

lithography, and the effects of the structure shape and size by the resulting LSPRs was analyzed. Crosshair structures were also computationally modelled and fabricated to exhibit up to three distinct LSPRs in the visible spectral region and irradiated at three distinct wavelengths and two polarizations. The resulting grafting patterns were compared to the FDTD-modelled hotspots, which demonstrated three different grafting patterns at both incident polarizations. These could lead to applications such as surface specific and polarization dependent diagnostic tools, variable gratings on a single substrate, multi-coloured nanoemitters, and more.

Keywords

Plasmonics, second-harmonic generation, localized surface plasmon resonances, hot electrons, finite-difference time-domain, metamaterials, electron-beam lithography, polarization-dependent plasmon mediated chemistry, dye-sensitized transition-metal dichalcogenides, laser-induced periodic surface structures

Summary for Lay Audience

Nanomaterials are structures with dimensions comparable to the size of light waves. These materials are known to interact efficiently with a field of light. Through a variety of fabrication techniques, these materials can be made to interact with light of a specific color up to a multitude of colors, depending on the features and sizes of the designed material, generating what is known as plasmons. These nanomaterials can then be employed to improve existing analytical techniques to allow the characterization of minute details at their surfaces.

While there are many light-based techniques to characterize materials, in this thesis we are particularly interested by a two-photon process known as second-harmonic generation. This technique has a selection rule that makes it forbidden in materials that have a center of inversion. Herein, we study how plasmons affect the second-harmonic generation output of materials with specific geometries. The study of a two-dimensional material, which are a category of materials that are approximately 1 nm thick, or $1/70{,}000^{th}$ of a human hair, is also studied. A dye is then added to this two-dimensional material to study its effects. By studying and improving these properties, light-based applications, such as fiber optic communications and polarization sensing techniques, can be optimized.

Furthermore, when a field of light excites these plasmons, they can interact with molecules at the surface of the nanomaterials to induce chemical reactions. These materials are designed in such a way to generate patterns at the surface using different shapes and features when fabricating the materials. This would allow the production of large surfaces with potential applications in biological trapping and diagnostic tools that require smaller sample sizes and higher densities of light-emitting surface areas are possible.

Co-Authorship Statement

Prof. François Lagugné-Labarthet was the corresponding author on the manuscripts presented in this thesis and was responsible for the tutelage and supervision Denis A.B. Therien received during his studies. This thesis includes three publications, all of which had contributions from co-authors.

Denis A.B. Therien was the primary author on the papers presented in Chapters 4, 6, and 7. He was responsible for the modelling, acquisition, and processing of most of the experimental work in the papers, as well as writing and revision for any necessary drafts. Throughout this work, data was additionally acquired and analyzed by co-authors as summarized below:

Chapter 4:

Therien, D.A.B.; Hou, R.; Lagugné-Labarthet, F. Second-Harmonic Generation from Dendritic Fractal Structures. *Plasmonics*, **2020**, *15*, 507-515.

Dr. Renjie Hou was responsible for the SHG data acquired and used in Figure 1, as well as the conception and assembly of the SHG microscope used by Denis A.B Therien during his studies. Therien. Denis A.B. Therien was responsible for the remaining FDTD modelling and SHG image acquisition and processing.

Chapter 5:

The AFM and Raman data present in this Chapter were acquired and analysed by Pooneh Farhat of the FLL group. Denis A.B. Therien was responsible for the SHG measurements, functionalization, and PD-SHG measurements in this Chapter.

Chapter 6:

Therien, D.A.B.; Ćulum, N. M.; McRae, D. M.; Mazaheri, L.; Lagugné-Labarthet, F. Single-Beam Inscription of Plasmon-Induced Surface Gratings. *Opt. Mater.*, **2021**, *112*, 110775.

Nina M. Ćulum was responsible for the acquisition and analysis of the AFM images, Dr. Danielle M. McRae assisted with the FDTD modelling, and Dr. Leila Mazaheri was co-corresponding author on this paper and assisted with the conception of the manuscript. Denis A.B. Therien developed the experimental procedure, and carried out the substrate fabrication, experiments and SEM imaging presented.

Chapter 7:

Therien, D.A.B.; McRae, D. M.; Mangeney, C.; Félidj, N.; Lagugné-Labarthet, F. Three-Color Plasmon-Mediated Reduction of diazonium Salts Over Metasurfaces. *Nanoscale Adv.*, **2021**, *3*, 2501-2507.

Dr. Danielle M. McRae assisted with the FDTD modelling presented in this paper. Prof. Claire Mangeney and Prof. Nordin Félidj assisted with the theoretical concepts, discussions, and editing of the manuscript. Denis A.B. Therien designed, fabricated, and tested the metastructures used in this paper.

Acknowledgments

First and foremost, I would like to acknowledge my supervisor, Professor François Lagugné-Labarthet. Under his mentorship, I was able to push myself harder and further than I originally thought possible. With his tutelage, I was able to publish multiple papers and gain confidence in myself as a scientist. He has both taught and challenged me more than anyone ever has, helping me to improve my work and dramatically raising my standards as a writer, experimentalist, and collaborator. I'll always remember one of my favourite phrases from our group meetings: "we are not making waffles on the beach here." For this, he has my enduring gratitude.

Next, I would like to sincerely thank my lab mates and colleagues. I have had many fruitful discussions with members of the FLL group, including Dr. Gregory Wallace, Dr. Danielle McRae, Dr. Renjie Hou, Dr. Leila Mazaheri, Dr. Joachim Jelken, Sydney Legge, Nina Culum, Olivia Aviles, Pooneh Farhat, and Lauren Katz. Particularly, Dr. Wallace, Dr. McRae, and Dr. Hou for teaching me techniques and writing skills that were pivotal to the completion of my degree. The frequent coffee break discussions over Einstein's, board game nights, and group hangouts were crucial to keeping me going during my degree, and I will forever cherish the memories created during my time at Western. A particular thanks to Jonathan Adsetts, who taught me to always keep my eyes open and my head up, especially when in a pool to avoid swimming straight into a wall.

I would like to thank the members of Western's Nanofabrication Facilities, Tim Goldhawk and Dr. Todd Simpson. Dr. Simpson trained me on nanofabrication techniques, while Tim Goldhawk trained me on a variety of surface preparation techniques. They were always around to have both technical and amicable discussions about both research and life. I would also like to thank Dr. Ian Burgess, Dr. Stuart Reid and Dr. Scott Rosendahl of the Canadian Light Source in Saskatoon, SK, Canada. Their help with the mid-infrared spectral range beam line projects was greatly appreciated.

I'd also like to thank my family. My grandmother, Joan O'Malley; late grandparents, Brian O'Malley, Lionel and Aline Therien; aunt and uncle, Kathy and James O'Malley;

and my parents, Denis and Kelly Therien; whose love and support has kept me going these past few years. I'd also like to thank my brothers, Daniel and Michael Therien, with whom I had long discussions about science and various arbitrary topics that kept my spirits up and my mind sharp.

Lastly, I am forever grateful to my wonderful fiancée, Nina Ćulum. Her love, support, proofreading skills, and patience has helped me through some of the best and some of the most difficult parts of my both academic career and personal life.

Table of Contents

Abstract i

Summary for Lay Audience iii

Co-Authorship Statement iv

Acknowledgments vi

Table of Contents viii

List of Figures xii

List of Abbreviations, Symbols, and Nomenclature xxiii

List of Appendices xxvii

Chapter 1 1

1 General Introduction 1

1.1 Applications of Plasmons 1

1.1.1 Plasmon-Enhanced Nonlinear Optics 2

1.1.2 Plasmon-Mediated Chemistry at the Nanoscale 5

1.2 Scope of Thesis 6

1.3 References 8

Chapter 2 11

2 Linear and Nonlinear Optical Properties of Plasmonic Nanomaterials 11

2.1 Plasmonically Active Materials 11

2.1.1 Surface Plasmon Resonances (SPRs) 12

2.1.2 Localized Surface Plasmon Resonances 14

2.1.3 Metamaterials 16

2.2 FDTD Electromagnetic Modelling 17

2.3 Second-Harmonic Generation 20

2.3.1 Principles of SHG 20

2.3.2 SHG in Nanomaterials 23
2.3.3 Plasmon-Enhanced SHG 26
2.4 Plasmon-Mediated Chemistry 26
2.4.1 The Hot Electron and Thermal Energy Decay of LSPRs 27
2.4.2 Selective Surface Chemical Reactions Using Hot Electrons 28
2.5 Summary 33
2.6 References 34
Chapter 3 41
3 Methodology 41
3.1 Finite-Difference Time-Domain (FDTD) Modelling 41
3.2 Fabrication Methods 44
3.2.1 Nanosphere lithography 44
3.2.2 Electron-Beam Lithography 46
3.2.3 Chemical Vapour Deposition 50
3.3 Characterization Methods 51
3.3.1 Scanning Electron Microscopy 51
3.3.2 Visible-Near Infrared Absorbance Spectroscopy 52
3.4 SHG Microscopy 53
3.5 Metamaterial Characterization 55
3.5.1 Characterizing LSPRs in Metamaterials 55
3.5.2 Tuning LSPRs in Metamaterials 58
3.6 Surface Functionalization 62
3.6.1 Single-Beam Grafting 62
3.7 Summary 63
3.8 References 63

Chapter 4 66
4 Second-Harmonic Generation from Dendritic Fractals 66
4.1 Introduction 66
4.2 Methods 68
4.3 Results and Discussion 69
4.3.1 Shape and symmetry dependence on second harmonic generation. 69
4.4 SHG mapping of C_3, C_4 and C_5-symmetry dendritic structures 70
4.4.1 Fractal structure with C_3 symmetry 72
4.4.2 Structures with C_4 symmetry 74
4.4.3 Structures with C_5 symmetry 75
4.5 Conclusion 78
4.6 References 79
Chapter 5 81
5 Enhancing the SHG Response in 2D MoS_2 Flakes 81
5.1 Introduction to Transition-Metal Dichalcogenides 81
5.1.1 SHG in TMDs 81
5.2 Methods 82
5.3 Calculating the MoS_2 Polarization-Dependent SHG Signal 83
5.4 Characterization of MoS_2 Flakes 87
5.5 SHGM of Functionalized MoS_2 Flakes 90
5.6 Conclusion 93
5.7 References: 94
Chapter 6 97
6 Single-Beam Inscription of Plasmon-Induced Surface Gratings 97
6.1 Introduction 97

6.2 Experimental 99
6.3 Results and Discussion 99
6.3.1 Single-beam Inscriptions on Bare Glass 102
6.3.2 Single-Beam Inscriptions on Gold Nanoprisms 105
6.4 Conclusion 111
6.5 References 111
Chapter 7 114
7 Three-Color Plasmon-Mediated Reduction of Diazonium Salts over Metasurfaces. 114
7.1 Introduction 114
7.2 Materials and Methods 116
7.3 Results and Discussion 116
7.3.1 FDTD Modelling 116
7.3.2 Characterization and Functionalization 118
7.3.3 Irradiation at 800 nm 120
7.3.4 Irradiation at 632.8 nm 123
7.3.5 Irradiation at 532 nm 125
7.4 Conclusion 129
7.5 References 129
Chapter 8 132
8 Conclusions and Outlook 132
8.1 References 135
Appendix A: Copyrights and Permissions 137
Curriculum Vitae 144

List of Figures

Figure 1-1 The number of publications with "plasmon" as a keyword from 1960 to 2021. Data was acquired from webofknowledge.com using the keyword “plasmon”. 1

Figure 1-2 (a) The SHG intensity for the hybrid ZnO silver mushroom array (HZSMA), the ZnO particles on Au, and the silver mushroom array (SMA) for different fundamental wavelengths. The values were normalized to the most intense SHG signal, and the red values were multiplied by a factor of 100 for visibility, reprinted from Shen, S.; Yang, W.; Shan, J.; Sun, G.; Shih, T.-M.; Zhou, Y.; Yang, Z., J. Chem. Phys. 2020, 153, 151102., with the permission from AIP Publishing; (b) an optical image of artificially stacked MoS_2 flakes with (c) the corresponding SHGM image, reprinted (adapted) with permission from Hsu, W.-T.; Zhao, Z.-A.; Li, L.-J.; Chen, C.-H.; Chiu, M.-H.; Chang, P.-S.; Chou, Y.-C.; Chang, W.-H., ACS Nano 2014, 8, 2951-2958. Copyright 2014 American Chemical Society; SEM images of mesoscale flower-like Ag particles after (d) a 120 s synthesis and (e) a 180 s synthesis, reprinted from Cheng, Z.-Q.; Li, Z.-L.; Luo, X.; Shi, H.-Q.; Luo, C.-L.; Liu, Z.-M.; Nan, F., Appl. Phys. Lett. 2019, 114, 011901.], with the permission from AIP Publishing..... 4

Figure 1-3 Transmission electron microscopy (TEM) images of a TEM grid (top), and Au nanoparticles before and after irradiation in the presence of the acrylate monomer, reprinted (adapted) with permission from Kameche, F.; Heni, W.; Telitel, S.; Vidal, L.; Marguet, S.; Douillard, L.; Fiorini-Debuisschert, C.; Bachelot, R.; Soppera, O., J. Phys. Chem. C 2021, 125, 8719-8731. Copyright 2021 American Chemical Society..... 6

Figure 2-1 A schematic of the electric field generated by the SPR. 13

Figure 2-2 Complex dielectric constant for a) Au (black) and Ag (red) and b) Cu (blue) and Al (green), as calculated by the Drude-Lorentz model.[2]..... 14

Figure 2-3 Schematic oscillation of the electric field around an Au nanosphere. 14

Figure 2-4 Far field extinction spectra for a gold nanodisk with a diameter of 280 nm with the near field enhancement maps inset showing the quadrupolar and dipolar LSPRs

present at 775 and 930 nm, respectively. Reprinted (adapted) with permission from Butet, J.; Brevet, P.-F.; Martin, O. J. F., ACS Nano 2015, 9, 10545-10562. Copyright 2015 American Chemical Society. 15

Figure 2-5 A series of SEM images of metamaterials known as dendritic fractals. (a) A three-branched generation 2 fractal, (b) a four-branched generation 2 fractal, and (c) a five-branched generation 2 fractal. 17

Figure 2-6 Illustration of a Yee cell, including the distribution of the magnetic (H) field (blue) and the electric (E) field (red) pointing vectors throughout the cell. 19

Figure 2-7 (a) An SEM image of a Fischer patterned substrate produced by NSL and (b) an SHGM image of a large surface area of an NSL substrate. 24

Figure 2-8 (a) Schematic of a bianisotropic metamolecule in which electromagnetic coupling could happen. The four Au nanodisks, each with radius of 50nm and a thickness of 30nm are symmetric along the y-axis asymmetric along the x-axis. Light is incident from the top of the metamaterial and the electric field polarizes along the x- or y-axis. (b) Linear scattering cross-section (SCS) of the metamolecule at the fundamental frequency under normal incident light with x- (black line) and y- (red line) polarization. The red arrow denotes the wavelength of the electromagnetic coupling under x-polarization. (c) Normalized electric and magnetic near-field distributions at the fundamental frequency denoted by the red arrow in (b). Top panels: x-polarization; bottom panels: y-polarization. © 2018 WILEY-VCH Verlag GmbH & Co. KGaA, Weinheim. 25

Figure 2-9 Multipolar emission from perfect nanospheres. (a) Experimental evidence of the SH quadrupolar emission from 150 nm gold nanoparticles and (b) the corresponding FDTD-calculated near-field enhancement intensity. Reprinted (adapted) with permission from Butet, J.; Brevet, P.-F.; Martin, O. J. F., ACS Nano 2015, 9, 10545-10562. Copyright 2015 American Chemical Society. 26

Figure 2-10 Illustration of the three stages of the non-radiative decay of an LSPR. At t = 0 is the irradiation of the nanoparticle, followed by t = 1 to 100 fs where in the charge

carriers are excited, t = 100 fs to 1 ps where the charger carriers relax, and finally t = 1 – 1000 ps the thermal dissipation..... 28

Figure 2-11 Imaging electron emission from plasmonic nanoantennae with PMMA. (a) Top-down SEM micrograph of a 260 nm pitch Au nanorod array coated with a 20 nm thick layer of PMMA. The coated array was previously exposed to $\sim 10^9$ fs laser pulses and the PMMA was subsequently developed. (b) SEM micrograph of a nanorod antenna near the periphery of the exposed region shown in panel (a) where regions of exposed and developed PMMA at the poles of the nanoantenna are visible. (c) SEM micrograph of a pole of a nanorod near the center of the exposed region in panel (a). A narrow strip of material believed to be cross-linked PMMA is present at the apex of the nanorod. (d, e) SEM micrographs of exposed PMMA around nanotriangles illuminated with $\sim 10^9$ fs laser pulses. The polarization of these pulses was aligned(d) parallel to and (e) orthogonal to the long-axis of the nanotriangle antennae. Reprinted (adapted) with permission from Hobbs, R. G.; Putnam, W. P.; Fallahi, A.; Yang, Y.; Kärtner, F. X.; Berggren, K. K., Nano Lett. 2017, 17, 6069-6076. Copyright 2017 American Chemical Society..... 29

Figure 2-12 Topographic an optical characterization of a nanodisk-based two color anisotropic nanoemitter. (a) Schematic representation of the nanostructure. (b) SEM image of the Au nanodisk with a diameter of 90 nm after the first exposure that positions green QDs along the x-axis. (c) SEM image of the same nanodisk after the second exposure that traps red QDs along the y-axis. The respective plasmonic near-field intensities of the dipole emission for (b) and (c) are shown in each inset. For clarity, SEM images have been artificially colored according to the emission wavelengths of the trapped QDs. Far-field fluorescence image of the two-colour anisotropic nanoemitters (TCANE) under illumination with (d) x-axis polarization and (e) y-axis polarization. Double arrows represent the polarization of the excitation light. (f) Polarization-dependent fluorescence spectra from the TCANE. The polarizations of the excitation light (λ_{exc} = 405 nm) were at θ=0° (red plot), 22.5° (orange plot), 45° (green plot), 67.5° (blue plot), and 90° (black plot) with respect to the y-axis. The inset defines the polarization angle θ, where the dashed line represents the incident polarization direction. Reprinted (adapted) with permission from Zhou, X.; Wenger, J.; Viscomi, F. N.; Le

Cunff, L.; Béal, J.; Kochtcheev, S.; Yang, X.; Wiederrecht, G. P.; Colas des Francs, G.; Bisht, A. S.; Jradi, S.; Caputo, R.; Demir, H. V.; Schaller, R. D.; Plain, J.; Vial, A.; Sun, X. W.; Bachelot, R., Nano Lett. 2015, 15, 7458-7466. Copyright 2015 American Chemical Society. 31

Figure 2-13 SEM images of a single nanoparticle after plasmon-induced grafting of (a) carboxyphenyl layers along the Y axis and (c) additional hydroxyethyl phenyl layers along the X direction. Irradiation conditions: λ_{inc} = 633 nm, 180 seconds with a power of P=0.8 mW/μm^2. Mapping of the near field intensity enhancement $|E|^2$ upon irradiation along the Y axis (b) and both X and Y axis (d), on a unit cell nanodisk of 100 nm, H = 50 nm, using the DDA method. 33

Figure 3-1 (a) A top-down view of the FDTD simulation region for an Au nanodisk. The gray rectangle represents the glass substrate, the white box represents the light source, the orange box represents the FDTD simulation region, the blue box represents the frequency domain power monitor, the yellow box represents the absorption monitors for the x and y axes, the red box represents the mesh, and the yellow circle represents the Au nanodisk. (b) a 3D view of the FDTD region..... 43

Figure 3-2. An illustration of the three main steps of NSL: monolayer formation of PS beads, metal deposition over the monolayer producing the FONs, and the Fisher pattern produced after the removal of the PS beads..... 45

Figure 3-3 UV-visible extinction spectra of Ag single layer periodic particle arrays of (a-c) nanodisks and (d-h) nanoprisms on mica substrates. From top to bottom, the parameters indicated on the right represent tnanosphere diameter used in the masks, thickness of deposited metal, shape of nanostructure, and LSPR peak position. The reported spectra are raw, unfiltered data. The oscillatory signal superimposed on the LSPR spectrum seen in the data is due to interference of the probe beam between the front and back faces of the mica. Reprinted (adapted) with permission from Haynes, C. L.; Van Duyne, R. P., J. Phys. Chem. B 2001, 105, 5599-5611. Copyright 2001 American Chemical Society. 46

Figure 3-4 Illustration of the stages of EBL process using a positive photoresist. The bare substrate, resist application, conductor application, beam exposure, development, metal deposition, and lift off represent the described steps 1 through 7, respectively. 49

Figure 3-5 SEM images of structures produced by EBL. (a) A three-branched generation four dendrimer; (b) a five-branched generation two dendrimer; (c) a four-branched crosshair structure; (d) an array of nanorods; (e) a right-handed spiral structure; (f) a left-handed spiral structure. 50

Figure 3-6 (a) An SiO_2@Si substrate after the CVD process with the regions of interest indicated by the red ovals. (b) An AFM image of a bilayer MoS_2 flake with an SEM image of a trilayer inset..... 51

Figure 3-7 Schematic of the microscope setup used for the vis-NIR absorbance measurements..... 53

Figure 3-8 Schematic of the SHG microscopy setup..... 55

Figure 3-9 Dendrimers fabricated by EBL. (a-b) Three-branched first and second generations, respectively; (c-d) four-branched first and second generations, respectively; (e-f) five-branched first and second generations, respectively. 56

Figure 3-10 Simulated (red) and experimental (blue) absorbance spectra for (a) a four-branched generation one dendrimer, (b) a four-branched generation two dendrimer, (c) a five-branched generation one dendrimer, and (d) a five-branched generation two dendrimer. 58

Figure 3-11 (a) an SEM image of a four-branched generation one dendrimer. The red arrows indicate the length varied and the blue lines represent the width varied. (b) an SEM image of an array of dendrimers, with an identifying number shown..... 59

Figure 3-12 Absorbance spectra showing the difference between generation one (Gen 1 - red) and two (Gen 2 - blue) dendrimers with (a) three branches, (b) four branches, and (c) five branches. The inset shows generation two of these dendrimers and the scale bar is 200 nm. 60

Figure 3-13 Absorbance spectra of (a) three-, (b) four-, and (c) five-branched generation two dendrimers of varying sizes (as indicated above each individual spectrum). The peak positions of interest are highlighted with asterisks in (b) and (c) as a guide to the eye. (d) Linear increase in the peak position with respect to the branch length, where the blue line and square markers correspond to the blue asterisks in (b) and the red line and square markers correspond to the red asterisks in (c). 61

Figure 3-14 Absorbance spectra of (a) three-, (b) four-, and (c) five-branched generation two dendrimers of varying widths as indicated above each individual spectrum. The peak position of interest is indicated by the dashed line as a guide to the eye. 62

Figure 4-1 SEM image of an array of structures with various geometries and sizes (a), and the corresponding SHG microscopy image for a vertical input polarization and where both orthogonal polarizations were detected and added (b). 69

Figure 4-2 SEM images of the dendrimers produced using the EBL method. Demonstrated are three-branched generation 4 (a), four-branched generation 2 (b), five-branched generation 2 (c), and a representative array of structures (d). 71

Figure 4-3 Absorption spectra for the three-branched generation four (bottom), four-branched generation 2 (middle), and five-branched generation 2 (top) dendrimers. Insets have the corresponding the dendrimer above the spectrum; the scale bar is 200 nm. The spectra are shifted for clarity..... 72

Figure 4-4 SHG images of three-branched generation 4 dendrimers with a branch length of 135 nm with a horizontal (a) and vertical (d) irradiation, FDTD simulations of the electromagnetic enhancement hotspots for the same dendrimer with a horizontal irradiation for at 400 nm (b) and 800 nm (c), as well as the vertical irradiation at 400 nm (e) and 800 nm (f). 73

Figure 4-5 SEM image of a four-branched generation 2 dendrimer with an individual branch circled in blue for clarity (a), SHG microscopy image of these structures (b), and the simulated nonlinear enhancement hotspots at 400 nm (c) and 800 nm. 75

Figure 4-6 SEM image of a five-branched generation 1 dendrimer (a), SHG microscopy was performed on the structures, as demonstrated in (b), simulated electromagnetic enhancement hotspots for the five-branched generation 1 at (c) 400 nm and (d) 800 nm. 76

Figure 4-7 SHG images of five-branched generation 2 dendrimers with a branch length of 135 nm with a horizontal (a) and vertical (d) irradiation, FDTD simulations of the electromagnetic enhancement hotspots for the same dendrimer with a horizontal irradiation for at 400 nm (b) and 800 nm (c), as well as the vertical irradiation at 400 nm (e) and 800 nm (f). 77

Figure 4-8 Power dependent peak intensity for a five-branched generation two dendrimer with the second order curve fit shown in blue. 78

Figure 5-1 Top view (top row) and side view (bottom row) of the 2H (left) and 1T (right) structures for the molybdenum disulfide (MoS_2) monolayer. The trigonal prism coordination for the Mo atom in 2H MoS_2 and the octahedral coordination for the Mo atom in 1T-MoS_2 are also shown. Mo, cyan; S, yellow. Copyright obtained from ACS (https://pubs.acs.org/doi/10.1021/acs.chemmater.5b00986), further permissions related to the material excerpted should be directed to the ACS. 82

Figure 5-2 A representative crystal lattice of the 2H MoS_2 where the yellow nodes are S atoms, and the blue nodes are Mo atoms. The long (x) axis intersects an Mo atom, and the input polarization angle is indicated by θ. 85

Figure 5-3 Polar plots showing $\sin(2\theta)^2$ (red) and $\cos(2\theta)^2$ (blue). 87

Figure 5-4 (a) An optical, (b) SEM, and (c) AFM image of a multilayered MoS_2 flake. (d) A cross-section along an MoS_2 bilayer, indicated by the blue line in c). (e) The chemical structure of R6G dye. 88

Figure 5-5 SHGM of an MoS_2 flake with a side length of 27 μm. 89

Figure 5-6 SHGM of a multilayer MoS_2 flake with a cross-section of the SHG intensity (shown by the dotted line) inset. 90

Figure 5-7 (a) Raman Spectra of the Si/SiO_2 substrate (black), bare MoS_2 flakes (red), and MoS_2 flakes after R6G functionalization (blue). The common modes at 520 cm^{-1} is the lattice mode of the Silicon substrate (b) Confocal Raman map of the peaks at 383 cm^{-1} and 402 cm^{-1} (highlighted in red in a) and (c) the peak at 1362 cm^{-1} (highlighted in blue in a). 91

Figure 5-8 SHG maps of an MoS_2 bilayer before (a,c) and after (b,d) functionalization with R6G dye. 92

Figure 5-9 (a) An SHGM image of a functionalized MoS_2 trilayer with SHGM intensity polar plots of the (b) substrate and an MoS_2 (c) monolayer, (d) bilayer, and (e) trilayer, as well as (f) a second MoS_2 bilayer. The red data points in (b-f) represent the experimental values, while the blue lines in (c-f) represent the $Sin^2(2\theta)$ fit and were added as a guide to the eye. 93

Figure 6-1 Scheme of the functionalization of a generic gold nanomaterial under plasmon excitation with light. 100

Figure 6-2 (a) A high contrast SEM image of the polyaryl thin film formation on glass substrate after 2 minutes of irradiation. (b) Schematic illustration of the grating k-vector and the light k-vector. The grating is fully formed after 8 minutes of irradiation. 101

Figure 6-3 (a-c) SEM images of the gratings produced on glass with a polarization of 0°, 45°, and 90°, respectively. (d-f) Higher magnification images of (a-c), respectively. Patterns were obtained after an irradiance of 7.49×10^3 W/cm^2 for 8 minutes. 102

Figure 6-4 SEM image of the amorphous mass generated by the focused laser spot. 103

Figure 6-5 (a) AFM scan of the grating produced with a polarization of 0° (same structure as shown in Figure 6-2a. (b) Cross section of (a) as indicated in red. 104

Figure 6-6 SEM images of three different substrate thicknesses: 160 μm (a and d), 600 μm (b and e) and 1000 μm (c and f). 105

Figure 6-7 (a) Absorbance measurements of the NSL substrates with the 632.8 nm irradiation wavelength indicated by the black line. (b) An SEM image of the inset molecule grafted to the surface using a 632.8 nm laser after 3 minutes of irradiation with an irradiance of 7.49×10^3 W/cm^2. 106

Figure 6-8 SEM images of the grating produced on an NSL substrate for different irradiation times, as indicated in the top right of each panel. The scale bar is 2 μm. 107

Figure 6-9 SEM images and FDTD calculations for grafting on an NSL substrate for horizontal (a-c) and vertical (d-f) polarizations. 108

Figure 6-10 AFM scans of the grafting produced on the NSL substrates using (a) a horizontally polarized laser and (b) a vertically polarized laser, as well as (c) the bare NSL substrate. (d) The cross sections for (a), (b), and (c) are shown in red, blue, and black, respectively. The cross sections have been shifted in the y-axis for clarity..... 110

Figure 7-1 Distribution of the near-field at 530 nm (a), 630 nm (b) and 800 nm (c) for a horizontal polarization. The corresponding isowavelength map is shown in (d) and represent the spatial distribution of the field for wavelengths varying from 500 nm to 800 nm with a crosshair structure outlined in black. 117

Figure 7-2 (a) Depiction of a grafting experiment. (b) SEM image of an individual structure..... 118

Figure 7-3 (a) Representative SEM image of an array of dendrimers used for grafting with a single structure shown in the inset. (b) FDTD far-field scattering for ideal (defect-free) and real structures (as shown in Figure 7-1b) and experimental absorption measurements for a linearly polarized light oriented horizontally or vertically with respect to the structure axes. 119

Figure 7-4 SEM images of the dendrimers after irradiation under an 800 nm fs-pulsed laser, for both (a) horizontally and (b) vertically polarized light. (c) FDTD modelling of the near-field distribution upon irradiation at 800 nm for the real structure with a horizontal polarization. 120

Figure 7-5 A representative array of five structures, each individually irradiated under an 800 nm fs-pulsed laser with a horizontal polarization in the presence of the diazonium-containing solution. In this experiment, the 800 nm laser beam is focused to 1 micron and the sample is scanned using a piezo electric stage. Each structure is irradiated for 60s with the beam centered over the structure. The inset (blue box) shows a structure immersed in the same diazonium-containing solution but without any exposure to laser irradiation. 122

Figure 7-6 SEM images of the structures after irradiation under a 632.8 nm continuous-wave laser, for both (a) horizontally and (b) vertically polarized light. (c,d) represents the same images but colorized in red to highlight the areas on which grafting mainly occurred. (e) FDTD modelling of the near-field distribution upon irradiation at 630 nm for the real structure with a horizontal polarization. 123

Figure 7-7 (a) an SEM image of an array of crosshairs irradiates at 632.8 nm in the presence of diazonium salts. The blue box is near the center of the beam and the red box is near the edge. The difference in grafting is shown in more detail in (b) and (c). 124

Figure 7-8 SEM images of the crosshairs after irradiation under a 532 nm laser both (a) horizontally and (b) vertically polarized. (c) and (d) are the colorized images of (a) and (b), respectively, with the outline of the cross in black as a guide for the eye. (e) FDTD modelling of the near-field distribution upon irradiation at 530 nm for the real structure with a horizontal polarization. Reference background image used to generate (c) and (d) is provided shown in the inset of Figure 7-5..... 126

Figure 7-9 SEM images of the 532 nm irradiated crosshairs with a (a) vertical and (b) horizontal polarization with increasing laser intensity from left to right. The first structure on the left of (a,b) has not been irradiated as a reference. 127

Figure 8-1 (a) A scanning electron micrograph of an array of truncated spiral structures and with an individual structure (highlighted in blue) shown in (b). (c) and (d) shows the simulated (red) and experimental (blue) ΔAbs spectra for a truncated spiral structure with a diameter of 2.5 and 4 μm, respectively (Manuscript accepted in the Journal of Israel

Chemistry: Therien, D. A. B.; Read, S. T.; Rosendahl, S. M.; Lagugné-Labarthet, F., Isr. J. Chem. 2022. https://doi.org/10.1002/ijch.202200007) © 2022 WILEY-VCH Verlag GmbH & Co. KGaA, Weinheim. 134

List of Abbreviations, Symbols, and Nomenclature

©	Copyright
2ω	Second-harmonic frequency
A	Area of the beam
AFM	Atomic force microscopy
c	Speed of light
C-C	Carbon-carbon
CVD	Chemical vapour deposition
CW	Continuous wave
e	Elementary charge of the material
$\hat{e}$	Polarization vector
$\mathbf{E}(\omega)$	Input photons
EBL	Electron-beam lithography
EE	Electromagnetic enhancement
EM	Electromagnetic
FDTD	Finite-difference time-domain
FON	Film over nanospheres
HZSMA	Hybrid ZnO silver mushroom array
$\mathbf{I}(\omega)$	Intensity of the fundamental frequency

k	Light wavevector
L	Fresnel factor
LCP	Left-circularly polarized
LIPSS	Laser-induced periodic surface structures
LSPRs	Localized surface plasmon resonances
m_e	Effective mass of an electron
N.A.	Numerical aperture
n_{avg}	Average refractive index
n_e	Electron density
NLO	Nonlinear optics
NSL	Nanosphere lithography
P(ω)	Polarizability of a material
PD-SHG	Polarization-dependent second-harmonic generation
PML	Perfectly matched layer
PMMA	Poly(methyl methacrylate)
PS	Polystyrene
QDs	Quantum dots
R6G	Rhodamine 6G
RCP	Right-circularly polarized

S(2ω)	Theoretical intensity for the SHG signal
SCS	Scattering cross-section
SEF	Surface-enhanced fluorescence
SEIRA	Surface-enhanced infrared absorption
SEM	Scanning electron microscopy
SERS	Surface-enhanced Raman Spectroscopy
SFG	Sum-frequency generation
SH	Second-harmonic
SHG	Second-harmonic generation
SHGM	Second-harmonic generation microscopy
SMA	Silver mushroom array
SPRs	Surface plasmon resonances
T	Pulse width of the laser at the fundamental frequency
TCANE	Two-colour anisotropic nanoemitters
TEM	Transmission electron microscopy
TERS	Tip-enhanced Raman spectroscopy
TMDs	Transition metal dichalcogenides
TPPL	Two-photon photoluminescence
UC	Upconversion

UV	Ultraviolet
vis-NIR	Visible-near-infrared
β	Exit angle of the SHG signal relative to the direction of the fundamental laser
β_{ijk}	Hyperpolarizability
ΔAbs	Differential absorbance: circular dichroism (LCP-RCP)
ε_0	Vacuum permittivity constant
ε_m	Metal dielectric constant
λ	Wavelength
Λ	Grating periodicity
$\chi^{(2)}$	Second-order nonlinear susceptibility
ω	Frequency of the impinging electromagnetic field
ω_ρ	Frequency of the surface electron oscillations from a bulk material or plasmon frequency

List of Appendices

Appendix A: Copyrights and permissions granted from their respective holders. 137

Chapter 1

1 General Introduction

Since the first journal publication in 1959 by Horie,[1] the interest in plasmonics has grown rapidly with over 6000 manuscripts in the field every year (Figure 1-1). The discovery of plasmons set in motion the development of a plethora of new fields, including plasmon-enhanced biosensing,[2-5] plasmon-enhanced Raman spectroscopies,[6-8] optical sensing,[9-12] and photocatalysis.[13-15] The field of optics was revolutionized by the discovery of plasmonics, nonlinear optics in particular has benefitted from enhancement techniques involving plasmonic materials.[13, 15-17]

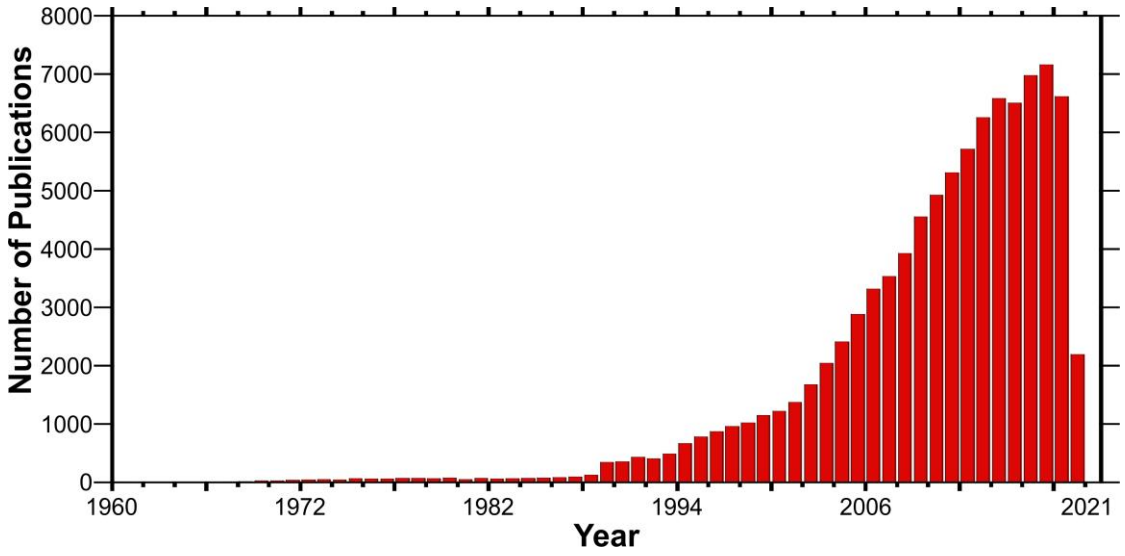

Figure 1-1 The number of publications with "plasmon" as a keyword from 1960 to 2021. Data was acquired from webofknowledge.com using the keyword “plasmon”.

1.1 Applications of Plasmons

Plasmonic materials have proven to be highly effective materials for confining, guiding, and enhancing optical fields thus opening many applications. The range of these applications is broad and encompasses biology, chemistry, and physics. Research in plasmonic materials in particular has led to the development of a variety of enhanced sensing techniques, most noticeably surface-enhanced Raman spectroscopy (SERS).[6]

Other applications of these materials include nanocatalysis,[18] investigating biomolecular interactions,[19] and many more.[17, 20-22]

1.1.1 Plasmon-Enhanced Nonlinear Optics

Plasmon-enhanced nonlinear optics in particular has gained interest due to high enhancement factors provided by a strongly confined optical field in the vicinity of a metallic nanostructure.[23, 24] In the field of biology, second-harmonic generation (SHG) has already proven to be an effective tool for *in vivo* imaging,[25] and has even been applied to study the growth of tumors and the effectiveness of chemotherapy.[26] When coupled with plasmonic nanomaterials, SHG can also be used in the enhanced imaging of live cells thus providing better optical contrast and/or shorter acquisition times.[27]

SHG active nanomaterials can be produced through a variety of methods, including lithography,[28, 29] chemical vapour deposition (CVD),[16] and electrochemical deposition.[30] Second-harmonic generation microscopy (SHGM) is well suited to characterize nanomaterials with nonlinear optical activity and other materials or devices that incorporate SHG materials, such as waveguides,[31] defect detection in crystal lattices,[32] and single molecule detection.[33, 34]

A study done by Shen *et al.* demonstrates the effects of a hybrid material on the plasmonic resonances, and subsequently the SHG response (Figure 1-2a).[35] In this work, the authors present Ag nanomushrooms grown on an Au thin film with a varying C-dopant concentration. The C-dopant acts as a bridge between the spectra features of the Au and the Ag. Furthermore, they introduce a ZnO film into the cavities between the Au/Ag/C nanomushrooms. The thickness of the film enhances the plasmonic coupling between the localized and propagating surface plasmons. As shown in figure 1-2a, the signal of the hybrid material (labelled HZSMA [black]) dwarfs its individual components (labelled ZnO@Au [red] and SMA [blue]).

Additionally, work done by Hsu *et al.* on transition metal dichalcogenides (TMDs) introduces the effects of artificially stacking monolayer flakes (Figure 1-2b,c).[36] TMDs are known to produce a second-harmonic response based on their crystal phase.[36, 37] This

stacking permits the visualization of both constructive and destructive interference in the SHG response (Figure 1-2c) due to the orientation of the crystal lattices stacked on top of one another.

Less conventional SHG active nanomaterials have also been developed by Cheng *et al.* in the form of mesoscale flower-like Ag particles grown by time-dependent electrochemical deposition (Figure 1-2d,e).[30] When the particle growth time increases, the particles develop a shape more closely resembling a flower, reaching a critical point after 180 seconds. After this critical time point, a thin film of Ag starts to develop. The SHG signal, stemming from the amorphous nature of the nanoparticles and the surface roughness, from these Ag flowers increases up to the critical time point, after which is begins to decrease as the discrete surface plasmons become lost to the thin film surface.

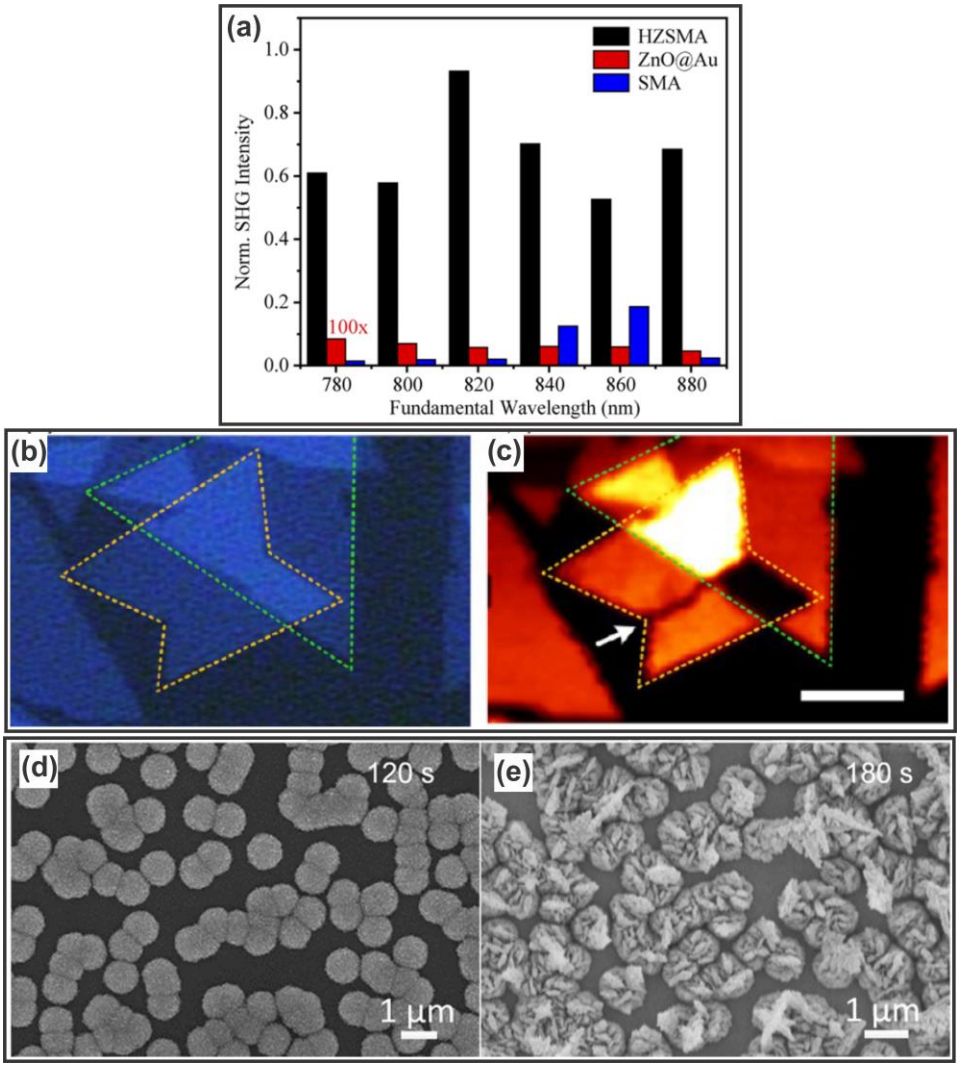

Figure 1-2 (a) The SHG intensity for the hybrid ZnO silver mushroom array (HZSMA), the ZnO particles on Au, and the silver mushroom array (SMA) for different fundamental wavelengths. The values were normalized to the most intense SHG signal, and the red values were multiplied by a factor of 100 for visibility, reprinted from Shen, S.; Yang, W.; Shan, J.; Sun, G.; Shih, T.-M.; Zhou, Y.; Yang, Z., J. Chem. Phys. 2020, 153, 151102., with the permission from AIP Publishing; (b) an optical image of artificially stacked MoS_2 flakes with (c) the corresponding SHGM image, reprinted (adapted) with permission from Hsu, W.-T.; Zhao, Z.-A.; Li, L.-J.; Chen, C.-H.; Chiu, M.-H.; Chang, P.-S.; Chou, Y.-C.; Chang, W.-H., ACS Nano 2014, 8, 2951-2958. Copyright 2014 American Chemical Society; SEM images of mesoscale flower-like Ag particles after (d) a 120 s synthesis and (e) a 180 s

synthesis, reprinted from Cheng, Z.-Q.; Li, Z.-L.; Luo, X.; Shi, H.-Q.; Luo, C.-L.; Liu, Z.-M.; Nan, F., Appl. Phys. Lett. 2019, 114, 011901.], with the permission from AIP Publishing.

1.1.2 Plasmon-Mediated Chemistry at the Nanoscale

Upon excitation, the localized surface plasmon resonances (LSPRs) of a nanomaterial will generate hot electrons in their vicinity. As a result, these materials have shown the potential to mediate chemical reactions.[14] The hot electrons generated are readily available to catalyze reactions and promote reactions at the surface. In fact, plasmonic materials have demonstrated the ability to facilitate a variety of reactions, including dimerization,[38] water splitting,[39] and surface functionalization.[40, 41] Furthermore, by incorporating plasmonic nanomaterials into optoelectronic devices, their functionality can be improved. [42-44] For example, the work done by Tooghi *et al.* demonstrates a highly efficient perovskite solar cell using a photonic-plasmonic nanostructure.[42] In this study, the authors incorporated plasmonic nanomaterials into the perovskite layer to trap light inside the solar cell leading to a 33% increase in the power conversion efficiency in their cells without an increase in the thickness of the absorbing layer.

Another interesting application of hot electrons is surface polymerization and lithography. A recent study by Kameche et al. demonstrates the near-field polymerization reaction utilizing Au nanoparticles.[14] In this study, the polymerization mechanism is explored using circular polarized light to induce the polymerization of a free-radical acrylate monomer (Figure 1-3). Here, they propose a mechanism for the physicochemical reaction occurring at the material surface. This study suggests that the hot electrons generated by the decay of the plasmon are responsible for the functionalization at the surface of the particles. Consequently, this study allows a better understanding of plasmon-mediated chemical reactions.

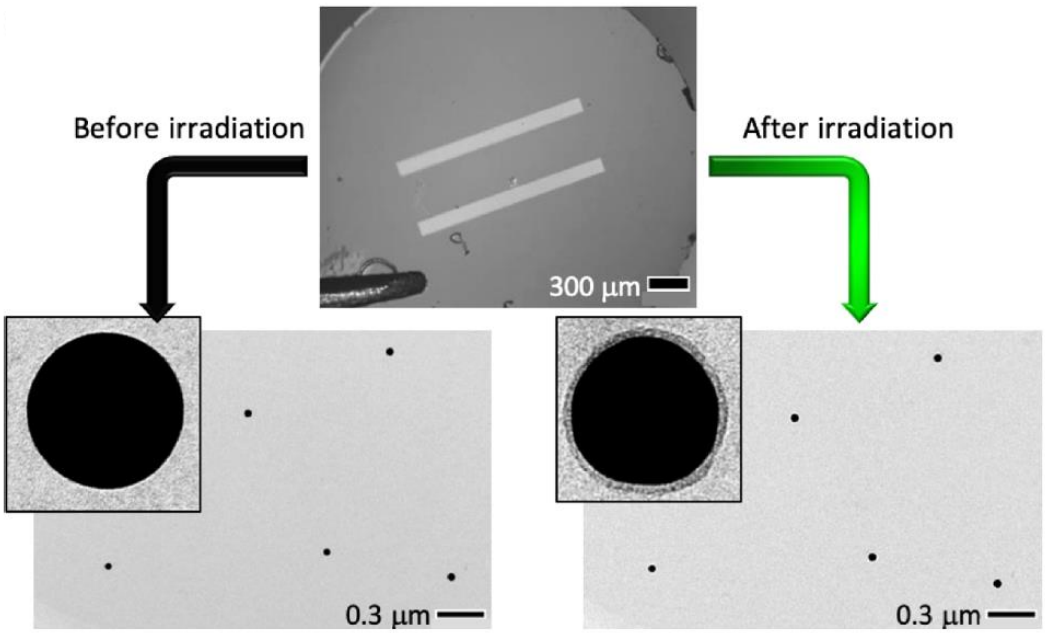

Figure 1-3 Transmission electron microscopy (TEM) images of a TEM grid (top), and Au nanoparticles before and after irradiation in the presence of the acrylate monomer, reprinted (adapted) with permission from Kameche, F.; Heni, W.; Telitel, S.; Vidal, L.; Marguet, S.; Douillard, L.; Fiorini-Debuisschert, C.; Bachelot, R.; Soppera, O., J. Phys. Chem. C 2021, 125, 8719-8731. Copyright 2021 American Chemical Society.

1.2 Scope of Thesis

The main goals of this thesis are to (1) evaluate the nonlinear optical properties of plasmonic materials as well as materials with intrinsic SHG properties using second-harmonic generation microscopy and (2) to apply plasmonic nanomaterials for wavelength- and polarization-dependent surface specific chemistry at a nanoscale level.

In Chapter 2, a brief review on the underlying theory about the properties of plasmonic materials, finite-difference time-domain modelling, and nonlinear optical microscopy re provided. We show in particular how the properties of these metamaterials are modelled to better understand how the fields are confined and the materials response. The home-made SHG optical microscope and optical microscope are thoroughly described. Finally, the principles of plasmon decay and plasmon-mediated surface chemistry is explained.

In Chapter 3, the fabrication and characterization methods used to obtain the results in Chapters 4-7 are presented. These methodologies include details on the components for the modelling approaches, the deposition method for the 2-D materials presented in Chapter 5, and the lithographic techniques to produce metamaterial. Next, the tuning methods for the metamaterials, finishing with the techniques used for surface functionalization.

In Chapter 4, plasmon-enhanced SHGM of fractal metamaterials is reported an analyzed. In particular, the polarization-dependent SHG response of these materials was compared for structures with C_3, C_4, and C_5-symmetry. Interestingly, the effect of plasmonic enhancement on SHG was observed in structures both with and without a center of inversion.

In Chapter 5, SHGM of transition metal dichalcogenides (TMDs) 2D flakes is explored. The SHG response of the TMDs was further enhanced when functionalized with an organic dye at its surface. Polarization-dependent SHGM analysis was completed and compared to the theoretical response of the bare 2D flakes highlighting a small enhancement upon functionalization.

In Chapter 6, the functionalization of both a bare glass coverslip, and a glass substrate with large surface areas of Au nanoprisms is studied using single-beam inscription. The theory behind the bare glass and Au nanoprisms functionalization is explained. The effect of light polarization on the grafting pattern on the Au nanoprism substrate is to the modelled response.

In Chapter 7, a metamaterial designed to exhibit three exploitable plasmonic resonances in the visible spectral range was developed. This metamaterial was simulated, fabricated, and employed in plasmon-mediated functionalization showing its responsiveness at 532 nm, 632 nm, and 800 nm. The effects of irradiation wavelength and laser polarization on the grafting pattern observed is discussed and compared to the modelled resonance positions.

Finally, we conclude in Chapter 8, highlighting the impact of the work presented in Chapters 4 through 7 and providing possible future directions and potential applications of our investigations, including applications of these materials in the visible to the mid-infrared spectral range.

1.3 References

1. Horie, C., *Prog. Theor. Phys.* **1959,** *21*, 113-134.

2. Kim, Y.; Gonzales, J.; Zheng, Y., *Small* **2021,** *17*, 2004988.

3. Mishra, A.; Ferhan, A. R.; Ho, C. M. B.; Lee, J.; Kim, D.-H.; Kim, Y.-J.; Yoon, Y.-J., *Int. J. Precis. Eng. Manuf.* **2021,** *8*, 945-954.

4. Camarca, A.; Varriale, A.; Capo, A.; Pennacchio, A.; Calabrese, A.; Giannattasio, C.; Murillo Almuzara, C.; D'Auria, S.; Staiano, M., *Sensors* **2021,** *21*, 906.

5. Li, C.; Jin, Y., *Adv. Funct. Mater.* **2021,** *31*, 2008031.

6. Zhang, J.; Kolhatkar, G.; Ruediger, A., *J. Mater. Chem. C* **2021,** *9*, 6960-6969.

7. Zhang, D.; Zhang, X.; Ma, R.; Deng, S.; Wang, X.; Wang, X.; Zhang, X.; Huang, X.; Liu, Y.; Li, G.; Qu, J.; Zhu, Y.; Li, J., *Water Res.* **2021,** *200*, 117243.

8. Jiang, L.; Hassan, M. M.; Ali, S.; Li, H.; Sheng, R.; Chen, Q., *Trends Food Sci. Technol.* **2021,** *112*, 225-240.

9. Xavier, J.; Yu, D.; Jones, C.; Zossimova, E.; Vollmer, F., *Nanophotonics* **2021,** *10*, 1387-1435.

10. Butt, M. A.; Khonina, S. N.; Kazanskiy, N. L., *Fiber Integr. Opt.* **2021,** *40*, 14-47.

11. Knoll, W.; Liu, J.; Yu, F.; Niu, L.; Reiner-Rozman, C.; Köper, I., *Chemosensors* **2021,** *9*, 11.

12. Daniyal, W. M. E. M. M.; Fen, Y. W.; Saleviter, S.; Chanlek, N.; Nakajima, H.; Abdullah, J.; Yusof, N. A., *Polymers* **2021,** *13*, 478.

13. Becerra, J.; Gopalakrishnan, V. N.; Quach, T.-A.; Do, T.-O., *Chem. Cat. Chem.* **2021,** *13*, 1059-1073.

14. Kameche, F.; Heni, W.; Telitel, S.; Vidal, L.; Marguet, S.; Douillard, L.; Fiorini-Debuisschert, C.; Bachelot, R.; Soppera, O., *J. Phys. Chem. C* **2021,** *125*, 8719-8731.

15. Kumar, A.; Choudhary, P.; Kumar, K.; Kumar, A.; Krishnan, V., *Mater. Chem. Front.* **2021,** *5*, 1448-1467.

16. Ma, J.; Sun, M., *Nanophotonics* **2020,** *9*, 1341-1358.

17. Butet, J.; Brevet, P.-F.; Martin, O. J. F., *ACS Nano* **2015,** *9*, 10545-10562.

18. Gellé, A.; Jin, T.; de la Garza, L.; Price, G. D.; Besteiro, L. V.; Moores, A., *Chem. Rev.* **2020,** *120*, 986-1041.

19. Bocková, M.; Slabý, J.; Špringer, T.; Homola, J., *Annu. Rev. Anal. Chem.* **2019,** *12*, 151-176.

20. Wallace, G. Q.; Lagugné-Labarthet, F., *Analyst* **2019,** *144*, 13-30.

21. Tuniz, A., *Riv. del Nuovo Cim.* **2021,** *44*, 193-249.

22. McRae, D. M.; Lagugné-Labarthet, F., *Nat. Nanotechnol.* **2019,** *14*, 922-923.

23. Collins, J. T.; Kuppe, C.; Hooper, D. C.; Sibilia, C.; Centini, M.; Valev, V. K., *Adv. Opt. Mater.* **2017,** *5*, 1700182.

24. Sain, B.; Meier, C.; Zentgraf, T., *Adv. Photonics* **2019,** *1*, 024002.

25. Malkinson, G.; Mahou, P.; Chaudan, É.; Gacoin, T.; Sonay, A. Y.; Pantazis, P.; Beaurepaire, E.; Supatto, W., *ACS Photonics* **2020,** *7*, 1036-1049.

26. Lukina, M. M.; Dudenkova, V. V.; Shimolina, L. E.; Snopova, L. B.; Zagaynova, E. V.; Shirmanova, M. V., *Cytometry A* **2019,** *95*, 47-55.

27. Sinha, S. S.; Jones, S.; Demeritte, T.; Chavva, S. R.; Shi, Y.; Burrell, J.; Pramanik, A.; Ray, P. C., *J. Phys. Chem. C* **2016,** *120*, 4546-4555.

28. Cesca, T.; Michieli, N.; Kalinic, B.; Balasa, I. G.; Rangel-Rojo, R.; Reyes-Esqueda, J. A.; Mattei, G., *Mater. Sci. Semicond. Process.* **2019,** *92*, 2-9.

29. Valev, V. K., *Langmuir* **2012,** *28*, 15454-15471.

30. Cheng, Z.-Q.; Li, Z.-L.; Luo, X.; Shi, H.-Q.; Luo, C.-L.; Liu, Z.-M.; Nan, F., *Appl. Phys. Lett.* **2019,** *114*, 011901.

31. Luo, R.; He, Y.; Liang, H.; Li, M.; Lin, Q., *Optica* **2018,** *5*, 1006-1011.

32. Li, Z.; Zhang, S.; Huang, Z.; Zhao, L.-D.; Uykur, E.; Xing, W.; Lin, Z.; Yao, J.; Wu, Y., *Chem. Mater.* **2020,** *32*, 3288-3296.

33. Salafsky, J. S., *Chem. Phys. Lett.* **2001,** *342*, 485-491.

34. Clevers, S.; Rougeot, C.; Simon, F.; Sanselme, M.; Dupray, V.; Coquerel, G., *J. Mol. Struct.* **2014,** *1078*, 61-67.

35. Shen, S.; Yang, W.; Shan, J.; Sun, G.; Shih, T.-M.; Zhou, Y.; Yang, Z., *J. Chem. Phys.* **2020,** *153*, 151102.

36. Hsu, W.-T.; Zhao, Z.-A.; Li, L.-J.; Chen, C.-H.; Chiu, M.-H.; Chang, P.-S.; Chou, Y.-C.; Chang, W.-H., *ACS Nano* **2014,** *8*, 2951-2958.

37. Lucking, M. C.; Beach, K.; Terrones, H., *Sci. Rep.* **2018,** *8*, 10118.

38. Zhang, Z.; Merk, V.; Hermanns, A.; Unger, W. E. S.; Kneipp, J., *ACS Catal.* **2017,** *7*, 7803-7809.

39. Yan, L.; Xu, J.; Wang, F.; Meng, S., *J. Phys. Chem. Lett.* **2018,** *9*, 63-69.

40. Therien, D. A. B.; McRae, D. M.; Mangeney, C.; Félidj, N.; Lagugné-Labarthet, F., *Nanoscale Adv.* **2021,** *3*, 2501-2507.

41. Tijunelyte, I.; Kherbouche, I.; Gam-Derouich, S.; Nguyen, M.; Lidgi-Guigui, N.; de la Chapelle, M. L.; Lamouri, A.; Lévi, G.; Aubard, J.; Chevillot-Biraud, A.; Mangeney, C.; Felidj, N., *Nanoscale Horiz.* **2018,** *3*, 53-57.

42. Tooghi, A.; Fathi, D.; Eskandari, M., *Sci. Rep.* **2020,** *10*, 11248.

43. Gaggiotti, S.; Hurot, C.; Weerakkody, J. S.; Mathey, R.; Buhot, A.; Mascini, M.; Hou, Y.; Compagnone, D., *Sens. Actuators B Chem.* **2020,** *303*, 127188.

44. Wang, H.; Li, S.; Ai, R.; Huang, H.; Shao, L.; Wang, J., *Nanoscale* **2020,** *12*, 8095-8108.

Chapter 2

2 Linear and Nonlinear Optical Properties of Plasmonic Nanomaterials

This chapter focuses on the materials and characterization techniques used in this thesis. Details on plasmonic materials, including simulations, characterization, and applications are presented. Some elements of theory regarding second-harmonic generation activity in nanomaterials are provided. Finally, the key factors that are involved in plasmon-mediated grafting are described.

2.1 Plasmonically Active Materials

Since their proposed existence in 1952 by Pines and Bohm, surface plasmons have become pivotal in their usage for enhanced spectroscopies.[1] The field of plasmonics utilizes the combination of light and conductive materials to produce areas of electromagnetic enhancement (EE) at desired frequencies. The conductive material used is typically a coinage metal, which are copper (Cu), gold (Au), and silver (Ag).[2, 3] Other metals have been used in plasmonic applications, including aluminum (Al) and platinum (Pt).[4, 5] The EE produced by these materials is due to the strong interactions between the incident light and the conduction electrons at the metals surface. Another, non-metal, material that has shown surface enhancement is graphene which has been proposed as an alternative substrate in graphene-enhanced Raman scattering.[6-8] These materials display local field enhancement confined to very small volumes (< nm^3) located at the interface between the nanostructure and a dielectric.

Such localized enhancement in the vicinity of the plasmonic materials can be exploited for plasmon-mediated processes where the electrons of the metallic nanostructure are used to trigger surface-induced functionalizations and reactions.[9-11] Additionally, plasmonic materials can be used to perform enhanced highly sensitive spectroscopy measurements through an electromagnetic surface enhancement. These spectroscopies have elicited a broad interest in analytical and bioanalytical chemistry with surface-enhanced Raman spectroscopy (SERS),[12-15] surface-enhanced infrared reflection-absorption spectroscopy,[16-18] tip-enhanced Raman spectroscopy (TERS),[19-22] surface-

enhanced fluorescence (SEF),[23-25] and plasmon-enhanced second-harmonic generation.[26-30]

2.1.1 Surface Plasmon Resonances (SPRs)

Upon irradiation with a light at a resonant wavelength, the oscillation between a metal and a dielectric is known as a surface plasmon resonance (SPR) and will displace the electrons out of phase relative to the input energy across the surface of the metal. The oscillations occur under the area irradiated and the resulting electric field intensity will decay exponentially away from the metal surface. The frequency of the surface electron oscillations from a bulk material (ω_p) in vacuum can be described as:[31]

$$\omega_p = \frac{1}{2\pi}\sqrt{\frac{n_e e^2}{m_e \varepsilon_0}} \qquad [2\text{-}1]$$

where n_e is the average electron density of the bulk conductive material at the surface, e is the electron charge, m_e represents the effective mass of an electron, and ε_0 represents the vacuum permittivity constant.

These SPRs occur at specific frequencies based on a variety of factors, such as the thickness of the metallic layer, the material, and the chemical nature of the medium.[32] These SPRs will generate areas of higher or lower electron density at the intersection between the metal and the dielectric, based on the input wavelengths frequency and polarization (Figure 2-1).

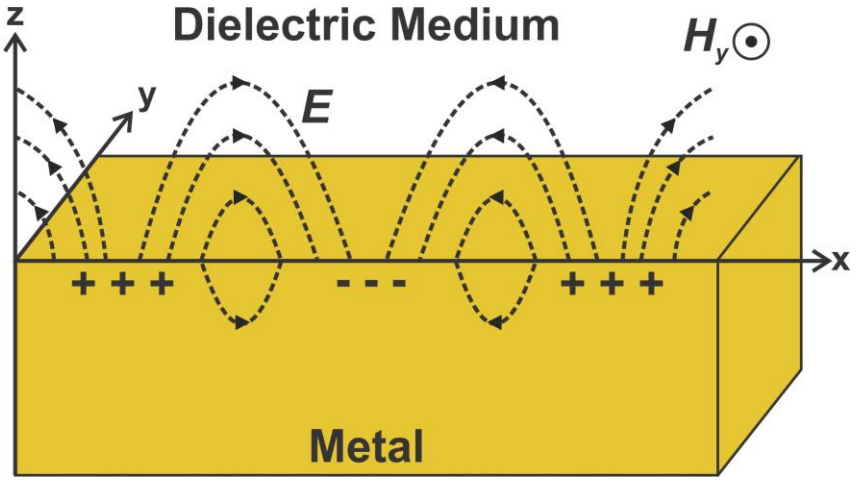

Figure 2-1 A schematic of the electric field generated by the SPR.

In general, SPR excitation requires that the dielectric function of the illuminated material has a negative real component and a positive imaginary component. The dielectric constant of a metal can be defined as the ratio between the permittivity of an electron influx and the vacuum permittivity. The relationship of the metal's dielectric constant (ε_m) and the plasmon frequency (ω_p) is given by:[31]

$$\varepsilon_m = 1 - \frac{\omega_p^2}{\omega^2} \qquad [2\text{-}2]$$

where, ω is the frequency of the impinging electromagnetic field. To satisfy the requirements to produce the SPRs, $|\omega|$ must be smaller in value than $|\omega_p|$, which is usually achieved using coinage metals (e.g.: Au, Al, Cu, Ag). The relationship between the oscillations of the conduction electrons of a metal and the index of refraction of a dielectric can be calculated using the Drude-Lorentz dispersion model. Simply put, this model considers the conduction electrons to be a harmonic oscillator that will respond to the input electromagnetic field. Treating the electrons as such allows the real and imaginary dielectric constants of metals to be calculated based on the impinging light. Using this Drude-Lorentz model, the real and imaginary dielectric constants Au, Ag, Cu, and Al can be calculated for various wavelengths (Figure 2-2).[2]

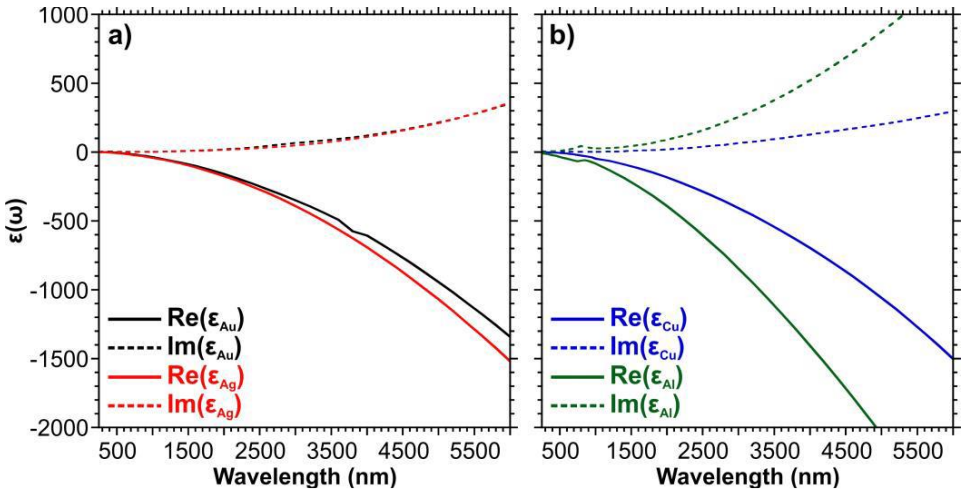

Figure 2-2 Complex dielectric constant for a) Au (black) and Ag (red) and b) Cu (blue) and Al (green), as calculated by the Drude-Lorentz model.[2]

2.1.2 Localized Surface Plasmon Resonances

SPRs can be further confined to the surface when the material is in a nanostructured form. When the nanomaterial is significantly smaller than the irradiation wavelength, the plasmonic resonance becomes confined, or localized, to the surface of the nanomaterial, otherwise known as a localized surface plasmon resonance (LSPR).[33] The confinement of the electric field to these nanomaterials will generate LSPR modes or "hot spots", an example of oscillation of the electric field around an Au nanosphere (Figure 2-3a).

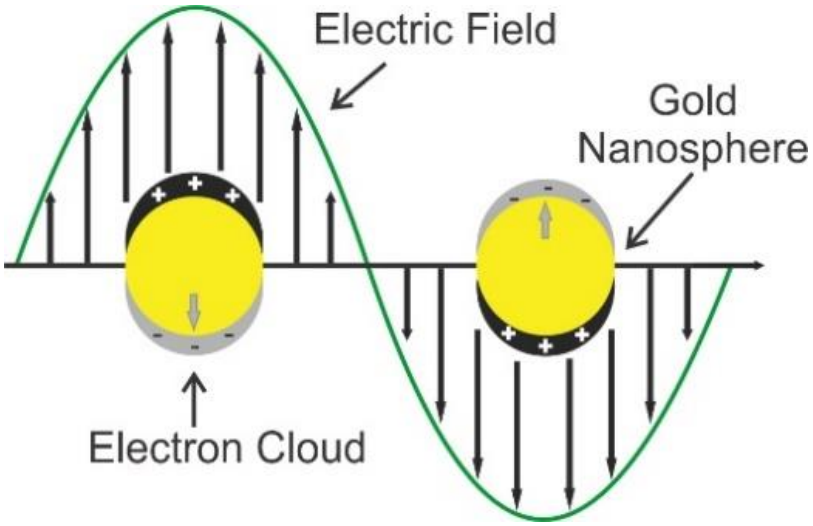

Figure 2-3 Schematic oscillation of the electric field around an Au nanosphere.

LSPRs will vary based on the size, shape, and arrangement of the nanomaterials and can be tailored to specific wavelengths using both lithographic,[34-36] and synthetic methods.[37-39] Their response to an impinging field will also depend on the input field properties including wavelength, pulse duration, and polarization. Since many of these materials and field parameters can be selected in different combinations, several modes with distinct energies, polarizations, and spatial localizations can thus be observed. For example, an Au nanodisk excited at 775 and 930 nm will excite the quadrupolar and dipolar modes, respectively (Figure 2-4).[40]

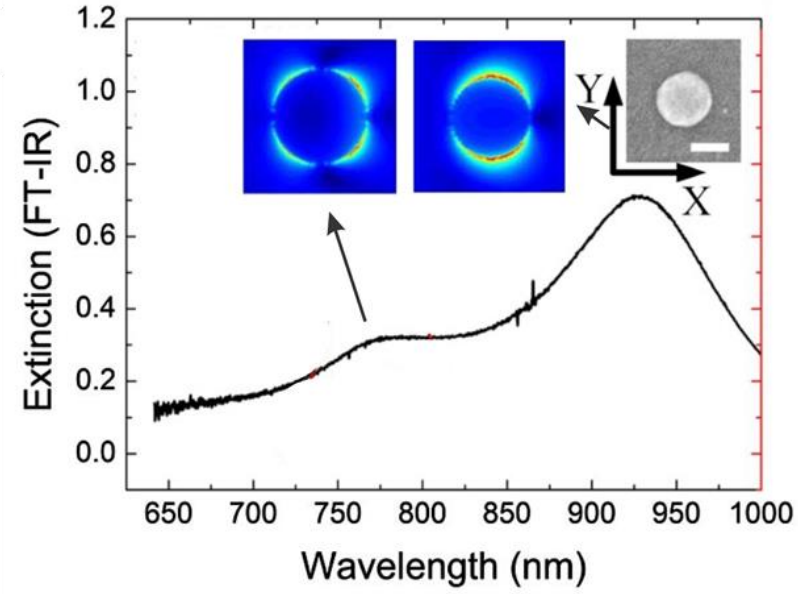

Figure 2-4 Far field extinction spectra for a gold nanodisk with a diameter of 280 nm with the near field enhancement maps inset showing the quadrupolar and dipolar LSPRs present at 775 and 930 nm, respectively. Reprinted (adapted) with permission from Butet, J.; Brevet, P.-F.; Martin, O. J. F., ACS Nano 2015, 9, 10545-10562. Copyright 2015 American Chemical Society.

Additionally, the energy of an impinging electromagnetic field can be confined to the surface by modifying the shape of the nanomaterial, producing different resonance modes that result in more intense, broader, hot spots.[15] Further surface modifications include producing nanomaterials in proximity of one another, forming dimers, trimers, or even chains of materials.[41] Such surface modifications will produce more intense hot spots

near the junctions of the nanomaterials due to a coupling of the LSPRs.[42] These nanomaterials can also be placed onto a substrate, allowing for polarization-controlled excitation of individual LSPRs that is not possible in a colloidal solution.[43]

Small alterations in these opto-geometric parameters will greatly affect the position of the resonances thus providing a high degree of tunability. For example, modifying the shape of an Au nanoparticle from a triangle to a decahedron or an icosahedron, while maintaining a consistent plasmon length, will demonstrate a spectral shift in the LSPR mode.[44] These materials have been proven effective in enhancing optical processes for a variety of applications. One of such applications is plasmon-enhanced second-harmonic generation microscopy,[45] which can be used for the characterization of the strain in two-dimensional materials,[46] SHG microscopy (SHGM) in microfluidic chips,[47] and as a pre-screening tool for surface-enhanced hyper Raman scattering platforms.[48]

2.1.3 Metamaterials

Metamaterials are artificial materials made by bottom-up or top-down approaches that consist of an assembly of nanoscale building blocks that are organized both two- or three-dimensional fashions with periodicities and dimensions close to that of the incident wavelength.[49, 50]

Like nanomaterials, metamaterials have dimensions on the same order of magnitude as the irradiation wavelength. However, they can interact more efficiently with impinging fields than nanomaterials and will generate more effective LSPR modes with larger surface areas than using simple structures. Due to their unique optical properties, metamaterials have shown potential in a variety of fields including chiral sensing,[51-53] negative refraction indices,[54] optical magnetism,[55] and invisibility cloaking.[56, 57]

Another example is enhanced second-harmonic generation microscopy from metamaterials, which is explained in greater detail in chapter 4 of this thesis.[30] Metamaterials are effective at enhancing the sensitivity and the acquisition speed of measurements. The design basis of these metamaterials come from a variety of sources,

including geometric shapes,[14, 15, 30] chain-links,[58] and even from biological tissues.[59] An example of a metamaterial is shown in Figure 2-5.[14, 15]

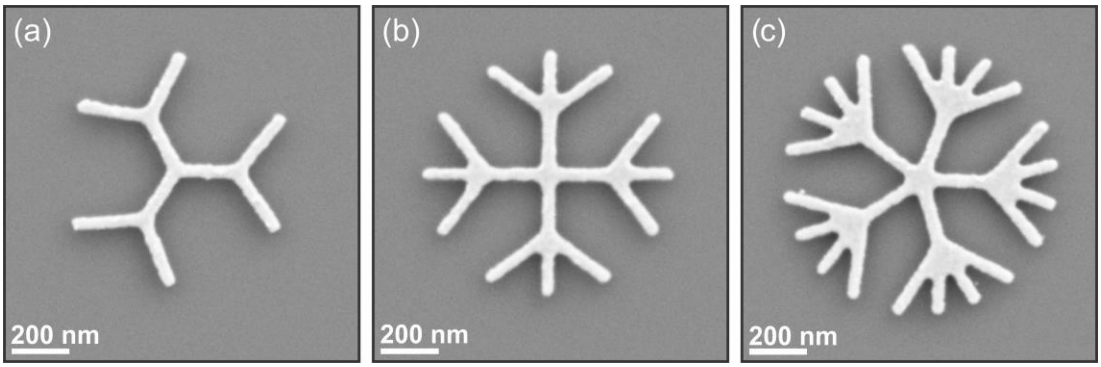

Figure 2-5 A series of SEM images of metamaterials known as dendritic fractals. (a) A three-branched generation 2 fractal, (b) a four-branched generation 2 fractal, and (c) a five-branched generation 2 fractal.

Metamaterials offer a higher sensitivity, faster response, and even an immunity to electromagnetic interference. Furthermore, the confinement and enhancement of the field to subwavelength areas has allowed both single molecule detection and nanoscale spatial resolutions.[60-64] As well, a significant reduction in the laser power required for molecule detection stems from the significant enhancement of the electromagnetic field from the metamaterials, allowing for a less destructive method of detection.[62, 65] This is particularly important when working with sensitive materials, such as biological samples.[66, 67] Other applications of interest include the study of the hot-electron generation process, discussed later in this chapter.

2.2 FDTD Electromagnetic Modelling

To better understand how LSPRs work and to predict the optical responses of materials, calculations can be performed using Maxwell's equations. Such calculations are particularly useful for metamaterials that have more complex arrangements or shapes than a single sphere or triangle, as there are few suggested theories for more intricate nanomaterials. Modelling the optical properties of metamaterials can be done using a variety of electrodynamic calculations, including the discrete dipole approximation, the finite element method, and the finite-difference time-domain (FDTD) method. These

different methods can be used to calculate the response of metamaterials under an electromagnetic field and produce accurate absorption spectra and maps the areas of electromagnetic enhancement.

The FDTD method can solve Maxwell's equations while discretizing space and time using finite-difference algorithms. The spatial domain breaks the simulation area into a cartesian grid using Yee's algorithm, and the resulting cartesian grid is known as a Yee cell (Figure 2-6). Yee cells are comprised of two pointing vectors, electric and magnetic, that are shifted by a half-grid point relative to one another. The calculations use the difference between these two vectors before and after the short pulse of the impinging light. This is a repeating process that continues until the simulation reaches a steady-state solution, known as convergence. Then, the time-domain portion of the results can be transformed using Fourier transform into frequency domain (absorption and scattering cross-section) spectra. Extinction measurements, which is the combination of both the absorption and scattering cross-section, can be used to characterize the strength of the plasmonic field, absorption measurements can be used to identify the spectral position of the LSPR modes.[68] For this thesis, only the absorption spectra were calculated using this method, so that comparisons could be made between the theoretical and experimental data. The scattering cross-section was not measured because of the nature of the microscope used to measure the SHG response of the materials. In other words, because of the irradiation and SHG signal collection both being orthogonal to the surface, any of the scattered light was not collected.

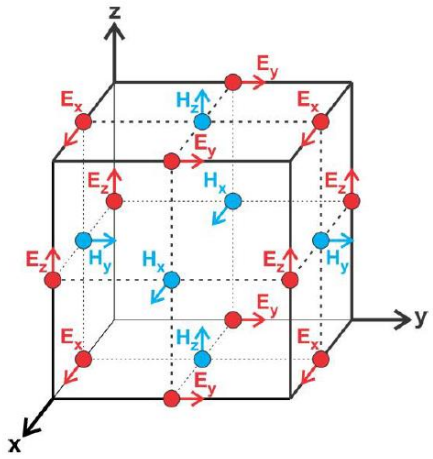

Figure 2-6 Illustration of a Yee cell, including the distribution of the magnetic (H) field (blue) and the electric (E) field (red) pointing vectors throughout the cell.

Although the use of Yee cells allows FDTD calculations to be performed on complex structures, it is worth noting that there can be cascading errors from the cartesian grid divide. These errors occur near the edges of the structures, where the Yee cells, with dimensions defined by the user (known as mesh size), are partially filled by the structure. The entirety of the cell then acts as the material of interest. This error can be mitigated by setting a smaller mesh size, but this comes at the cost of a significantly more computationally demanding simulation.

For the calculations presented in this thesis, a plane-wave source was used with an initial intensity of $E_0 = 1$, allowing the resulting electric field components (E_x, E_y, and E_z) to be normalized to the intensity of the light source. The normalized electric field ($|E_{x,y,x}/E_0|^2$) can be simply determined by squaring the obtained values for the individual E components, since $E_0 = 1$. This method was used to generate the polarized linear electromagnetic (EM) field maps throughout this thesis. Additionally, the nonlinear EM field maps can be calculated by incorporating the nonlinear susceptibility value of bulk Au ($\overleftrightarrow{\chi}^{(2)} = 3 \times 10^{-29} mV^{-1}$) into the simulations.[69-71] This nonlinear method can be used to calculate the SHG response of a metamaterial.[69]

2.3 Second-Harmonic Generation

Since its introduction in 1961 by *Franken et al.*, the field of SHGM has grown to be incorporated into our daily lives.[72] An example of a commonly used SHG active material is the potassium titanyl phosphate (KTP) crystal.[73, 74] The KTP crystal is birefringent, which means its crystal structure is asymmetric and will have different refractive indices based on the polarization, orientation, and frequency of the impinging field. For example, when light with a wavelength of 1064 nm is focussed in a KTP crystal, through phase matching process it generates photons at 532 nm (green).[75] This process is particularly efficient, allowing it to be used in green laser pointers.[75] In this work we have extensively used SHGM for the study of metamaterials that were designed to exhibit second-harmonic properties.

2.3.1 Principles of SHG

The electron cloud around a material can be manipulated by applying an electrical field. In other words, a materials' induced polarization is the response of a material upon irradiation with light. The degree to which the electrons of a material can be manipulated by light, whether it is a linear or nonlinear optical process, therefore falls under induced polarization.[76]

In nonlinear optics (NLO), the induced polarization of a material mainly depends on the nonlinear terms. The induced polarization of a material can be separated into multiple terms which depend on the number of input photons, and is given by:

$$\boldsymbol{P}(\omega) = \varepsilon_0 \overleftrightarrow{\chi}^{(1)} \boldsymbol{E}(\omega) + \varepsilon_0 \overleftrightarrow{\chi}^{(2)} \boldsymbol{E}(\omega)\boldsymbol{E}(\omega) + \cdots + \varepsilon_0 \overleftrightarrow{\chi}^{(i)} \boldsymbol{E}(\omega)^{(i)} \qquad [2\text{-}3]$$

Here, $\boldsymbol{P}(\omega)$ represents the induced polarization of the material, ε_0 represents the vacuum permittivity constant, $\boldsymbol{E}(\omega)$ represents the input photons, and $\overleftrightarrow{\chi}^{(n)}$ represents the polarization susceptibility and is a tensor for the physical properties of the material at the n^{th} order. $\overleftrightarrow{\chi}^{(n)}$ is a mathematical representation of the physical properties of the material based on the number of input photons. For example, a second-order optical process depends on the general $\overleftrightarrow{\chi}^{(2)}$ term, which is a 27-element tensor with a 3x3x3 (3-dimensional) distribution. There are multiple nonlinear optical processes that are

encompassed by the second induced polarization term, including sum-frequency generation (SFG), upconversion (UC), two-photon photoluminescence (TPPL), and second-harmonic generation (SHG). This thesis focuses on the SHG process. During the SHG process, a material absorbs two photons at a fundamental frequency, **E**(ω), and emits a single photon at double the frequency, **E**(2ω). This process, however, has a limiting selection rule: the material of interest must be non-centrosymmetric (*i.e.* cannot contain a centre of inversion). If a material does contain a center of inversion, the $\overleftrightarrow{\chi}^{(2)}$ term will either be identical upon an inversion operation, or all 27 elements will be equal to 0, resulting in no signal.

When dealing with nonlinear processes (*e.g.* SHG) the second-order susceptibility term can be isolated from the overall induced polarization. The second-harmonic signal resulting from the SHG process can be isolated and simplified to the following equation:

$$\boldsymbol{E}(2\omega) \propto \boldsymbol{P}(2\omega) = \overleftrightarrow{\chi}^{(2)}\boldsymbol{E}(\omega)^{\mathbf{2}} \qquad [2\text{-}4]$$

Where the SHG signal or polarization is proportional to the two variables: the nonlinear susceptibility and the input wavelength. Since the field vector oscillates positively and negatively with time, for negative values of the oscillation, [2-4] can be written:

$$-\boldsymbol{E}(2\omega) \propto -\boldsymbol{P}(2\omega) = \overleftrightarrow{\chi}^{(2)}\big(-\boldsymbol{E}(\omega)\big)\big(-\boldsymbol{E}(\omega)\big) \qquad [2\text{-}5]$$

This results in [2-6]:

$$-\boldsymbol{E}(2\omega) \propto -\boldsymbol{P}(2\omega) = \overleftrightarrow{\chi}^{(2)}\boldsymbol{E}(\omega)^{\mathbf{2}} \qquad [2\text{-}6]$$

The relationship between [2-4] and [2-6] demonstrates that, in materials with a center of inversion, $-\boldsymbol{E}(2\omega) = \boldsymbol{E}(2\omega)$ which is not possible. This indicates that the $\overleftrightarrow{\chi}^{(2)}$ tensor is therefore equal to 0 in a centrosymmetric material. This results in the SHG process being nonexistent and is therefore considered a forbidden process in materials with a center of inversion.

Additionally, the theoretical signal intensity for the SHG signal ($S(2\omega)$) can be calculated by:

$$S(2\omega) = \frac{(2\omega)^2}{8\varepsilon_0 c^3 cos^2\beta} \cdot \left|\overleftrightarrow{\chi}^{(2)}_{eff}\right|^2 [I(\omega)]^2 AT \quad [2\text{-}7]$$

where c is the speed of light, β is the exit angle of the SHG signal relative to the direction of the fundamental laser, $I(\omega)$ is the intensity at the fundamental frequency at the surface, *A* is the area of the beam on the surface of the material, and *T* is the pulse width of the laser at the fundamental frequency. The only variable in this equation is the effective nonlinear susceptibility tensor $|\overleftrightarrow{\chi}^{(2)}_{eff}|$, which can be isolated to give:[77]

$$\overleftrightarrow{\chi}^2_{eff} = \left(\vec{L}_{2\omega} \cdot \hat{e}_{2\omega}\right) \cdot \overleftrightarrow{\chi}^{(2)}_S : (\vec{L}_{\omega} \cdot \hat{e}_{\omega})(\vec{L}_{\omega} \cdot \hat{e}_{\omega}) \quad [2\text{-}8]$$

where L is the Fresnel factor at the fundamental (ω) and second harmonic (2ω) frequencies, $\overleftrightarrow{\chi}^{(2)}_S$ is the theoretical nonlinear susceptibility of the material, and $\hat{e}$ is the polarization vector at the fundamental (ω) and second harmonic (2ω) frequencies. Using [2-8], the polarization dependence of the SHG signal intensity can be shown for a material with a known point group with active $\overleftrightarrow{\chi}^{(2)}$ elements.

The surface roughness of a nanomaterial will also contribute a minute amount to the overall signal of the nonlinear optical response. This signal is minimal for smooth surfaces and increases with increasing surface roughness. Any adsorbents must also be factored in, whether it is a dielectric medium (*e.g.* air) or a hyperpolarizable molecule, such as malachite green.[78] The effective nonlinear susceptibility tensor can be described by:

$$\overleftrightarrow{\chi}^{(2)}_{eff} = \overleftrightarrow{\chi}^{(2)}_A + \overleftrightarrow{\chi}^{(2)}_B + \overleftrightarrow{\chi}^{(2)}_i \quad [2\text{-}9]$$

where $\overleftrightarrow{\chi}^{(2)}_A$ represents any adsorbed molecules to the surface, $\overleftrightarrow{\chi}^{(2)}_B$ represents the any contributions from the surface of the material (including from surface roughness), and $\overleftrightarrow{\chi}^{(2)}_i$ represents the interactions between the surface and the adsorbed molecules. In the case of hyperpolarizable molecules, however, the $\overleftrightarrow{\chi}^{(2)}_A$ term can be replaced with the hyperpolarizability term, β_{ijk}. The hyperpolarizability term is similar to $\overleftrightarrow{\chi}^{(2)}$ as it will

also be equal to zero when the molecule has a center of inversion (*e.g.* in molecular oxygen).

In this work, SHGM will be used to analyze the effects of LSPR modes on the intensity of the nonlinear optical processes' response. Furthermore, the SHG response in isotropic metamaterials with localized anisotropy is studied and compared to metamaterials without a center of inversion.

2.3.2 SHG in Nanomaterials

Nanofabrication methods offer the possibility of fabricating artificial materials that have the proper symmetry to become SHG active. In the past decade, a multitude of studies have been reported that demonstrate the SHG activity in nanomaterials. Ranging from structures that are inherently SHG active due to their non-centrosymmetric structure, to metamaterials that have been shaped with localized non-centrosymmetry, these metamaterials provide a versatile platform for enhanced SHGM.[79-81]

Nanosphere lithography (NSL) is an effective method to produce nanostructures that are SHG active. In NSL, arrays of nanoprisms in hexagonal arrangements using nanospheres as a template (Figure 2-7a). These individual nanoprisms have a C_3 symmetry and therefore no center of inversion. By virtue of this symmetry, they are ideal candidates for SHGM as produce large surface areas of SHG active nanomaterials. The SHG map shown in Figure 2-7b highlights the SHG emission from the individual prisms at a fundamental wavelength of 800 nm and the SHG wavelength at 400 nm.

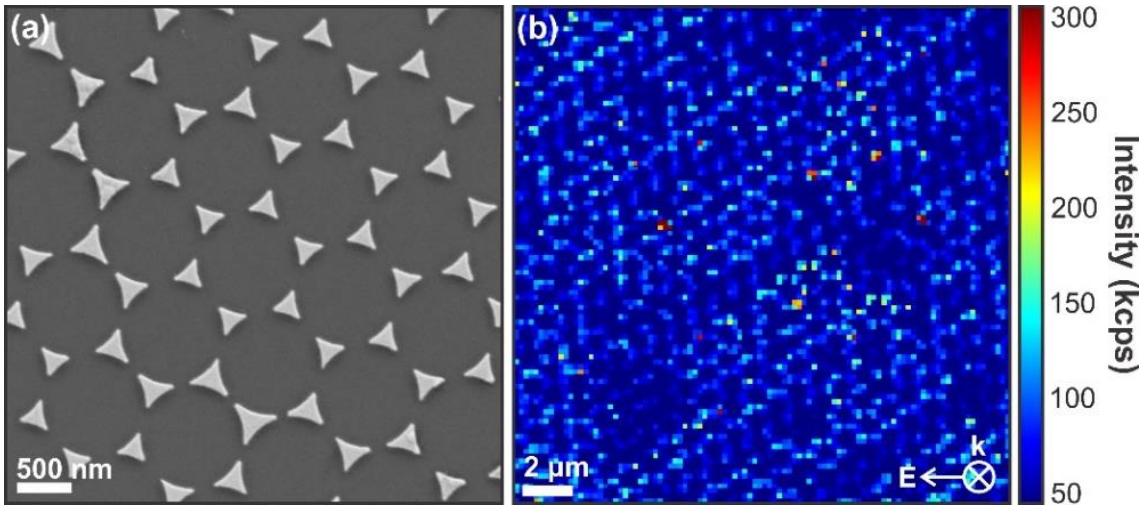

Figure 2-7 (a) An SEM image of a Fischer patterned substrate produced by NSL and (b) an SHGM image of a large surface area of an NSL substrate.

Another fabrication technique that can be used to generate SHG active nanomaterials is electron-beam lithography (EBL). This technique can generate nano- and metamaterials with a spatial resolution down to 10 nm. Metamaterials are produced to contain localized non-centrosymmetry in otherwise centrosymmetric structures. An example of this is a series of four circular nanodisks produced by Guo *et al.* that are equally spaced in y, but not in x (Figure 2-8).[82] The intensity of the hot spot along the x direction is significantly higher than that along the y direction. This discrepancy in the hot spots when the polarization direction changes is known as localized induced asymmetry (or non-centrosymmetry). This means that despite the individual structures having centres of inversion, the overall metamaterial does not.[82]

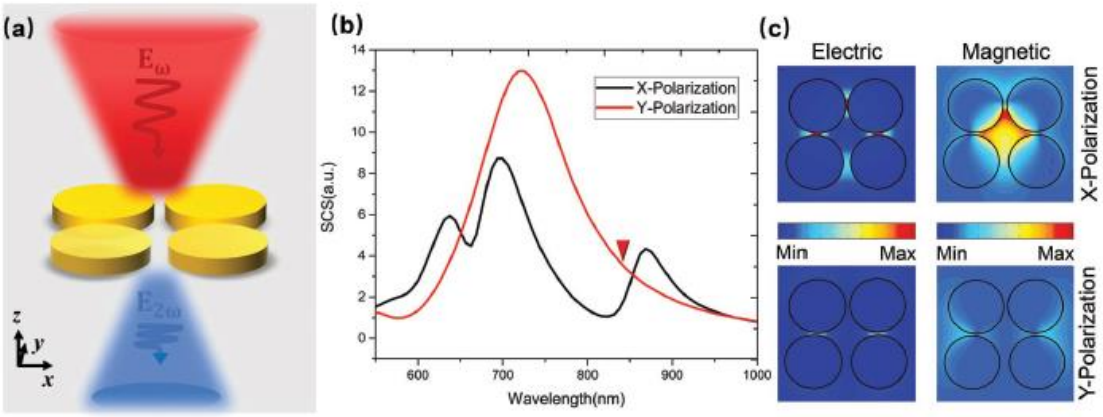

Figure 2-8 (a) Schematic of a bianisotropic metamolecule in which electromagnetic coupling could happen. The four Au nanodisks, each with radius of 50nm and a thickness of 30nm are symmetric along the y-axis asymmetric along the x-axis. Light is incident from the top of the metamaterial and the electric field polarizes along the x- or y-axis. (b) Linear scattering cross-section (SCS) of the metamolecule at the fundamental frequency under normal incident light with x- (black line) and y- (red line) polarization. The red arrow denotes the wavelength of the electromagnetic coupling under x-polarization. (c) Normalized electric and magnetic near-field distributions at the fundamental frequency denoted by the red arrow in (b). Top panels: x-polarization; bottom panels: y-polarization. © 2018 WILEY-VCH Verlag GmbH & Co. KGaA, Weinheim.

Metamaterials are of particular interest for nonlinear optics, as their nonlinear susceptibilities can effectively change the properties of the input light (*e.g.* frequency doubling). As shown in figure 2-5, the symmetry point group of a metamaterial of interest can be easily controlled when using advanced lithography techniques. In figure 2-4 a, b, and c, dendritic fractals, based on the Cayley tree structures first shown by *Halas et al.*,[83] with a point group of C_3, C_4, and C_5, respectively, are shown. While the overall point group of the metastructure dictates whether it will be SHG active or not, we also observe an SHG response in the structures with a C_4 symmetry. this is due to the breaking of the symmetry at localized areas on the structure. This is discussed in further detail in chapter 4.

2.3.3 Plasmon-Enhanced SHG

The SHG signal can be enhanced even further by tailoring nanomaterials so that they have LSPRs that match the fundamental and second-harmonic (SH) wavelengths.[28, 30]

Upon irradiation and excitation of a nanomaterial, the SH response will adopt a similar shape to that of the LSPR.[29] For example, if the quadrupolar mode of an Au nanosphere is excited, the polarization dependent SHG signal will show four lobes and the highest SHG intensity will occur where the areas of the electromagnetic enhancement are the highest (Figure 2-9).[28] Normally, a SHG from a spherical object would be forbidden. Due to the nanoscale size of the gold nanoparticle, the surface roughness, combined with the enhancement of the LSPR, will show an SHG signal.

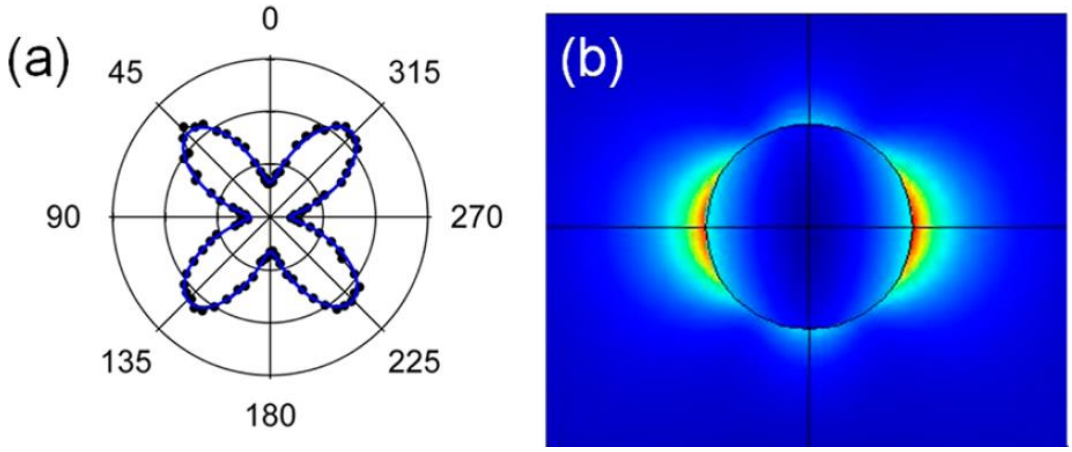

Figure 2-9 Multipolar emission from perfect nanospheres. (a) Experimental evidence of the SH quadrupolar emission from 150 nm gold nanoparticles and (b) the corresponding FDTD-calculated near-field enhancement intensity. Reprinted (adapted) with permission from Butet, J.; Brevet, P.-F.; Martin, O. J. F., ACS Nano 2015, 9, 10545-10562. Copyright 2015 American Chemical Society.

2.4 Plasmon-Mediated Chemistry

When the LSPRs on a metamaterial are excited, the small volumes where the enhanced field is confined to generates areas of electromagnetic enhancement which can has been exploited for photo-initiated surface reactions.[84, 85] After irradiation with a resonant

wavelength, these LSPRs will begin to decay. Their stored energy is released through two main decay pathways: light emission (*e.g.* fluorescence) or hot electron and thermal energy generation.[86-88] Through the hot electron decay pathway, a multitude of reactions can be catalyzed.[84-86] Examples of these reactions include surface functionalization,[89] such as sensor fabrication,[90, 91] polarization dependent grafting,[92] and plasmon-mediated nanohole drilling.[22] Furthermore, chemical reactions with a high societal impact can be performed at the surface including water splitting,[93-95] CO_2 reduction,[96-98] and artificial photosynthesis.[99-101] The field of plasmon-mediated surface chemistry is currently very dynamic and numerous surface reactions are under investigation using plasmon catalysis.[102]

2.4.1 The Hot Electron and Thermal Energy Decay of LSPRs

The radiative decay pathway occurs within 100 fs of excitation by the emission of a photon, typically through fluorescence.[103-105] The non-radiative decay pathway is the process in which hot electrons are generated and can be used in plasmon-mediated reactions.[106] The non-radiative decay has three stages (Figure 2-10).[107, 108] During its excitation, the nanomaterial will generate LSPRs, inducing a distribution in the electron density based on the excited resonance mode.[108]

After excitation, the generated LSPRs will undergo either radiative or non-radiative decay. The radiative decay involves the release of the excited energy by emission of photons. The nonradiative decay, however, is more complex involving a three-step decay pathway:[109]

Step 1 – charge carrier excitation (Figure 2-10, t = 1 – 100 fs): This first step, during which the charge carriers are excited, is crucial for plasmon-mediated chemistry as it produces hot electrons at the material's surface and are concentrated in the hot spots based on the excited LSPR mode. These hot electrons are capable of initiating photo-induced surface reactions.[102] During this stage, the delocalized electrons can interact with materials near the surface of the nanoparticle and are able to induce surface catalyzed and surface specific reactions.[110, 111]

Step 2 – charge carrier relaxation (Figure 2-10, t = 100 fs – 1 ps): The next step is charge carrier relaxation, during which the hot electron and hot "holes" (a positive charge or "hole" left by dislocated electrons) recombine. This results in both the relaxation of the electric field and the dissipation the acquired energy through heat. It has been shown that the heating step does not significantly contribute to the reaction at the surface.[109, 112] Furthermore, any thermal-induced reactions will be truncated by the quick dissipation of heat. The previously proposed mechanism for this reaction is the transfer of a radical from the Au surface to a reactive molecule, allowing reactions to occur without the need for a catalyst to be present.

Step 3 – thermal dissipation (Figure 2-10, t = 1 – 1000 ps): The final step is thermal dissipation, where the relaxation of the charge carriers in the nanomaterial releases the absorbed energy through heat. The heat released during the thermal dissipation can reach temperatures upwards of 400 K.[112-114]

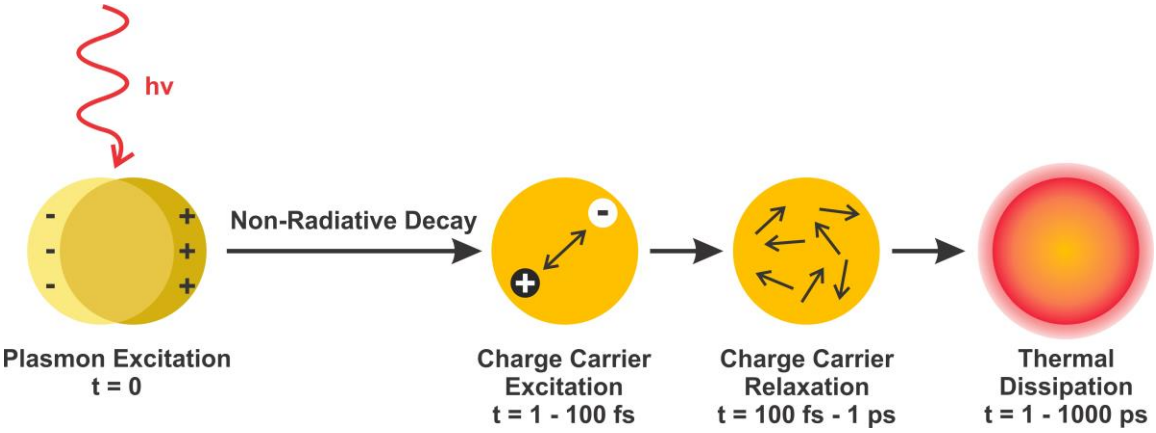

Figure 2-10 Illustration of the three stages of the non-radiative decay of an LSPR. At t = 0 is the irradiation of the nanoparticle, followed by t = 1 to 100 fs where in the charge carriers are excited, t = 100 fs to 1 ps where the charger carriers relax, and finally t = 1 – 1000 ps the thermal dissipation.

2.4.2 Selective Surface Chemical Reactions Using Hot Electrons

Surface functionalization of PMMA to visualize plasmon modes.

For example, Hobbes *et al.* uses Au nanorods and nanotriangles functionalized with PMMA through plasmonic excitation to visualize the dipolar modes of their structure. The spatial localization of the PMMA material reveals the area where the field intensity is the most confined, yielding surface reactions. This dipolar mode was demonstrated on nanorods to show the crosslinking and decomposition of the PMMA(Figure 2-11a-c), and nanotriangles to demonstrate the effect of the polarization on the dipolar mode and subsequent surface reactions (Figure 2-11d,e).[115]

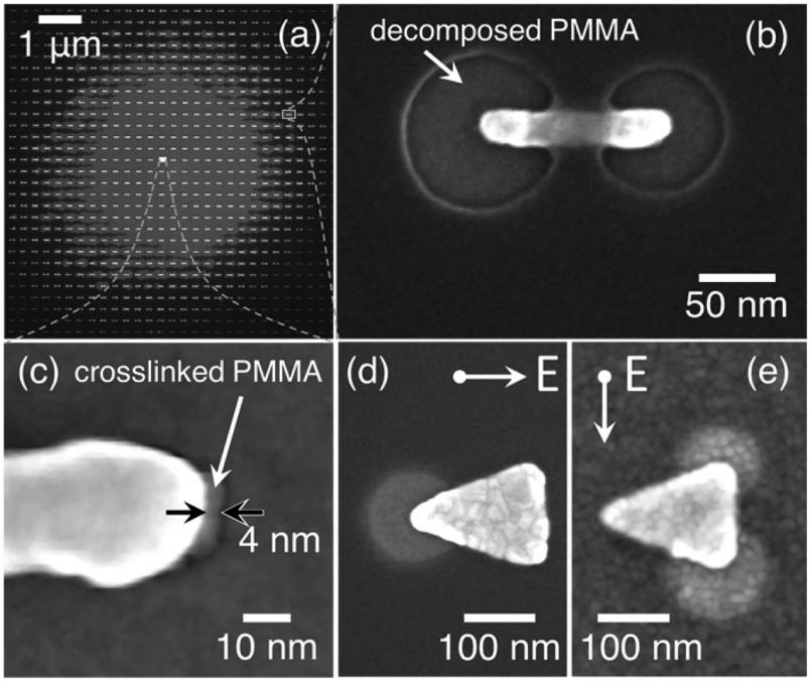

Figure 2-11 Imaging electron emission from plasmonic nanoantennae with PMMA. (a) Top-down SEM micrograph of a 260 nm pitch Au nanorod array coated with a 20 nm thick layer of PMMA. The coated array was previously exposed to ~10^9 fs laser pulses and the PMMA was subsequently developed. (b) SEM micrograph of a nanorod antenna near the periphery of the exposed region shown in panel (a) where regions of exposed and developed PMMA at the poles of the nanoantenna are visible. (c) SEM micrograph of a pole of a nanorod near the center of the exposed region in panel (a). A narrow strip of material believed to be cross-linked PMMA is present at the apex of the nanorod. (d, e) SEM micrographs of exposed PMMA around nanotriangles illuminated with ~10^9 fs laser pulses. The polarization of these

pulses was aligned(d) parallel to and (e) orthogonal to the long-axis of the nanotriangle antennae. Reprinted (adapted) with permission from Hobbs, R. G.; Putnam, W. P.; Fallahi, A.; Yang, Y.; Kärtner, F. X.; Berggren, K. K., Nano Lett. 2017, 17, 6069-6076. Copyright 2017 American Chemical Society.

Multiplexing guest molecules over metamaterials.

By varying the polarization of the input light, plasmon-mediated grafting can be employed for selectively exciting new plasmon modes and therefore enabling different molecular patterns on the surfaces.[89, 109, 116] This open up the possibility of multiplexing the functionalization of distinct analytes over the nanostructure using the polarization of the incoming light as a key tunability parameter.[10] Bachelot *et al.* used this approach over nanodisks to graft two formulations of a polymer that contain light-emitting quantum dots (Figure 2-12).[92] In this work, two polymers containing distinct light-emitting quantum dots were grafted along orthogonal directions using distinct polarization directions. The authors effectively demonstrated the polarization dependence of the emissions from the QDs (Figure 2-12f), allowing for real-time colour switching devices that depend only on the polarization of the input irradiation.[92]

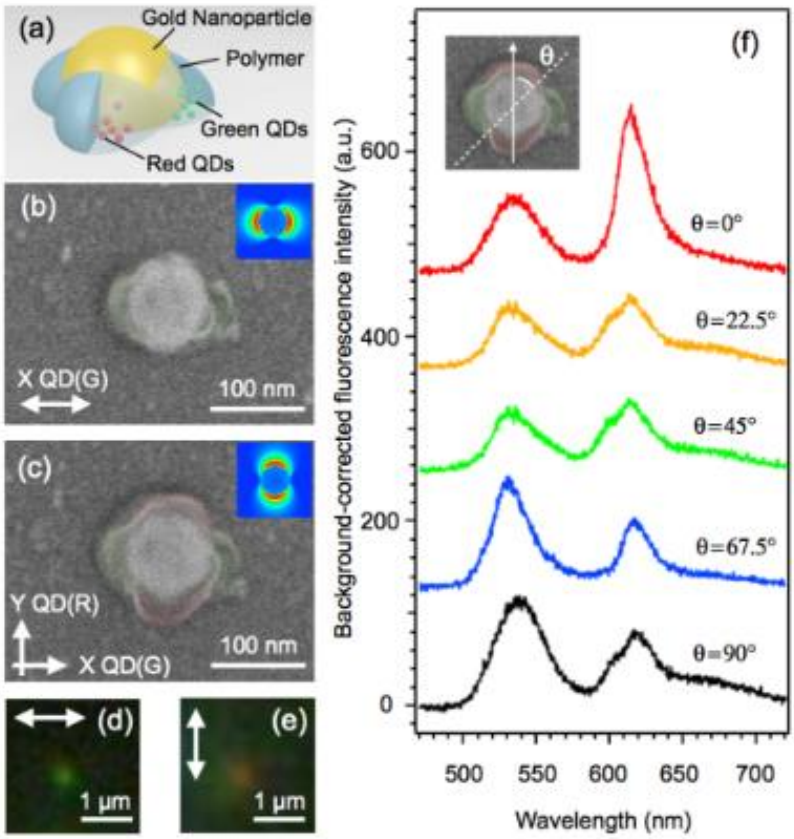

Figure 2-12 Topographic an optical characterization of a nanodisk-based two color anisotropic nanoemitter. (a) Schematic representation of the nanostructure. (b) SEM image of the Au nanodisk with a diameter of 90 nm after the first exposure that positions green QDs along the x-axis. (c) SEM image of the same nanodisk after the second exposure that traps red QDs along the y-axis. The respective plasmonic near-field intensities of the dipole emission for (b) and (c) are shown in each inset. For clarity, SEM images have been artificially colored according to the emission wavelengths of the trapped QDs. Far-field fluorescence image of the two-colour anisotropic nanoemitters (TCANE) under illumination with (d) x-axis polarization and (e) y-axis polarization. Double arrows represent the polarization of the excitation light. (f) Polarization-dependent fluorescence spectra from the TCANE. The polarizations of the excitation light (λ_{exc} = 405 nm) were at θ=0° (red plot), 22.5° (orange plot), 45° (green plot), 67.5° (blue plot), and 90° (black plot) with respect to the y-axis. The inset defines the polarization angle θ, where the dashed line represents the incident polarization direction. Reprinted (adapted) with permission

from Zhou, X.; Wenger, J.; Viscomi, F. N.; Le Cunff, L.; Béal, J.; Kochtcheev, S.; Yang, X.; Wiederrecht, G. P.; Colas des Francs, G.; Bisht, A. S.; Jradi, S.; Caputo, R.; Demir, H. V.; Schaller, R. D.; Plain, J.; Vial, A.; Sun, X. W.; Bachelot, R., Nano Lett. 2015, 15, 7458-7466. Copyright 2015 American Chemical Society.

Chapter 7 of this thesis details a cross-like metamaterial with the potential to graft up to three distinct patterns at the metamaterial's surface.[10] furthermore, Multiplexing has been previously used to graft two different diazonium salts to the surface of a single Au nanodisk.[117] In the work done by *Félidj et al.* on these Au nanodisks, two diazonium salts with distinguishable moieties were grafted to a single nanodisk using perpendicular polarizations. Along the Y axis, a diazonium salt containing a carboxyphenyl moiety was grafted, followed by a diazonium salt with a hydroxyethyl phenyl moiety along the X axis. The Raman spectra confirmed the presence of both moieties after the irradiations were completed, demonstrating a successful multiplexing. Atomic force microscopy cross-sections shown in Figure 2-13a,c (blue and red dashed lines) confirmed the addition of the diazonium salt layers by an increase of thickness of +/- 35 nm in both the X and Y directions.

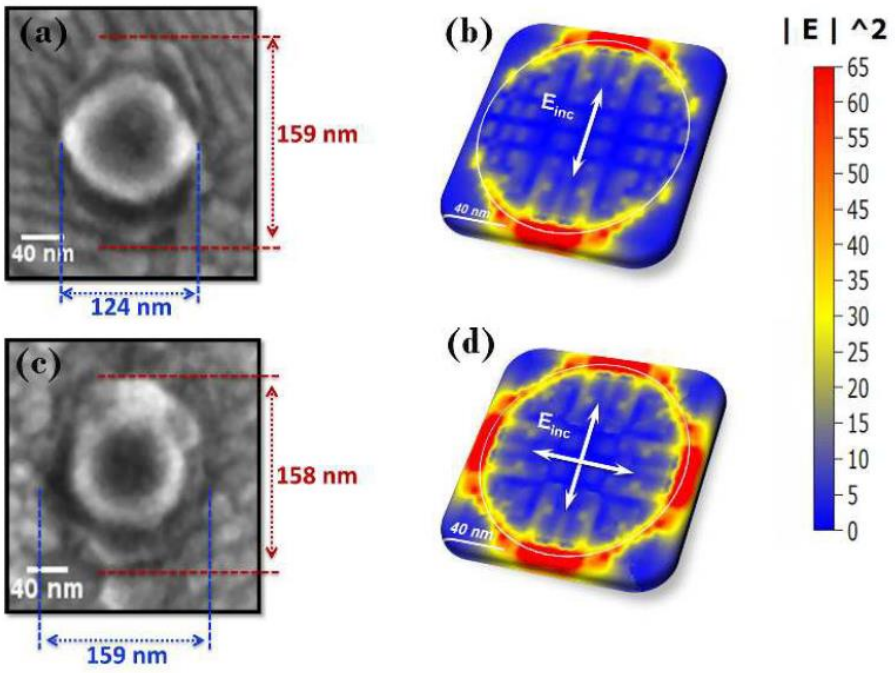

Figure 2-13 SEM images of a single nanoparticle after plasmon-induced grafting of (a) carboxyphenyl layers along the Y axis and (c) additional hydroxyethyl phenyl layers along the X direction. Irradiation conditions: λ_{inc} = 633 nm, 180 seconds with a power of P=0.8 mW/µm^2. Mapping of the near field intensity enhancement $|E|^2$ upon irradiation along the Y axis (b) and both X and Y axis (d), on a unit cell nanodisk of 100 nm, H = 50 nm, using the DDA method.

2.5 Summary

In this chapter, the fundamentals of plasmonics and its applications to optical and chemical processes were reviewed. Nanomaterials with second-order non-linear properties, including metamaterials, were described. The calculation of the electromagnetic field in the vicinity of these artificial structures using FDTD is explained for both the linear and nonlinear optical response of nanomaterials to an impinging field. Following this, the principles of SHG were given, including the enhancement and polarization dependence of this nonlinear optical process using LSPRs. Finally, chemical reactions at the surface of metamaterials were discussed highlighting the distinct pathways of plasmon-mediated reactions.

2.6 References

1. Pines, D.; Bohm, D., *Phys. Rev.* **1952,** *85*, 338-353.

2. Barchiesi, D.; Grosges, T., *J. Nanophoton.* **2014,** *8*, 083097.

3. Jing, J.-Y.; Wang, Q.; Zhao, W.-M.; Wang, B.-T., *Opt. Laser. Eng.* **2019,** *112*, 103-118.

4. Robatjazi, H.; Zhao, H.; Swearer, D. F.; Hogan, N. J.; Zhou, L.; Alabastri, A.; McClain, M. J.; Nordlander, P.; Halas, N. J., *Nat. Commun.* **2017,** *8*, 27.

5. Jia, Y.; Li, Z.; Wang, H.; Saeed, M.; Cai, H., *Sensors* **2020,** *20*, 131.

6. Ukhtary, M. S.; Saito, R., *Carbon* **2020,** *167*, 455-474.

7. Epstein, I.; Alcaraz, D.; Huang, Z.; Pusapati, V.-V.; Hugonin, J.-P.; Kumar, A.; Deputy, X. M.; Khodkov, T.; Rappoport, T. G.; Hong, J.-Y.; Peres, N. M. R.; Kong, J.; Smith, D. R.; Koppens, F. H. L., *Science* **2020,** *368*, 1219-1223.

8. Islam, M. S.; Sultana, J.; Biabanifard, M.; Vafapour, Z.; Nine, M. J.; Dinovitser, A.; Cordeiro, C. M. B.; Ng, B. W. H.; Abbott, D., *Carbon* **2020,** *158*, 559-567.

9. Zhang, C.; Wang, Y.; Liang, Y.; Zhu, Y.; Li, Z.; Huang, X.; Lu, G., *J. Phys. Chem. Lett.* **2020,** *11*, 7650-7656.

10. Therien, D. A. B.; McRae, D. M.; Mangeney, C.; Félidj, N.; Lagugné-Labarthet, F., *Nanoscale Adv.* **2021,** *3*, 2501-2507.

11. Luo, Y.; Xiao, Y.; Onidas, D.; Iannazzo, L.; Ethève-Quelquejeu, M.; Lamouri, A.; Félidj, N.; Mahouche-Chergui, S.; Brulé, T.; Gagey-Eilstein, N.; Gazeau, F.; Mangeney, C., *Chem. Comm.* **2020,** *56*, 6822-6825.

12. Li, D.; Yao, D.; Li, C.; Luo, Y.; Liang, A.; Wen, G.; Jiang, Z., *TRAC-Trend. Anal. Chem.* **2020,** *127*, 115885.

13. Perumal, J.; Wang, Y.; Attia, A. B. E.; Dinish, U. S.; Olivo, M., *Nanoscale* **2021,** *13*, 553-580.

14. McRae, D. M.; Lagugné-Labarthet, F., *Nat. Nanotechnol.* **2019,** *14*, 922-923.

15. Wallace, G. Q.; Lagugné-Labarthet, F., *Analyst* **2019,** *144*, 13-30.

16. Adato, R.; Aksu, S.; Altug, H., *Mater. Today Commun.* **2015,** *18*, 436-446.

17. Seiça, A. F. S.; Iqbal, M. H.; Carvalho, A.; Choe, J.-y.; Boulmedais, F.; Hellwig, P., *ACS Sensors* **2021,** *6*, 2875-2882.

18. Tseng, M. L.; Jahani, Y.; Leitis, A.; Altug, H., *ACS Photonics* **2021,** *8*, 47-60.

19. Zrimsek, A. B.; Chiang, N.; Mattei, M.; Zaleski, S.; McAnally, M. O.; Chapman, C. T.; Henry, A.-I.; Schatz, G. C.; Van Duyne, R. P., *Chem. Rev.* **2017,** *117*, 7583-7613.

20. Verma, P., *Chem. Rev.* **2017,** *117*, 6447-6466.

21. Kajendirarajah, U.; Olivia Avilés, M.; Lagugné-Labarthet, F., *Phys. Chem. Chem. Phys.* **2020,** *22*, 17857-17866.

22. McRae, D. M.; Jeon, K.; Lagugné-Labarthet, F., *ACS Omega* **2018,** *3*, 7269-7277.

23. Lu, G.; Xu, J.; Wen, T.; Zhang, W.; Zhao, J.; Hu, A.; Barbillon, G.; Gong, Q., *Materials* **2018,** *11*, 1435.

24. Šubr, M.; Praus, P.; Kuzminova, A.; Kočišová, E.; Kylián, O.; Sureau, F.; Procházka, M.; Štěpánek, J., *Nanomaterials* **2020,** *10*, 773.

25. Fort, E.; Grésillon, S., *J. Phys. D Appl. Phys.* **2008,** *41*, 13001-31.

26. Sugita, A.; Nakatsuka, Y.; Ono, A.; Inami, W.; Kawata, Y. In *Enhanced SHG due to hybridized plasmons in Au nanotrimer structures*, Conf. Lasers Electro-Optics, Washington, DC, 2020/05/10; Optical Society of America: Washington, DC, 2020; p FM2D.5.

27. Shen, S.; Shan, J.; Shih, T.-M.; Han, J.; Ma, Z.; Zhao, F.; Yang, F.; Zhou, Y.; Yang, Z., *Phys. Rev. Appl.* **2020,** *13*, 024045.

28. Butet, J.; Brevet, P.-F.; Martin, O. J. F., *ACS Nano* **2015,** *9*, 10545-10562.

29. Valev, V. K., *Langmuir* **2012,** *28*, 15454-15471.

30. Therien, D. A. B.; Hou, R.; Lagugné-Labarthet, F., *Plasmonics* **2020,** *15*, 507-515.

31. Mayer, K. M.; Hafner, J. H., *Chem. Rev.* **2011,** *111*, 3828-3857.

32. Jing, J.-Y.; Wang, Q.; Zhao, W.-M.; Wang, B.-T., *Optics and Lasers in Engineering* **2019,** *112*, 103-118.

33. Chen, Y.; Ming, H., *Photonic Sens.* **2012,** *2*, 37-49.

34. Cao, J.; Sun, T.; Grattan, K. T. V., *Sens. Actuators B Chem.* **2014,** *195*, 332-351.

35. Golibrzuch, M.; Maier, T. L.; Feil, M. J.; Krischer, K.; Becherer, M., *J. Appl. Phys.* **2022,** *131*, 124301.

36. Kim, J.; Lee, J. S.; Kim, J.-w.; De Wolf, P.; Moon, S.; Kim, D. H.; Song, J.-H.; Kim, J.; Kim, T.; Nam, S. H.; Suh, Y. D.; Kim, K.-H.; Kim, H.; Shin, C., *Nanoscale* **2021,** *13*, 4475-4484.

37. Rachkov, A. G.; Schimpf, A. M., *Chem. Mater.* **2021,** *33*, 1394-1406.

38. Chapagain, P.; Guisbiers, G.; Kusper, M.; Geoffrion, L. D.; Benamara, M.; Golden, A.; Bachri, A.; Hewavitharana, L., *ACS Omega* **2021,** *6*, 6871-6880.

39. Li, Y.-Y.; Zhong, C.-Y.; Li, M.-X.; Zhang, Q.-Y.; Chen, Y.; Liu, Z.-Q.; Zhang, J. Z., *J. Mater. Chem. C* **2021,** *9*, 1614-1621.

40. Yang, J.; Sun, Q.; Yu, H.; Ueno, K.; Misawa, H.; Gong, Q., *Photonics Res.* **2017,** *5*, 187-193.

41. Lin, S.; Li, M.; Dujardin, E.; Girard, C.; Mann, S., *Adv. Mater.* **2005,** *17*, 2553-2559.

42. Nordlander, P.; Oubre, C.; Prodan, E.; Li, K.; Stockman, M. I., *Nano Lett.* **2004,** *4*, 899-903.

43. Langer, J.; Jimenez de Aberasturi, D.; Aizpurua, J.; Alvarez-Puebla, R. A.; Auguié, B.; Baumberg, J. J.; Bazan, G. C.; Bell, S. E. J.; Boisen, A.; Brolo, A. G.; Choo, J.; Cialla-May, D.; Deckert, V.; Fabris, L.; Faulds, K.; García de Abajo, F. J.; Goodacre, R.; Graham, D.; Haes, A. J.; Haynes, C. L.; Huck, C.; Itoh, T.; Käll, M.; Kneipp, J.; Kotov, N. A.; Kuang, H.; Le Ru, E. C.; Lee, H. K.; Li, J.-F.; Ling, X. Y.; Maier, S. A.; Mayerhöfer, T.; Moskovits, M.; Murakoshi, K.; Nam, J.-M.; Nie, S.; Ozaki, Y.; Pastoriza-Santos, I.; Perez-Juste, J.; Popp, J.; Pucci, A.; Reich, S.; Ren, B.; Schatz, G. C.; Shegai, T.; Schlücker, S.; Tay, L.-L.; Thomas, K. G.; Tian, Z.-Q.; Van Duyne, R. P.; Vo-Dinh, T.; Wang, Y.; Willets, K. A.; Xu, C.; Xu, H.; Xu, Y.; Yamamoto, Y. S.; Zhao, B.; Liz-Marzán, L. M., *ACS Nano* **2020,** *14*, 28-117.

44. Ringe, E.; Langille, M. R.; Sohn, K.; Zhang, J.; Huang, J.; Mirkin, C. A.; Van Duyne, R. P.; Marks, L. D., *J. Phys. Chem. Lett.* **2012,** *3*, 1479-1483.

45. Remesh, V.; Stührenberg, M.; Saemisch, L.; Accanto, N.; Hulst, N. F. v., *Appl. Phys. Lett.* **2018,** *113*, 211101.

46. Wang, Z.; Dong, Z.; Zhu, H.; Jin, L.; Chiu, M.-H.; Li, L.-J.; Xu, Q.-H.; Eda, G.; Maier, S. A.; Wee, A. T. S.; Qiu, C.-W.; Yang, J. K. W., *ACS Nano* **2018,** *12*, 1859-1867.

47. Ghirardini, L.; Baudrion, A.-L.; Monticelli, M.; Petti, D.; Biagioni, P.; Duò, L.; Pellegrini, G.; Adam, P.-M.; Finazzi, M.; Celebrano, M., *J. Phys. Chem. C* **2018,** *122*, 11475-11481.

48. Madzharova, F.; Öhl, D.; Junqueira, J.; Schuhmann, W.; Kneipp, J., *Adv. Opt. Mater.* **2019,** *7*, 1900650.

49. Simovski, C. R., *Opt. Spectrosc.* **2009,** *107*, 726.

50. Neubrech, F.; Huck, C.; Weber, K.; Pucci, A.; Giessen, H., *Chem. Rev.* **2017,** *117*, 5110-5145.

51. Yoo, S.; Park, Q.-H., *Nanophotonics* **2019,** *8*, 249-261.

52. Warning, L. A.; Miandashti, A. R.; McCarthy, L. A.; Zhang, Q.; Landes, C. F.; Link, S., *ACS Nano* **2021,** *15*, 15538-15566.

53. Wu, W.; Hu, W.; Qian, G.; Liao, H.; Xu, X.; Berto, F., *Mater. Des.* **2019,** *180*, 107950.

54. Gómez-Castaño, M.; Garcia-Pomar, J. L.; Pérez, L. A.; Shanmugathasan, S.; Ravaine, S.; Mihi, A., *Adv. Opt. Mater.* **2020,** *8*, 2000865.

55. Papadakis, G. T.; Fleischman, D.; Davoyan, A.; Yeh, P.; Atwater, H. A., *Nat. Comm.* **2018,** *9*, 296.

56. Islam, S. S.; Hasan, M. M.; Faruque, M. R. I., *Appl. Phys. A* **2018,** *124*, 160.

57. Manjappa, M.; Pitchappa, P.; Wang, N.; Lee, C.; Singh, R., *Adv. Opt. Mater.* **2018,** *6*, 1800141.

58. Liu, P.; Liang, Z.; Lin, Z.; Xu, Z.; Xu, R.; Yao, D.; Lin, Y.-S., *Sci. Rep.* **2019,** *9*, 9917.

59. Higgins, S. G.; Becce, M.; Belessiotis-Richards, A.; Seong, H.; Sero, J. E.; Stevens, M. M., *Adv. Mater.* **2020,** *32*, 1903862.

60. Wang, P.; Nasir, M. E.; Krasavin, A. V.; Dickson, W.; Jiang, Y.; Zayats, A. V., *Acc. Chem. Res.* **2019,** *52*, 3018-3028.

61. Kravets, V. G.; Schedin, F.; Jalil, R.; Britnell, L.; Gorbachev, R. V.; Ansell, D.; Thackray, B.; Novoselov, K. S.; Geim, A. K.; Kabashin, A. V.; Grigorenko, A. N., *Nat. Mater.* **2013,** *12*, 304-309.

62. Savin, A.; Bruma, A.; Steigmann, R.; Iftimie, N.; Faktorova, D., *Appl. Sci.* **2015,** *5*, 1412-1430.

63. Lafuente, M.; Berenschot, E. J. W.; Tiggelaar, R. M.; Rodrigo, S. G.; Mallada, R.; Tas, N. R.; Pina, M. P., *Microchim. Acta* **2020,** *187*, 247.

64. Marshall, A. R. L.; Stokes, J.; Viscomi, F. N.; Proctor, J. E.; Gierschner, J.; Bouillard, J.-S. G.; Adawi, A. M., *Nanoscale* **2017,** *9*, 17415-17421.

65. Zhang, Y.; Zhao, J.; Cao, J.; Mao, B., *Sensors* **2018,** *18*, 1912.

66. Marin, B. C.; Ramírez, J.; Root, S. E.; Aklile, E.; Lipomi, D. J., *Nanoscale Horiz.* **2017,** *2*, 311-318.

67. Roh, Y.; Lee, S.-H.; Kwak, J.; Song, H. S.; Shin, S.; Kim, Y. K.; Wu, J. W.; Ju, B.-K.; Kang, B.; Seo, M., *Sens. Actuators B Chem.* **2022,** *352*, 130993.

68. Near, R.; Hayden, S.; El-Sayed, M., *J. Phys. Chem. C* **2012,** *116*, 23019-23026.

69. Hou, R.; Shynkar, V.; Lafargue, C.; Kolkowski, R.; Zyss, J.; Lagugné-Labarthet, F., *Phys. Chem. Chem. Phys.* **2016,** *18*, 7956-7965.

70. Berline, I.; Fiorini-Debuisschert, C.; Royal, C.; Douillard, L.; Charra, F., *J Appl. Phys.* **2008,** *104*, 103113.

71. Krause, D.; Teplin, C. W.; Rogers, C. T., *J. Appl. Phys.* **2004,** *96*, 3626-3634.

72. Franken, P. A.; Hill, A. E.; Peters, C. W.; Weinreich, G., *Phys. Rev. Lett.* **1961,** *7*, 118-119.

73. Bierlein, J. D.; Vanherzeele, H., *J. Opt. Soc. Am. B* **1989,** *6*, 622-633.

74. Shukla, V. K.; Ghosh, J., *Phys. Rev. A* **2020,** *101*, 023832.

75. Sorokina, N. I.; Voronkova, V. I., *Crystallogr. Rep.* **2007,** *52*, 80-93.

76. Reddy, R. R.; Nazeer Ahammed, Y.; Rama Gopal, K.; Abdul Azeem, P.; Rao, T. V. R.; Mallikarjuna Reddy, P., *Opt. Mater.* **2000,** *14*, 355-358.

77. Labarthet, F. L.; Shen, Y. R., Nonlinear Optical Microscopy. In *Optical Imaging and Microscopy: Techniques and Advanced Systems*, Török, P.; Kao, F.-J., Eds. Springer Berlin Heidelberg: Berlin, Heidelberg, 2003; pp 169-196.

78. Kikteva, T.; Star, D.; Leach, G. W., *J. Phys. Chem. B* **2000,** *104*, 2860-2867.

79. Ren, S.; Chen, Z.; Li, S.; Wang, S.; Zhao, Z.; Zhao, Y.; Hu, R.; Qu, J.; Liu, L., *Opt. Mater. Express* **2021,** *11*, 3223-3231.

80. Yang, Y.; liu, W. G.; Lin, Z. T.; Pan, R. H.; Gu, C. Z.; Li, J. J., *Mater. Today Phys.* **2021,** *17*, 100343.

81. Deng, J.; Tang, Y.; Chen, S.; Li, K.; Zayats, A. V.; Li, G., *Nano Lett.* **2020,** *20*, 5421-5427.

82. Guo, K.; Qian, C.; Zhang, Y. L.; Fung, K. H., *Adv. Opt. Mater.* **2018,** *6*, 1701154.

83. Gottheim, S.; Zhang, H.; Govorov, A. O.; Halas, N. J., *ACS Nano* **2015,** *9*, 3284-3292.

84. Kailasa, S. K.; Koduru, J. R.; Desai, M. L.; Park, T. J.; Singhal, R. K.; Basu, H., *TRAC-Trend. Anal. Chem.* **2018,** *105*, 106-120.

85. Stewart, S.; Wei, Q.; Sun, Y., *Chem. Sci.* **2021,** *12*, 1227-1239.

86. Jian, C.-c.; Zhang, J.; He, W.; Ma, X., *Nano Energy* **2021,** *82*, 105763.

87. Farcau, C.; Craciun, A.-M.; Vallée, R. A. L., *J. Chem. Phys.* **2020,** *153*, 164701.

88. Zhang, Y.; Chen, W.; Fu, T.; Sun, J.; Zhang, D.; Li, Y.; Zhang, S.; Xu, H., *Nano Lett.* **2019,** *19*, 6284-6291.

89. Nguyen, M.; Lamouri, A.; Salameh, C.; Lévi, G.; Grand, J.; Boubekeur-Lecaque, L.; Mangeney, C.; Félidj, N., *Nanoscale* **2016,** *8*, 8633-8640.

90. Ghodselahi, T.; Neishaboorynejad, T.; Arsalani, S., *Appl. Surf. Sci.* **2015,** *343*, 194-201.

91. Chen, J.-S.; Chen, P.-F.; Lin, H. T.-H.; Huang, N.-T., *Analyst* **2020,** *145*, 7654-7661.

92. Zhou, X.; Wenger, J.; Viscomi, F. N.; Le Cunff, L.; Béal, J.; Kochtcheev, S.; Yang, X.; Wiederrecht, G. P.; Colas des Francs, G.; Bisht, A. S.; Jradi, S.; Caputo, R.; Demir, H. V.; Schaller, R. D.; Plain, J.; Vial, A.; Sun, X. W.; Bachelot, R., *Nano Lett.* **2015,** *15*, 7458-7466.

93. Yan, L.; Xu, J.; Wang, F.; Meng, S., *J. Phys. Chem. Lett.* **2018,** *9*, 63-69.

94. Vahidzadeh, E.; Zeng, S.; Alam, K. M.; Kumar, P.; Riddell, S.; Chaulagain, N.; Gusarov, S.; Kobryn, A. E.; Shankar, K., *ACS Appl. Mater. Interfaces* **2021,** *13*, 42741-42752.

95. Zhang, P.; Liu, H.; Li, X., *Appl. Surf. Sci.* **2021,** *559*, 149865.

96. Yang, J.; Guo, Y.; Lu, W.; Jiang, R.; Wang, J., *Adv. Mater.* **2018,** *30*, 1802227.

97. Le, T.; Shao, Y.; Wang, B., *J. Phys. Chem. C* **2021,** *125*, 6108-6115.

98. Humayun, M.; Ullah, H.; Shu, L.; Ao, X.; Tahir, A. A.; Wang, C.; Luo, W., *Nano-Micro Lett.* **2021,** *13*, 209.

99. Xiao, C.; Hu, H.; Zhang, X.; MacFarlane, D. R., *ACS Sustain. Chem. Eng.* **2017,** *5*, 10858-10863.

100. Kim, Y. J.; Moon, G.; Hong, H.; Yun, J.; Kim, S. I.; Chae, Y.; Kim, D.; Ryu, W., *J. Mater. Chem. A* **2020,** *8*, 24192-24203.

101. Kim, Y. J.; Hong, H.; Yun, J.; Kim, S. I.; Jung, H. Y.; Ryu, W., *Adv. Mater.* **2021,** *33*, 2005919.

102. Martirez, J. M. P.; Bao, J. L.; Carter, E. A., *Annu. Rev. Phys. Chem.* **2021,** *72*, 99-119.

103. Forestiere, C.; Miano, G.; Pascale, M.; Tricarico, R., *Phys. Rev. A* **2020,** *102*, 043704.

104. Zhang, W.; Lei, H., *Nanoscale* **2020,** *12*, 6596-6602.

105. Gamal, M.; Kandas, I.; Badran, H.; Hajjiah, A.; Muhammed, M.; Shehata, N., *Nanomaterials* **2021,** *11*, 1928.

106. Christopher, P.; Moskovits, M., *Annu. Rev. Phys. Chem.* **2017,** *68*, 379-398.

107. Brongersma, M. L.; Halas, N. J.; Nordlander, P., *Nat. Nanotechnol.* **2015,** *10*, 25-34.

108. Li, X.; Xiao, D.; Zhang, Z., *New J. Phys.* **2013,** *15*, 023011.

109. Kameche, F.; Heni, W.; Telitel, S.; Vidal, L.; Marguet, S.; Douillard, L.; Fiorini-Debuisschert, C.; Bachelot, R.; Soppera, O., *J. Phys. Chem. C* **2021,** *125*, 8719-8731.

110. Bléteau, P.; Bastide, M.; Gam-Derouich, S.; Martin, P.; Bonnet, R.; Lacroix, J.-C., *ACS Appl. Nano Mater.* **2020,** *3*, 7789-7794.

111. Kazuma, E.; Jung, J.; Ueba, H.; Trenary, M.; Kim, Y., *Science* **2018,** *360*, 521-526.

112. Keller, E. L.; Frontiera, R. R., *ACS Nano* **2018,** *12*, 5848-5855.

113. Furube, A.; Hashimoto, S., *NPG Asia Mater.* **2017,** *9*, e454-e454.

114. Un, I.-W.; Sivan, Y., *ACS Photonics* **2021,** *8*, 1183-1190.

115. Hobbs, R. G.; Putnam, W. P.; Fallahi, A.; Yang, Y.; Kärtner, F. X.; Berggren, K. K., *Nano Lett.* **2017,** *17*, 6069-6076.

116. Minamimoto, H.; Toda, T.; Murakoshi, K., *Nanoscale* **2021,** *13*, 1784-1790.

117. Tijunelyte, I.; Kherbouche, I.; Gam-Derouich, S.; Nguyen, M.; Lidgi-Guigui, N.; de la Chapelle, M. L.; Lamouri, A.; Lévi, G.; Aubard, J.; Chevillot-Biraud, A.; Mangeney, C.; Felidj, N., *Nanoscale Horiz.* **2018,** *3*, 53-57.

Chapter 3

3 Methodology

This chapter discusses the techniques and instrumentation used throughout this thesis which include finite-difference time-domain modelling, absorbance measurements, electron-beam lithography, and second-harmonic generation microscopy (SHGM). The functionalization of surfaces and chemical vapour deposition are also described. The design and fabrication of metamaterials that are capable of efficiently interacting with an impinging field, involve a combination of simulations, lithographic techniques, and characterization processes. This allows the metamaterials to exhibit LSPRs at specific wavelengths which can be accurately tuned to any desired wavelength and can exhibit upwards of three LSPR modes in the visible range.[1-3]

3.1 Finite-Difference Time-Domain (FDTD) Modelling

The FDTD measurements in this thesis were performed using the Ansys Lumerical software. The typical setup for the modelling of metastructures contains six key components:

- The FDTD region is a 3D space wherein all components of the simulation are placed, as shown by the orange box in Figure 3-1a. The FDTD region will divide the volume into Yee cells of a predetermined volume. This space contains boundaries in the x-, y-, and z-directions that can be used to set up a variety of situations. By using a perfectly matched layer (PML) boundary condition, any light that passes through this boundary is absorbed, effectively minimizing unwanted reflections. The PML boundary condition is typically used in the z-direction for the modelling of the studied structures. The periodic boundary conditions can be used to model arrays of structures with a reduced simulation time and memory requirement. The periodic boundary conditions will generate an effectively infinite array of the structure contained within the FDTD region and analyze the response of the single structure within a repeating system.

- The mesh is used to divide a designated volume of the FDTD region into smaller Yee cells, as described in Chapter 2, section 2-2, thus producing a higher concentration of cells for the encapsulated volume, as shown by the red box in Figure 3-1a. The mesh works by filling the Yee cells that contain the structure with the desired optical parameters. However, if the Yee cell only contains a small portion of the structure, the entire cell is filled by the material. By using a smaller mesh size, the edges of the structure will be more accurately modelled, particularly when working with rounded objects.

- The light source used throughout the modelling of the studied metastructures was a plane wave light source, as shown by the white box in Figure 3-1a. This allowed an even distribution of the impinging field across the surface of the structure. The polarization of the electric field can be modified, as indicated by the blue arrow in Figure 3-1a, and circularly polarized light can be simulated by using two orthogonal light sources with a phase shift of either + or – 90°. The modelling is normalized to the intensity of this plane wave light source. The green arrow in Figure 3-1a indicates the polarization direction of the magnetic field, and the pink arrow (unobserved) indicates the propagation direction of the light.

- The absorption analysis group is a series of 6 boundaries, one in each axis direction, four of which shown by the yellow box in Figure 3-1a. These boundaries work by enclosing the modelled structure and monitoring the evolution of the plane wave light source as it passes through the modelled structure. they then calculate different optical properties of the modelled structure, including cross-section, abruption, and transmission.

- The areas of electromagnetic enhancement are done using a 2D frequency domain power monitor placed at the surface of the modelled structure, as shown by the blue box in Figure 3-1a. This monitor can be set to acquire the integrated power at the surface of the metastructures for a set wavelength. This produces a 2D image of the hotspots with a resolution determined by the concentration of Yee cells within the area.

- The optical parameters for the modelling of the studied structures were set as described Chapter 2, section 2.2. These parameters are set for each object, for example the Au nanodisk as shown by the yellow circle in Figure 3-1a. The structures can be generated using 3D objects designed by Lumerical as well as imported 2D coordinates from a GDSII file and adding the height in the z-direction. Both methods allow a fine control of the structural parameters. Furthermore, bitmap images can be imported to produce an object based the pixel colours of a black and white image. This is particularly useful for importing scanning electron microscopy images into the modelling software to help compensate for structural defects on fabricated structures, this is exhibited in Chapter 7 for the crosshair structures.

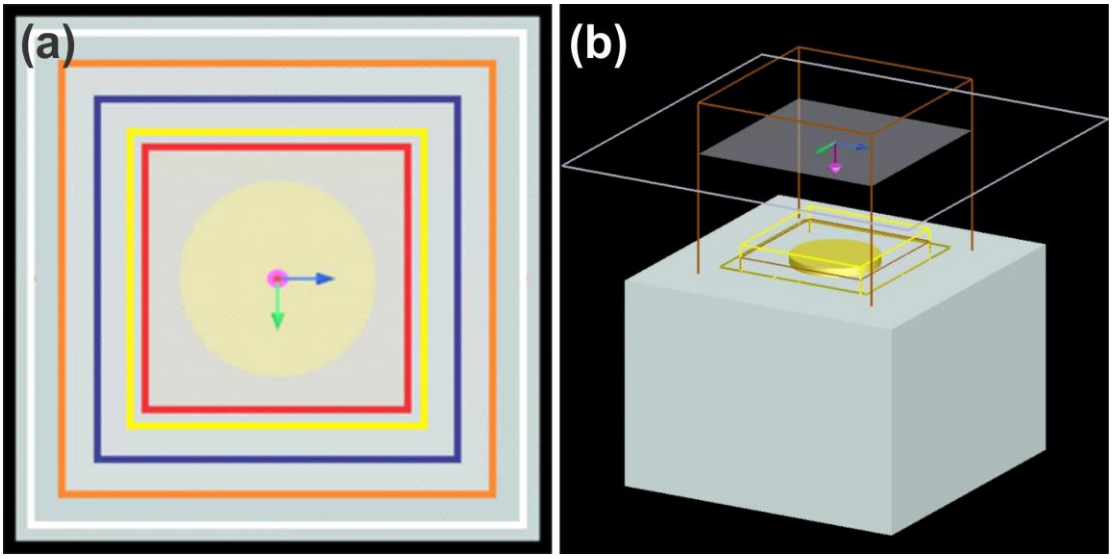

Figure 3-1 (a) A top-down view of the FDTD simulation region for an Au nanodisk. The gray rectangle represents the glass substrate, the white box represents the light source, the orange box represents the FDTD simulation region, the blue box represents the frequency domain power monitor, the yellow box represents the absorption monitors for the x and y axes, the red box represents the mesh, and the yellow circle represents the Au nanodisk. (b) a 3D view of the FDTD region.

Typically, the substrate and the light source are extended past the limits of the FDTD region, ensuring they are uniform and are considered infinitely large compared to the metastructure, as shown in Figure 3-1b.

3.2 Fabrication Methods

3.2.1 Nanosphere lithography

Nanosphere lithography is a benchtop lithography technique used to fabricate large arrays of plasmonically active nanomaterials on common substrates such as glass cover slips and silicon substrates.[4, 5] The glass coverslips that are used for NSL must first be chemically cleaned, which is done through a three-step procedure. First, the glass substrates are sonicated in acetone. Then the glass substrates are sonicated in a solution of sulfuric acid and NoChromix®. Finally, the subjected to a 1:1:5 (v:v:v) solution of hydrogen peroxide:ammonium hydroxide:water. After each step, the glass coverslips are thoroughly rinsed with Milli-Q® (18.2 MΩ/cm^3) water. Once clean, the glass coverslips are dried with a gentle flow of N_2 gas and are ready for NSL.

A solution of dispersed polystyrene (PS) spheres is prepared by diluting a stock sample of PS spheres in water (10 % w/w) and Milli-Q® water with a ratio of 1:25 (v:v). A rubber O-ring is placed on the glass substrate, into which 25 μL of the PS spheres solution is drop-casted. The substrate is covered to dry for 24 hours. Once dried, the substrate is covered by large areas of monolayer PS beads on the surface.

Metal deposition by electron-beam evaporation (Angstrom Engineering) in Western's Nanofabrication Facility. During this process, the metal pellets located in the crucibles evaporated using a focussed high current beam under vacuum. The amount of metal deposited onto the substrate is controlled by the evaporation rate and a quartz microbalance. On dielectric substrates, such as glass, a thin film (3 to 5 nm) of titanium is added before the coinage metal, allow it to adhere to the surface substrate more efficiently. This thin film of titanium does not affect the spectral position of the LSPR.[1] This produces a homogeneous film over nanosphere (FON) substrate. After the metal deposition, the PS beads are removed by gently sonicating the substrate in an anhydrous ethanol solution, producing hexagonal arrays of nanoprisms (i.e. Fisher patterns) on the substrate surface where the monolayers were located (Figure 3-1).

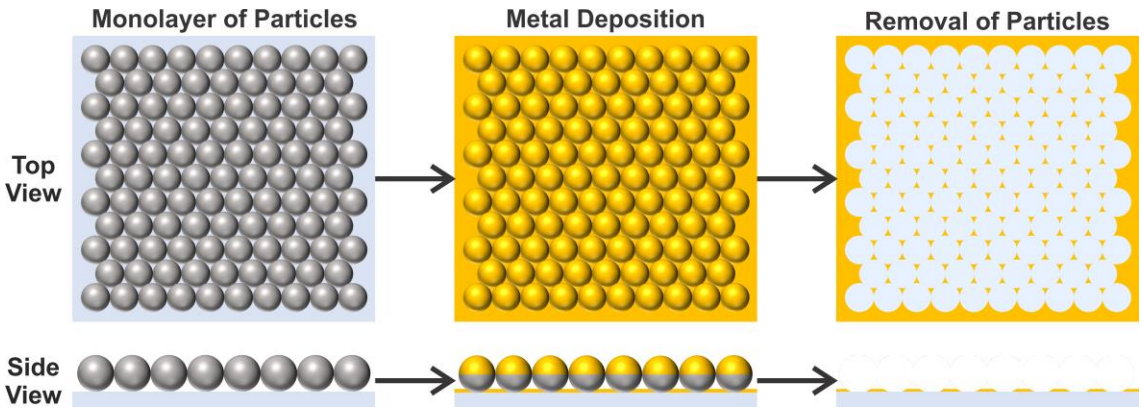

Figure 3-2. An illustration of the three main steps of NSL: monolayer formation of PS beads, metal deposition over the monolayer producing the FONs, and the Fisher pattern produced after the removal of the PS beads.

The diameter of the PS beads used, as well as the thickness of the metals deposited, will determine the sizes of the nanoprisms in the resulting Fisher pattern.[6] The subsequent LSPR wavelength ultimately depends on the size of the nanoprisms. The work done by Haynes and Van Duyne highlights the dependence of the LSPR spectral position based on multiple factors, including shape, metal thickness, and size (Figure 3-2).[6] When decreasing the particle size but maintaining a comparable metal thickness, the LSPR peak will exhibit a spectral shift towards smaller wavelengths (blue shift). The ability to control the LSPR position renders NSL a powerful and cost-effective technique for the effective production of large (~ a few mm^2 to cm^2) areas of plasmonic nanomaterials.

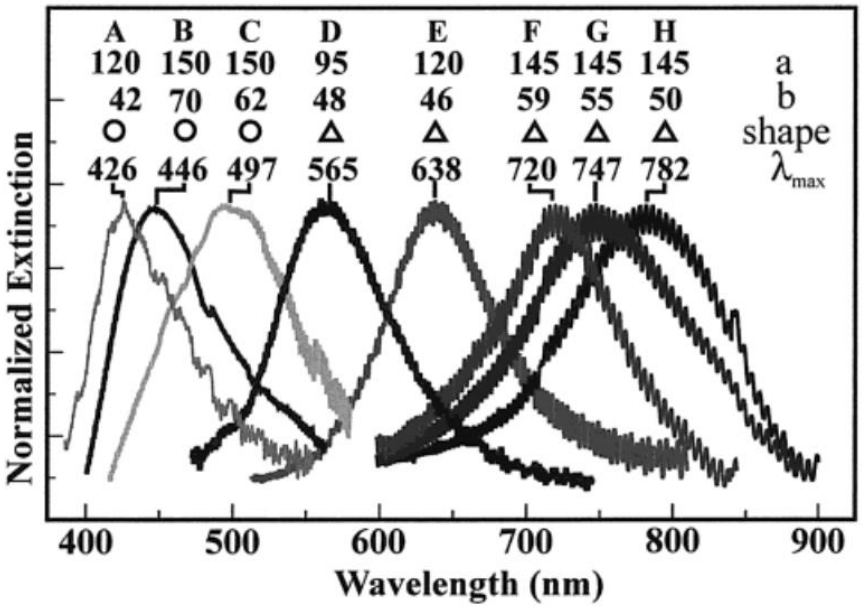

Figure 3-3 UV-visible extinction spectra of Ag single layer periodic particle arrays of (a-c) nanodisks and (d-h) nanoprisms on mica substrates. From top to bottom, the parameters indicated on the right represent tnanosphere diameter used in the masks, thickness of deposited metal, shape of nanostructure, and LSPR peak position. The reported spectra are raw, unfiltered data. The oscillatory signal superimposed on the LSPR spectrum seen in the data is due to interference of the probe beam between the front and back faces of the mica. Reprinted (adapted) with permission from Haynes, C. L.; Van Duyne, R. P., J. Phys. Chem. B 2001, 105, 5599-5611. Copyright 2001 American Chemical Society.

3.2.2 Electron-Beam Lithography

While NSL is effective at producing large areas of plasmonic nanomaterials, the complexity of the structures is limited to triangular shapes and generating these structures becomes increasingly difficult as the PS sphere size is reduced. Therefore, advanced lithographic techniques are necessary to produce more complex nano- and metamaterials. Electron-beam lithography (EBL) offers a spatial resolution of 10 nm using conventional setups [7-9] and sub-5 nm spatial resolution using aberration-corrected setups thus producing nanostructures with exquisite spatial resolution.[10-12] Due to its low spatial resolution and the ability to fabricate virtually any desired shape, EBL is a powerful

technique for generating and tuning plasmonic materials for a wide variety of applications.[8, 13]

The EBL process contains six steps and one optional step:

- In step 1, a substrate is cleaned using an O_2 plasma cleaning process (Orion Reactive Ion Etching, Trion Technologies). The substrate can vary from glass cover slips for applications in the visible wavelength range, to CaF_2 windows for applications in the near- to mid-infrared wavelength range, to silicon surfaces for initial dose testing and imaging samples.

- In step 2, a photoresist is spin coated onto the surface of the clean slide. The photoresist, which can be either positive or negative, is chosen based on the desired structures. After development, a positive photoresist yields holes in the exposed areas, generating a positive mask that will result in the desired structure. Contrarily, a negative photoresist will yield pillars in the exposed areas, generating a negative mask that will leave a flat metallic surface with holes in the substrates surface in the areas exposed to the electron beam. For this thesis, a positive photoresist PMMA-A2 was chosen. PMMA-A2 consists of a 2% w:v solution of polymethyl methacrylate (PMMA, MW = 950 kDa) in anisole. The photoresist thickness is also an important factor. When the photoresist is spin coated onto the surface, the photoresist concentration, the spin speed, and spin time determine the thickness of the photoresist layer.[14] For example, PMMA-A2 will produce a 90 nm polymer layer and is best suited for nanostructures with a desired height of 45 nm or less. When increasing the thickness of the photoresist layer, thicker nanomaterials can be produced, but spatial resolution will be lost in the process.

- Step 3 is optional and only used for dielectric substrates (e.g., glass and CaF_2). For these materials, a conductive layer must be deposited to avoid charging at the surface of the sample upon irradiation with the electron beam. The conductive layer used in this thesis is AquaSAVE^{TM} (Mitsubishi Chemical Corporation). This polymer is conductive that can be spin coated on top of the photoresist and serves to prevent any electrostatic charging at the photoresists surface, which would result in the

photoresist being over exposed. Over exposure would result in the polymer around the written pattern to be exposed as well, resulting in a loss of spatial resolution and even burnt material at the substrate surface.[15]

- In the irradiation step (step 4), the substrate is exposed to the electron beam to produce the desired mask. The instrument used in this thesis was the Leo Zeiss 1530 SEM equipped with a piezo nanopositioning stage combined with a Raith Nanofabrication EBL control system (Elphy QUANTUM, Raith Nanofabrication). A 10 μm aperture (resulting an approximate beam spot size of 12 nm) with a beam voltage of 30 kV was used for most of the metamaterials produced. A 20 μm aperture (resulting in an approximate beam spot size of 20 nm) can be used to produce large surface areas of nanomaterials in the same time frame and is generally more useful in the production of less complex nanomaterials. The PMMA-A2 positive photoresist was exposed with a dose of 1000 pC/cm. During exposure, the PMMA polymer chains are broken into monomer units, allowing them easily dissolve with a developer and be removed while the bulk of the unexposed photoresist remains.[16]

- The final steps of the EBL process are development (step 5), metal deposition (step 6), and final lift-off of the residual photoresist (step 7). The development is done in a 1:3 (v:v) solution of methyl isobutyl ketone:isopropanol. Then, the developed substrates are rinsed in an isopropanol bath and gently dried with N_2 gas. The metal deposition step is identical to the metal deposition described in Section 3.2.1 of this chapter. Finally, lift-off is done in Remover PG (Kayaku Advanced Materials), an n-methyl-2-pyrrolidone based solution designed to efficiently remove photoresist after lithographic fabrication.

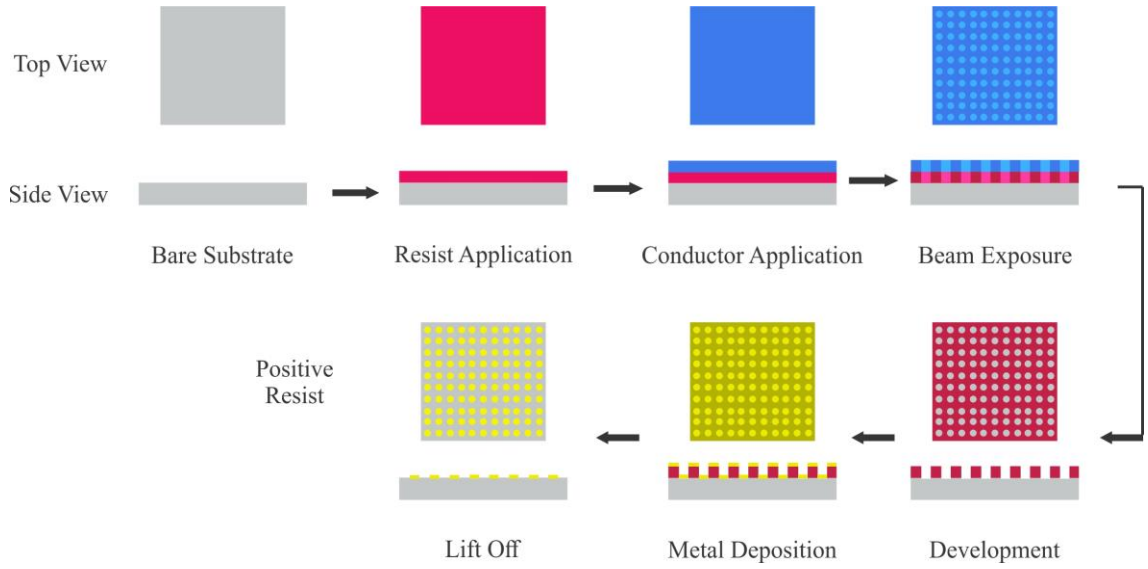

Figure 3-4 Illustration of the stages of EBL process using a positive photoresist. The bare substrate, resist application, conductor application, beam exposure, development, metal deposition, and lift off represent the described steps 1 through 7, respectively.

EBL has become widely used for nanofabrication due to its versatility and precision.[17, 18] Shown in Figure 3-4 are structures that have been made by EBL. These structures were carefully conceived with preliminary modelling to display resonances in specific spectral ranges. Figures 3-4a,b are fractal structures with plasmon resonances in the visible range.[19] Figures 3-4c is a crosshair structure with resonances in the visible range that were exploited for plasmon-mediated chemistry.[2] Figure 3-4d is a series og gold nanorods used for surface-enhanced infrared absorption, and Figures 3-4e,f are chiral structures developed to have circular dichroic response in the infrared spectral range.[18, 20, 21]

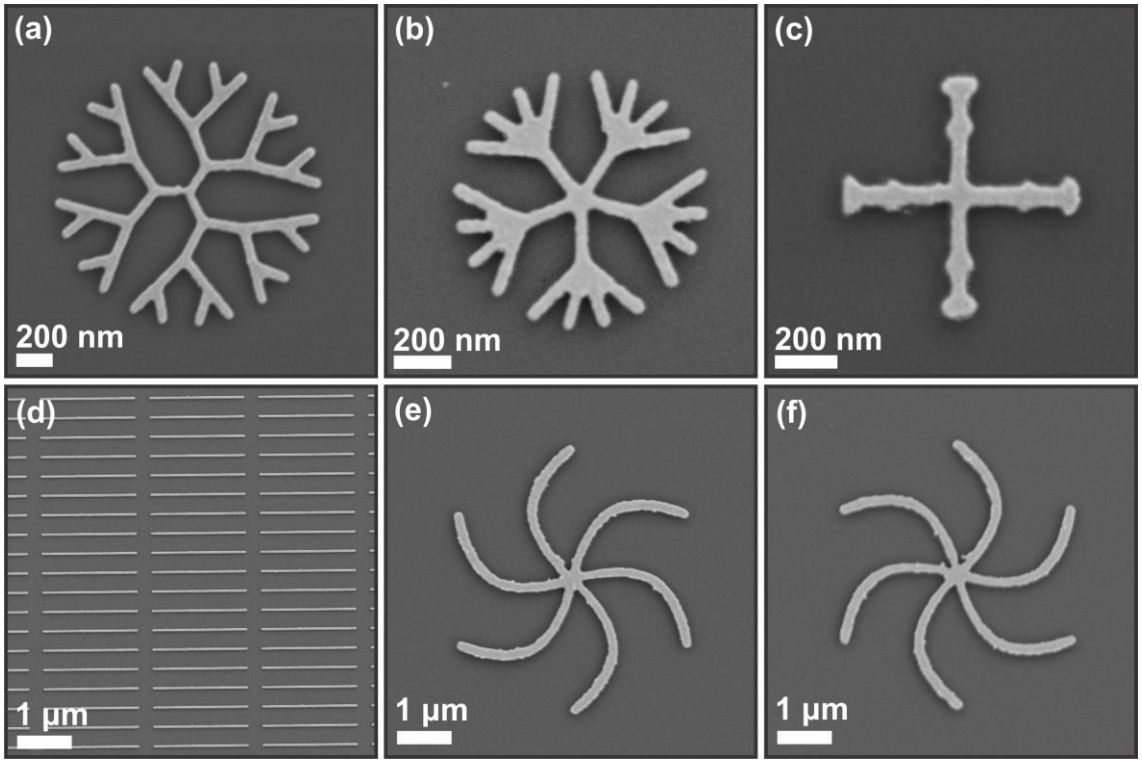

Figure 3-5 SEM images of structures produced by EBL. (a) A three-branched generation four dendrimer; (b) a five-branched generation two dendrimer; (c) a four-branched crosshair structure; (d) an array of nanorods; (e) a right-handed spiral structure; (f) a left-handed spiral structure.

3.2.3 Chemical Vapour Deposition

The transition metal dichalcogenides (TMD) flakes studied in Chapter 5 were prepared using chemical vapour deposition (CVD). A high temperature furnace (Lindberg Blue, Thermo Scientific) equipped with a 2.54 cm diameter fused quartz tube was used for the CVD process. For MoS_2 flake production, 160 mg of sulfur powder (Sigma Aldrich) is placed in an alumina boat (Sigma Aldrich) 23 cm upstream from the MoO_3 located at the center of the furnace in the lower temperature zone, achieving a temperature between 150 and 200°C (*i.e.* above the melting point/below the boiling point of the sulfur powder). This is done to control vaporization rate of the sulfur powder transported by the Ar gas, enabling the reaction to occur without a surplus of the sulfur powder at the surface of the substrates and without boiling off the sulfur powder before the reaction can occur. As it vaporizes, the sulfur is transported towards the center of the furnace by the argon gas

where it encounters the vaporized MoO_3 powder. 8 mg of MoO_3 powder (Sigma Aldrich) is placed in a second alumina boat. On top of the second alumina boat, an SiO_2@Si substrate, prepared by depositing 300 nm of SiO_2 on Si by plasma CVD, is secured by stainless steel wire. The alumina boat containing the MoO_3 and the substrate is then placed in the center of the glass tube in the high temperature zone of 850°C (*i.e.* above the melting point of MoO_3 powder). The system is placed under a constant flow of Ar gas at a rate of 100 sccm. Once the reagents are placed inside the quartz tube, the furnace is gradually heated from room temperature to 550°C at a rate of 18°C/minute, then from 550°C to 850°C at a rate of 5°C/minute. The furnace is kept at 850°C for 15 minutes before being cooled down to room temperature under ambient conditions. This recipe provides substrates with areas of monolayer 2H phase MoS_2 flakes (Figure 3-5b) near the edges of the substrate as indicated by the red ovals in Figure 3-5a.

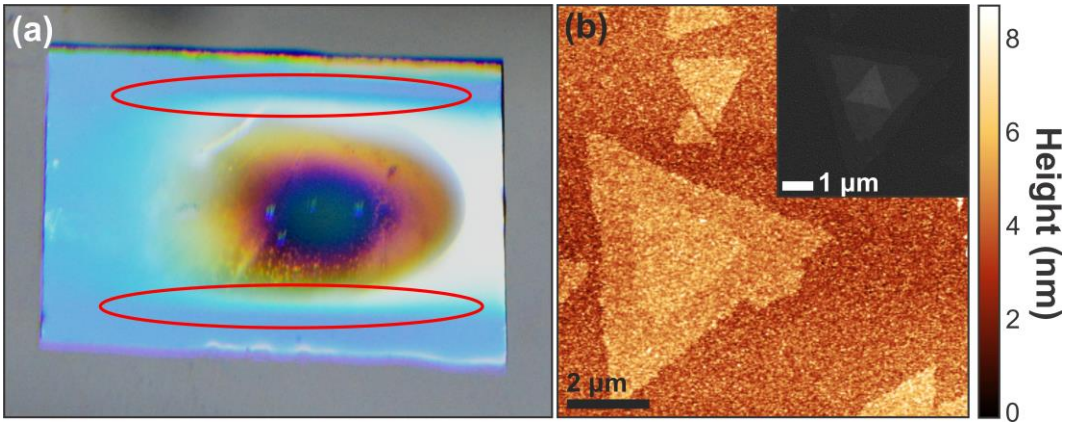

Figure 3-6 (a) An SiO_2@Si substrate after the CVD process with the regions of interest indicated by the red ovals. (b) An AFM image of a bilayer MoS_2 flake with an SEM image of a trilayer inset.

3.3 Characterization Methods

3.3.1 Scanning Electron Microscopy

The scanning electron microscopy (SEM) images presented in this thesis were taken with the Leo Zeiss 1530 field emission SEM at Western's Nanofabrication facility. This is the same instrument used for the EBL process. The imaging was done in secondary scattered electron mode with a beam current typically between 1 and 3 kV.

3.3.2 Visible-Near Infrared Absorbance Spectroscopy

The visible-near-infrared (vis-NIR) absorbance measurements in this thesis were obtained using an in-house built inverted microscope (figure 3-6). This microscope uses a halogen lamp (HL-200, Ocean Optics) light source covering a spectral range of 350 nm to 1050 nm. The light is passed through a 100 μm wide fiber optic cable and expanded using a 10×/N.A. = 0.25 microscope objective (M-10×, Newport). The light is then recollimated using a 40×/N.A. = 0.65 objective (M-40×, Newport), resulting in a beam diameter of 50 μm. The sample stage is attached to the inverted Nikon microscope. The light passing through the sample is then collected using a 20×/N.A. = 0.5 objective (M-20×, Newport) before passing to either the binoculars, or a spectrometer through a second 100 μm wide fibre optic cable. The light is collected by a spectrometer (USB4000-VIS-NIR-ES, Ocean Optics) and is then analyzed by OceanVIEW software (Ocean Optics). This setup allows for the analysis of a 50 μm diameter circular area on substrates. The I_0 for the samples was measured by acquiring the spectrum through bare glass located with 1 mm of the sample. The background was taken under the same conditions as the I_0, but with the halogen lamp turned off which assisted in the mitigation of background noise contribution. The resulting measurements produced the experimental absorption ($\log(I/I_0)$).

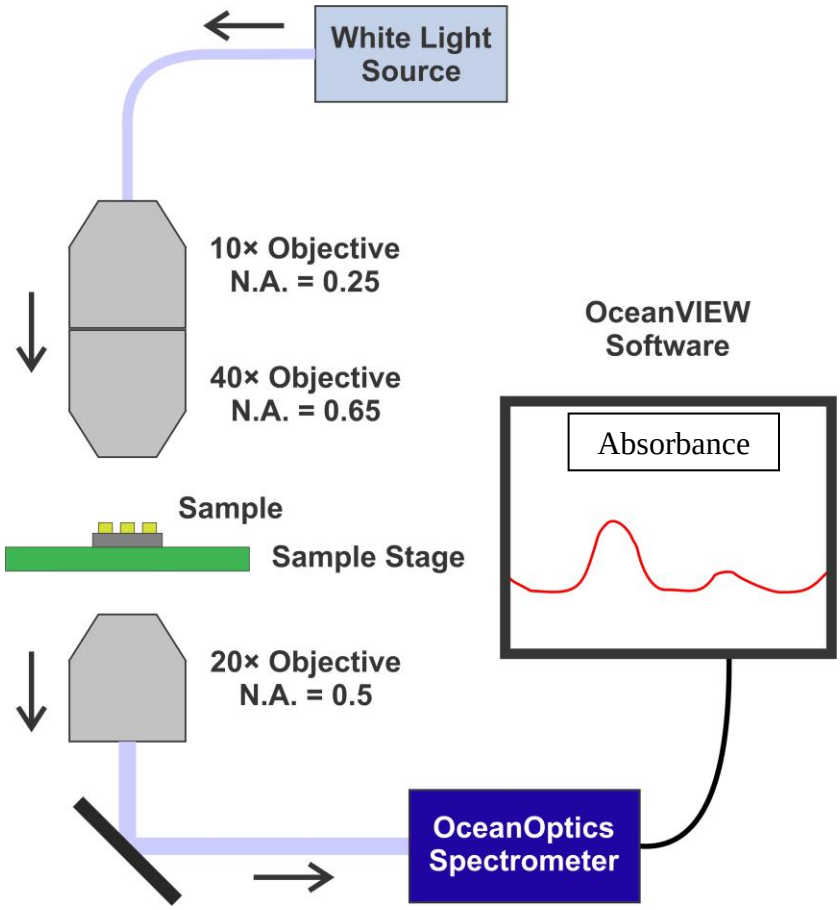

Figure 3-7 Schematic of the microscope setup used for the vis-NIR absorbance measurements.

3.4 SHG Microscopy

The SHGM experiments were performed using an in-house built microscope setup (figure 3-7).[22, 23] The wavelength of the titanium-sapphire laser in this setup is tunable between 700 and 980 nm (Coherent Mira 900f). The laser was tuned to 800 nm (*i.e.* the fundamental frequency) with a power up to 1.1 W. This laser has a pulse width of ~200 fs and a repetition rate of 76 MHz. The polarization and power are controlled using a manually controlled half-wave plate (Newport, 05RP02-46) and a horizontal polarizer (Newport, 10GL08AG.16) to produce p-polarized light, followed by an electronically controlled half-wave plate on a motorized optical mount (Thorlabs, WPH05M808 and PRM1Z8E), which controls the final polarization of the light. A silver mirror on a flip mount is used after the polarization and power control to check the output power. The

light is then reflected by a dichroic mirror (Chroma, T680spxr), which has a 99.96% reflection at 800 nm and 2.38% reflection at 400 nm, into a 100×/N.A. = 0.95 air objective (Olympus, MPLFLN 100x), and onto the sample surface. A nanopositioning stage scans the laser across the sample surface (PI nano® XY Piezo Stage). The reflected light at the fundamental frequency from the structures, as well as the two-photon photoluminescence, from the structures was significantly reduced using filters. First, a glass short-pass filter (Thorlabs, FGB39) eliminates the fundamental light at 800 nm and transmits the generated light at 400 nm (71.9% transmission). This is immediately followed by a band-pass filter (AHF, F49-406) that provides a 93.34% transmission of light between 385 and 425 nm and 0.0001% transmission outside of that range. Additionally, the SHG emissions were split into their orthogonal polarizations using a polarized beam splitter cube (Thorlabs, PBS251) that transmits 86.2% p-polarized and 0.11% s-polarized light. Finally, the light is collected by two separate avalanche photodiodes (Perkin Elmer, SPCM-AQR-15) and are equipped with a single-photon counting module (SPCM). The SHG response is analyzed using a LabView-based software developed by Dr. Renjie Hou, a previous Ph.D. candidate of the Lagugné group. The SHGM is typically carried out at an irradiance of 1.27×10^{6} W/cm^{2} at the sample.

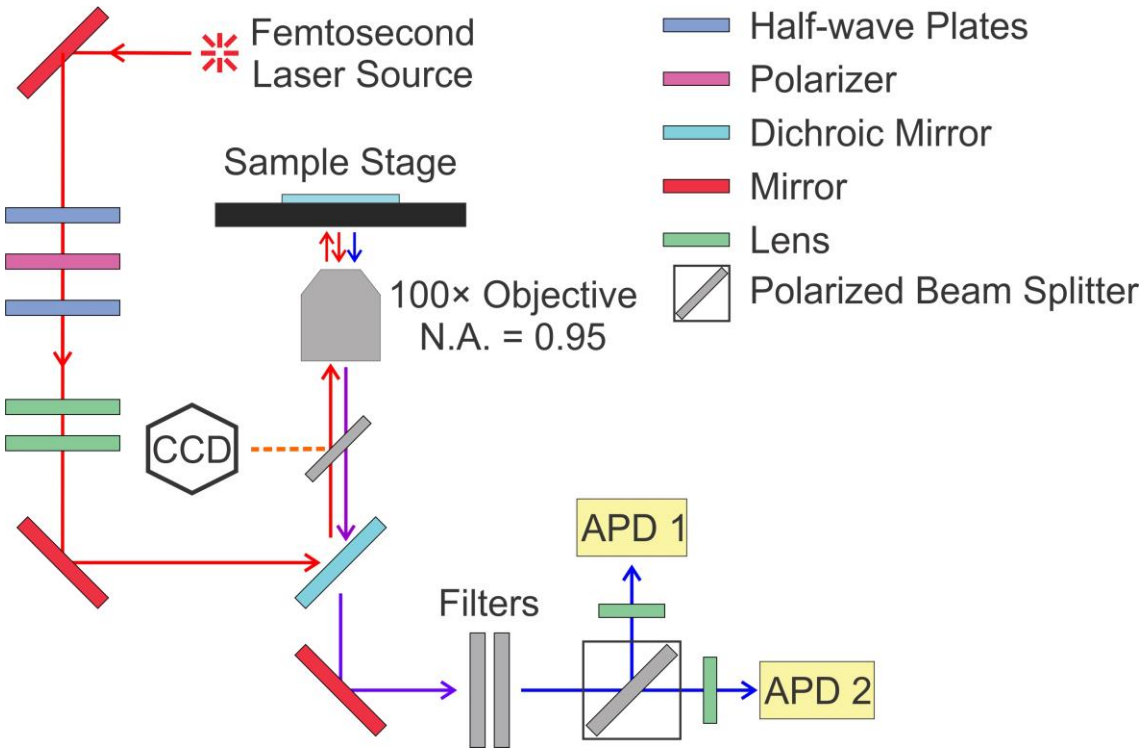

Figure 3-8 Schematic of the SHG microscopy setup.

3.5 Metamaterial Characterization

The metamaterials produced by either NSL or EBL are characterized prior to experiments to determine and tune their LSPRs. Two approaches are used to evaluate the optical properties of the metamaterials: FDTD modelling, to determine the theoretical LSPR positions prior to fabrication, and vis-NIR spectroscopy, to experimentally determine the actual LSPR positions after fabrication. The correlation of these approaches confirms the physical properties of the structures and the anticipated optical properties. When the two approaches do not match, the calculations are repeated with further optimizations, and, when necessary, new samples are fabricated.

3.5.1 Characterizing LSPRs in Metamaterials

Fractal metastructures are of interest because the display several plasmon resonances over a broad spectral range.[1, 24] These resonances can be tuned from the visible to the mid-infrared range by altering parameters such as the dimensions of the structural units,

their organization and the metal thickness used.[1] Figure 3-8 shows examples of such structures with distinct symmetries for the first and second generations of fractals.

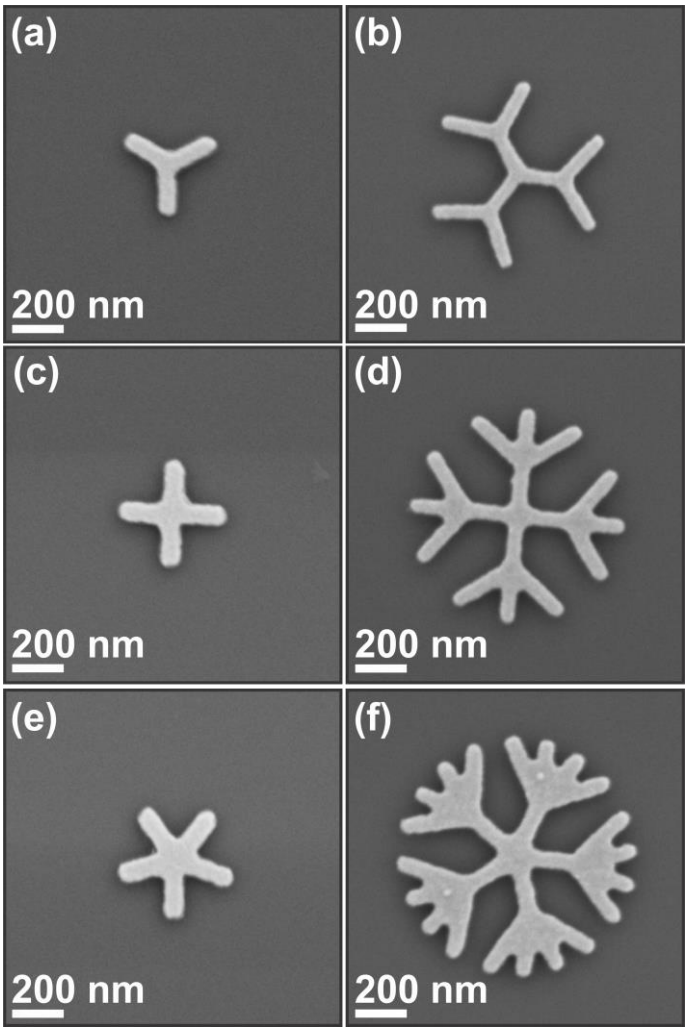

Figure 3-9 Dendrimers fabricated by EBL. (a-b) Three-branched first and second generations, respectively; (c-d) four-branched first and second generations, respectively; (e-f) five-branched first and second generations, respectively.

Previous published studies by Dr. Gregory Wallace from the Lagugné group have shown that these structures can be tuned in the infrared range and could be used for surface enhanced infrared spectroscopy.[25] The EM modelling and experimental measurements matched very well.[24] The optical properties of the modelled structures were set using the standard Palik indices of refraction for the Ti (adhesion layer) and Au material parameters deposited on a SiO_2 (glass) substrate.[26] For the nonlinear optical calculations,

the nonlinear susceptibility of Au, $\chi^{(2)}$, was set to 3×10^{-20} m/V.[27] The absorbance spectra were calculated using six scattered light monitors in a three-dimensional arrangement, a feature designed by Lumerical that allows the analysis of a material's absorbance, extinction, and scattering. A two-dimensional array of structures was set up using a y-symmetry conditions with an average of 800 nm between individual structures in both the x- and y-axis set using periodic boundary conditions and a perfectly matched layer along the z-axis. The amplitude of the input planar wave field was set to 1×10^{9} V/m for the linear simulations, and an input light source of 800 nm with 150 fs pulses was used to calculate the nonlinear enhancement at both 800 nm and 400 nm. The nonlinear calculations were done at these wavelengths to match the SHG microscope setup outlined in Section 3.3.

The simulated absorbance spectra are useful to evaluate the spectral position of the LSPRs prior to the costly nanofabrication process. Shown in figure 3-9 are calculated spectra (red) superimposed with experimental ones (blue) for a series of 4- and 5-branched fractal structures.[19] While the simulations and the experimental data are close, the simulations cannot compensate for structural defects produced during fabrication. Rounded edges and surface roughness are surface defects that are generally not considered in the modelling parameters and lead to differences between the experimental and calculated resonances.

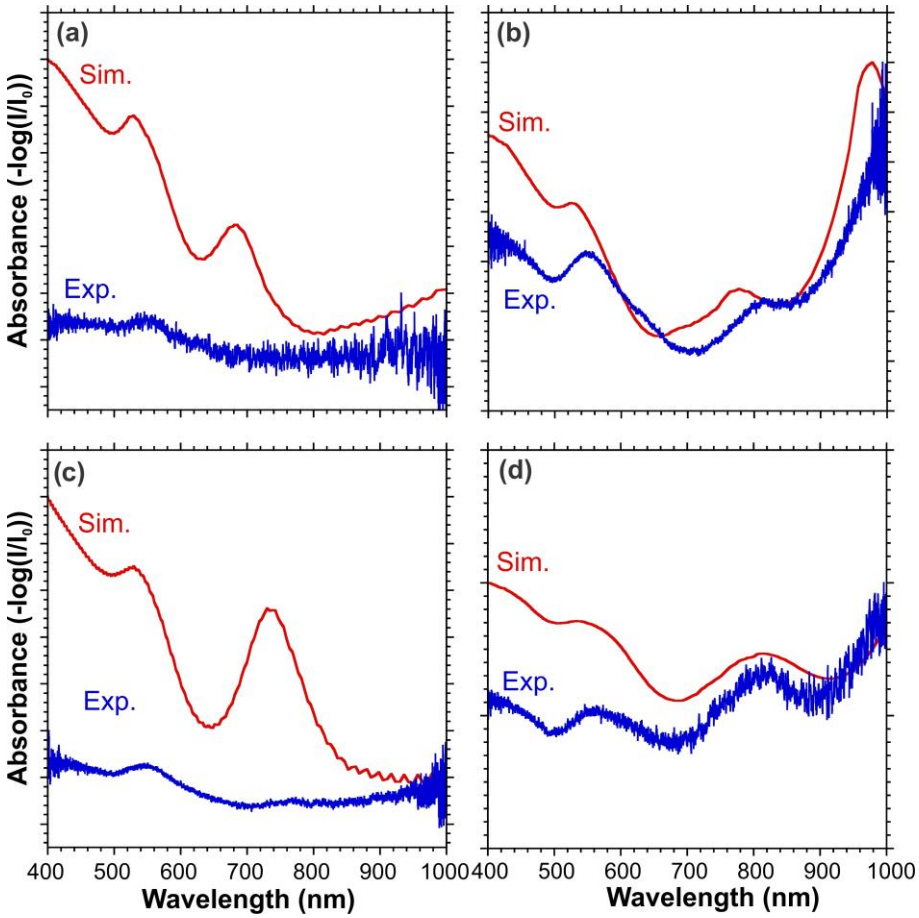

Figure 3-10 Simulated (red) and experimental (blue) absorbance spectra for (a) a four-branched generation one dendrimer, (b) a four-branched generation two dendrimer, (c) a five-branched generation one dendrimer, and (d) a five-branched generation two dendrimer.

3.5.2 Tuning LSPRs in Metamaterials

Parameters that can be varied when tuning the LSPR of the dendrimers include: the generation of the dendrimer (Figure 3-9), the length and width of the individual nanorods within the dendrimers (Figure 3-10a red line for length and blue line for width), the type of metal deposited,[28] and finally the thickness of metal deposited. Additionally, these dendrimers are fabricated in arrays of 50×50 μm^2, where each array contains upwards of 900 individual structures (Figure 3-10b). Consequently, the experimental absorbance results from an average of 900 structures.

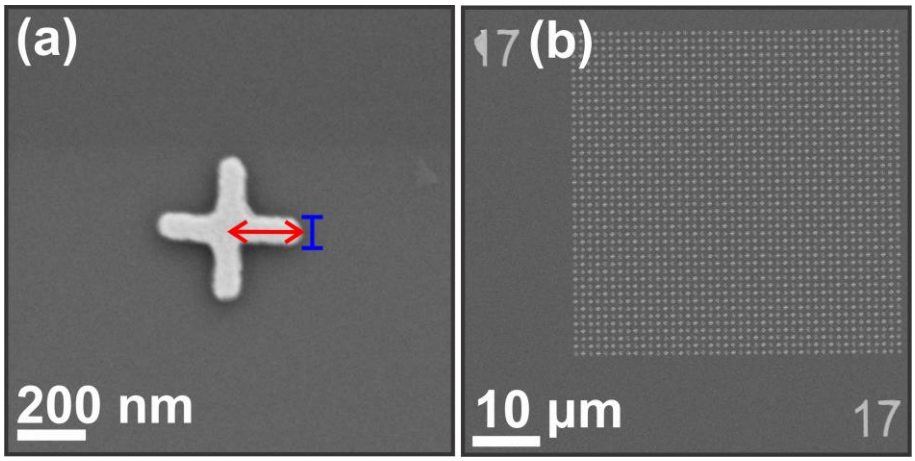

Figure 3-11 (a) an SEM image of a four-branched generation one dendrimer. The red arrows indicate the length varied and the blue lines represent the width varied. (b) an SEM image of an array of dendrimers, with an identifying number shown.

With the dendritic structures, an effective method to tune the LSPRs consists of inscribing higher generations with the same symmetry (figure 3-11). This involves adding a selected number of nanorods to the extremities of the existing structure. For example, if a four-branched generation one dendrimer were to be modified to a second generation, three branches would be added to each extremity (figure 3-11b inset), yielding a total of 4 branches for the outer dendrons. The branches are added at an angle to avoid overlapping with the branches of the adjacent dendrons. Second-generation dendrimers are a simple modification that introduces new exploitable LSPRs in the visible range. Dendrimers up to the fourth generation were prepared highlighting resonances in the visible range, which are discussed in Chapter 4.

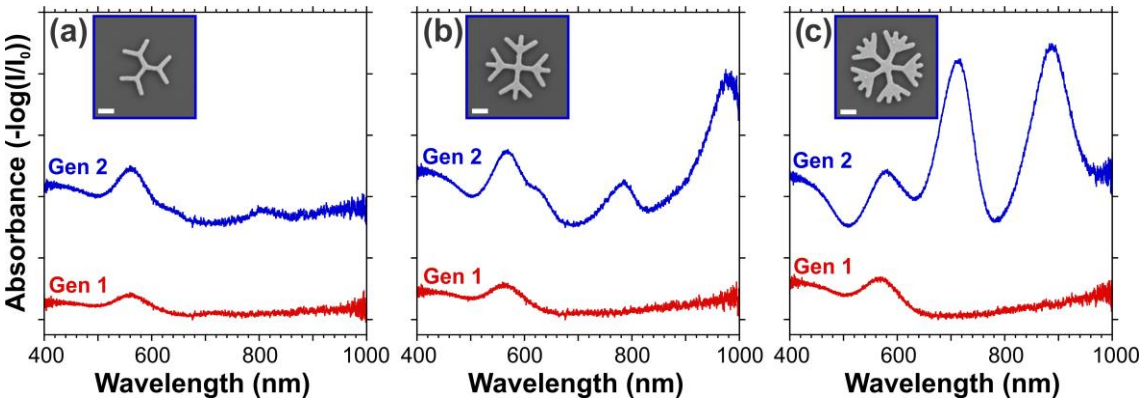

Figure 3-12 Absorbance spectra showing the difference between generation one (Gen 1 - red) and two (Gen 2 - blue) dendrimers with (a) three branches, (b) four branches, and (c) five branches. The inset shows generation two of these dendrimers and the scale bar is 200 nm.

By increasing the branch length (figure 3-11a, red arrow), a red shift in some of the resonance positions is measured. For a specified deposited metal thickness (i.e. the height of the structures), the ratio between the branch length and the width can also be varied to modify selected resonance positions. By increasing the length-to-width ratio, some LSPRs will be red shifted. For example, the longitudinal quadrupolar and dipolar modes of the four- and five-branched generation two dendrimers, respectively, increases linearly from around 700 to 900 nm as the length of the individual nanorods increases from 150 to 250 nm (figure 3-12b-d).[1] However, the transverse dipolar mode observed around 570 nm for the three-, four-, and five-branched generation two dendrimers remains unshifted. Increasing the length-to-width ratio allows the possibility of controlling the wavelength at which the LSPRs are excited, and therefore the fine tuning of the structures for specific applications.

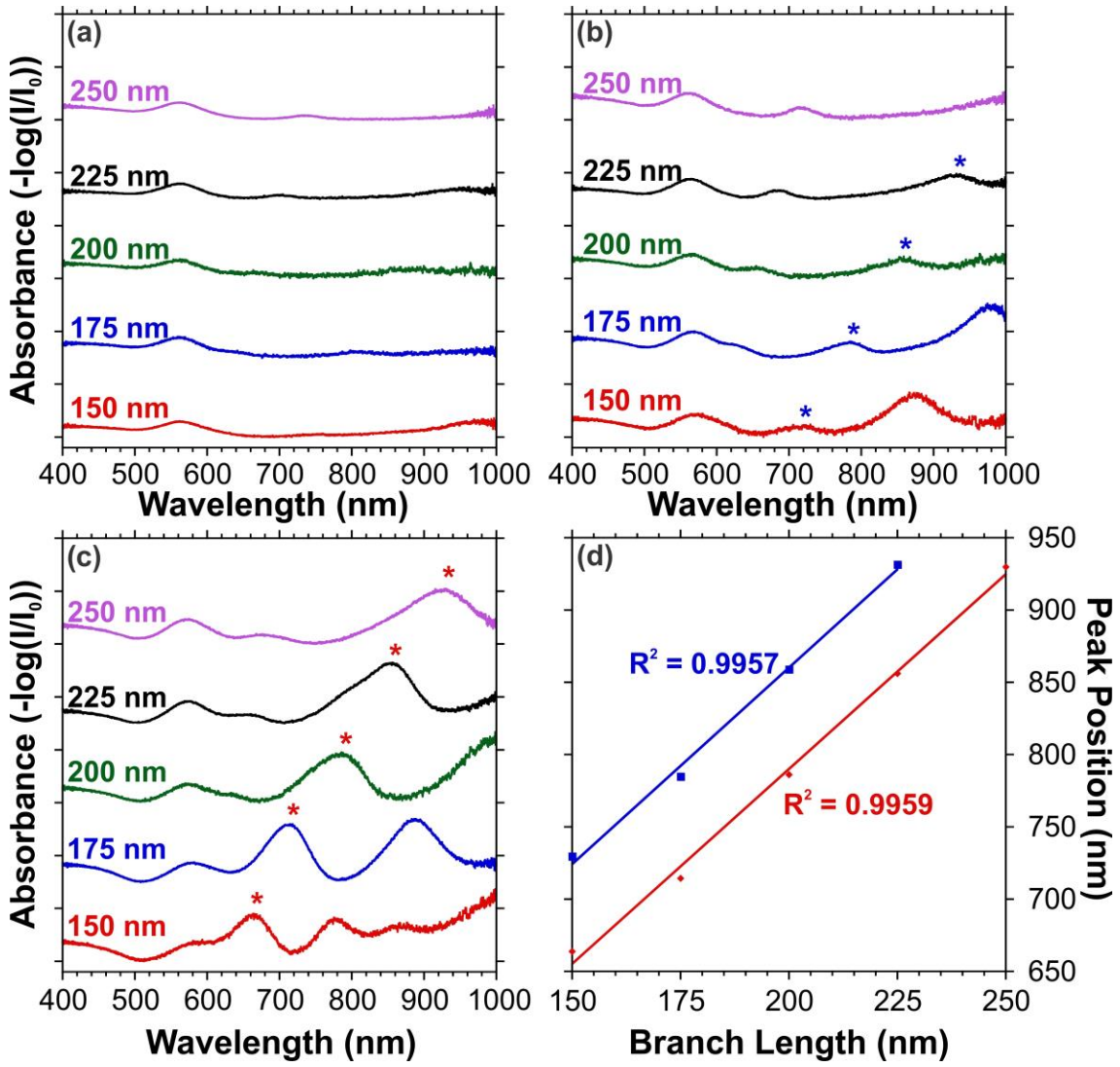

Figure 3-13 Absorbance spectra of (a) three-, (b) four-, and (c) five-branched generation two dendrimers of varying sizes (as indicated above each individual spectrum). The peak positions of interest are highlighted with asterisks in (b) and (c) as a guide to the eye. (d) Linear increase in the peak position with respect to the branch length, where the blue line and square markers correspond to the blue asterisks in (b) and the red line and square markers correspond to the red asterisks in (c).

The spectral position of the aforementioned transverse dipolar mode can be shifted by increasing the width of the dendrimer branches as opposed to the length. The increase in width will cause a red shift the transverse dipolar LSPR mode associated to the width of

the structure as indicated by the dashed lines in figure 3-13. Consequently, a blue shift in the LSPR modes is caused by the decreasing length-to-width ratio (figure 3-13b,c).

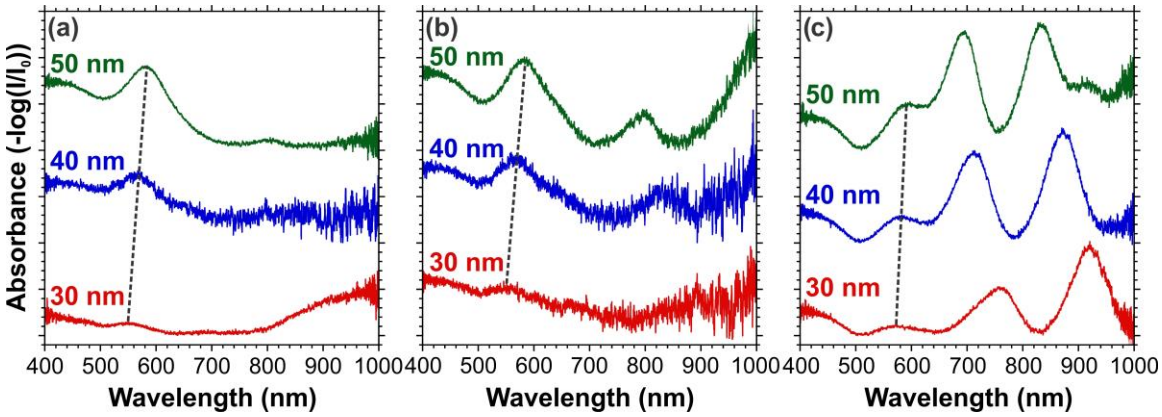

Figure 3-14 Absorbance spectra of (a) three-, (b) four-, and (c) five-branched generation two dendrimers of varying widths as indicated above each individual spectrum. The peak position of interest is indicated by the dashed line as a guide to the eye.

3.6 Surface Functionalization

The functionalization of the structures performed in Chapters 6 and 7 of this thesis follow similar protocols. These experiments were done with an O-ring laid on the surface of the substrates into which the solutions of diazonium salt were drop-casted. The O-ring was added to ensure the solvent would not evaporate throughout the experiments, which would cause the diazonium salt to recrystallize on the surface.

3.6.1 Single-Beam Grafting

Prior to the single beam grafting structures on the bare glass substrates presented in Chapter 6, the substrates were cleaned using the method described in Section 3.2.1. The substrates were positioned over an inverted microscope equipped with a 632.8 nm laser. A 5 mM solution of 4-nitrobenzenediazonium tetrafluoroborate (MM = 236.92 g/mol, Sigma Aldrich) was prepared by dissolving 29.615 mg of the powder in 25 mL of Milli-Q® water and drop-cast into the O-ring on the surface of the substrates. Irradiation was performed through a 20× objective (N.A. = 0.5) with an irradiance of 1.17×10^4 W/cm^2

for a varying length of time. The sample stage was lowered slightly past the focal point to generate a wider beam spot. After irradiation, the samples were thoroughly washed with Milli-Q® water and dried under a gentle flow of N_2 gas.

The plasmon-mediated grafting procedure follows similar steps as the single-beam grafting with the same diazonium salt solution concentration. In Chapter 6, plasmon-mediated grafting was induced on the NSL substrate with the same 632.8 nm excitation source used in the single-beam grafting.

In Chapter 7, two different setups were used. The first setup used is described in Section 3.3, which was used to excite the LSPR of the metamaterial at 800 nm. The second setup followed the same procedure outlined in Section 3.5.1, but with a 532 nm laser in addition to the 632.8 nm laser, allowing for the excitation of two distinct LSPR modes using a single system. The average irradiance used throughout the experiments are as follows: 1.79×10^3 W/cm^2 for the 532 nm laser, 1.17×10^4 W/cm^2 for the 632.8 nm laser, and 1.27×10^6 W/cm^2 for the 800 nm laser.

3.7 Summary

In this chapter, we have described the different approaches and techniques used to characterize the metamaterials with optical properties that were adjusted for specific applications. These techniques were used in the design and fabrication of all the structures used in this thesis. The proper characterization of these materials is pivotal to accurately identify and tune the LSPRs of the metamaterials. The use of electron-beam lithography allows the fabrication and study of large, reproducible arrays of metamaterials. For the crosshair structures, the specific details on the modelling, tuning and characterization of the structures in Chapter 7 will be provided therein.

3.8 References

1. Wallace, G. Q.; Lagugné-Labarthet, F., *Analyst* **2019,** *144*, 13-30.

2. Therien, D. A. B.; McRae, D. M.; Mangeney, C.; Félidj, N.; Lagugné-Labarthet, F., *Nanoscale Adv.* **2021,** *3*, 2501-2507.

3. Inwati, G. K.; Kumar, P.; Roos, W. D.; Swart, H. C.; Singh, M., *J. Alloys Compd.* **2020,** *823*, 153820.

4. Cossio, G.; Yu, E. T., *Nano Lett.* **2020,** *20*, 5090-5096.

5. Chan, G. H.; Zhao, J.; Hicks, E. M.; Schatz, G. C.; Van Duyne, R. P., *Nano Lett.* **2007,** *7*, 1947-1952.

6. Haynes, C. L.; Van Duyne, R. P., *J. Phys. Chem. B* **2001,** *105*, 5599-5611.

7. Kumar, R.; Chauhan, M.; Moinuddin, M. G.; Sharma, S. K.; Gonsalves, K. E., *ACS Appl. Mater. Interfaces* **2020,** *12*, 19616-19624.

8. Chen, Y., *Microelectron. Eng.* **2015,** *135*, 57-72.

9. Horák, M.; Bukvišová, K.; Švarc, V.; Jaskowiec, J.; Křápek, V.; Šikola, T., *Sci. Rep.* **2018,** *8*, 9640.

10. Hirota, K.; Hara, S.; Wada, H.; Shimojima, A.; Kuroda, K., *ACS Nano* **2019,** *13*, 2795-2803.

11. Manfrinato, V. R.; Stein, A.; Zhang, L.; Nam, C.-Y.; Yager, K. G.; Stach, E. A.; Black, C. T., *Nano Lett.* **2017,** *17*, 4562-4567.

12. Jiang, N., *Microelectron. Eng.* **2017,** *168*, 41-44.

13. Zeng, Y.; Madsen, S. J.; Yankovich, A. B.; Olsson, E.; Sinclair, R., *Nanoscale* **2020,** *12*, 23768-23779.

14. Semaltianos, N. G., *Microelectronics J.* **2007,** *38*, 754-761.

15. Duan, H.; Zhao, J.; Zhang, Y.; Xie, E.; Han, L., *Nanotechnology* **2009,** *20*, 135306.

16. Rahman, F.; Carbaugh, D. J.; Wright, J. T.; Rajan, P.; Pandya, S. G.; Kaya, S., *Microelectron. Eng.* **2020,** *224*, 111238.

17. Plank, H.; Winkler, R.; Schwalb, C. H.; Hütner, J.; Fowlkes, J. D.; Rack, P. D.; Utke, I.; Huth, M., *Micromachines* **2020,** *11*, 48.

18. Carbaugh, D. J.; Pandya, S. G.; Wright, J. T.; Kaya, S.; Rahman, F., *Nanotechnology* **2017,** *28*, 455301.

19. Therien, D. A. B.; Hou, R.; Lagugné-Labarthet, F., *Plasmonics* **2020,** *15*, 507-515.

20. Liu, Z.; Zhong, Y.; Shafei, I.; Jeong, S.; Wang, L.; Nguyen, H. T.; Sun, C.-J.; Li, T.; Chen, J.; Chen, L.; Losovyj, Y.; Gao, X.; Ma, W.; Ye, X., *Nano Lett.* **2020,** *20*, 2821-2828.

21. Brown, L. V.; Yang, X.; Zhao, K.; Zheng, B. Y.; Nordlander, P.; Halas, N. J., *Nano Lett.* **2015,** *15*, 1272-1280.

22. Hou, R.; Lagugné-Labarthet, F., *Surf. Sci.* **2018,** *676*, 46-50.

23. Hou, R., University of Western Ontario, https://ir.lib.uwo.ca/etd/3696 2016.

24. Wallace, G. Q.; Foy, H. C.; Rosendahl, S. M.; Lagugné-Labarthet, F., *J. Phys. Chem. C* **2017,** *121*, 9497-9507.

25. Wallace, G. Q.; McRae, D. M.; Lagugné-Labarthet, F., *Opt. Lett.* **2019,** *44*, 3865-3868.

26. Palik, E., *Handbook of Optical constants of Solids*. Academic Press: Burlington, 1997; p 3224.

27. Hou, R.; Shynkar, V.; Lafargue, C.; Kolkowski, R.; Zyss, J.; Lagugné-Labarthet, F., *Phys. Chem. Chem. Phys.* **2016,** *18*, 7956-7965.

28. Ando, R. F.; Tuniz, A.; Kobelke, J.; Schmidt, M. A., *Opt. Mater. Express* **2017,** *7*, 1486-1495.

Chapter 4

4 Second-Harmonic Generation from Dendritic Fractals

This chapter is a version of a manuscript published in Plasmonics (DOI: https://doi.org/10.1007/s11468-019-01080-y).

Nanostructured conductive surfaces have been exploited for a variety of applications in photonics and optical sensing due to the broad spectral tunability of the localized surface plasmon resonances and the subsequent electromagnetic field confinement in the vicinity of the structures. Herein, we report on the second-order nonlinear optical properties of dendritic fractal structures with specific geometries that were optimized to yield resonances at both the fundamental and the second harmonic wavelengths. Using a femtosecond excitation at 800 nm, second harmonic generation microscopy experiments were conducted on a series of gold fractal dendritic structures with and without center of inversion. The polarized second harmonic maps reveal the local character of the SHG emission and even structures with center of inversion shows SHG activity in the periphery of the core dendron where non-centrosymmetric features are forming the higher fractal generations. The experiments were correlated using finite-difference time-domain electromagnetic time modelling performed at both the fundamental and second harmonic wavelengths.

4.1 Introduction

The past decade has seen the emergence of applications utilizing conductive nanostructures in optical sensing of analytes, filtering of specific spectral domains, and in biomedical applications such as photothermal therapies.[1-5] The high tunability of metallic nanostructures fabrication using either in colloidal synthesis or advanced nanofabrication methods for 2D arrays enables a control of light-matter interaction that was not possible before.[6-10] Metastructures with specific resonances spanning from the UV to the ThZ range have been fabricated and used towards specific applications maximizing the resonance conditions between an impinging field and a given structure.[3, 10]

Of particular interest are structures used in conjunction with spectroscopy techniques to further enhance the sensitivity and the acquisition speed of measurements, such as surface plasmon resonance (SPR), surface enhanced Raman spectroscopy (SERS) or surface-enhanced infrared absorption (SEIRA).[11-13] Plethoric number of contributions in the field have been published highlighting the diversity of applications in sensing and biosensing utilizing large, localized enhancements from plasmonic structures for spectroscopy purposes.[3, 9, 10, 13-18]

Harmonic generation is another field that has been investigated, albeit still a developing field. The idea here is to conceive metallic structures that are optimized to emit light at the 2nd or 3rd harmonic frequency as compared to the input light. For the specific case of second-harmonic, the symmetry of the structure is of critical importance since, in the dipolar approximation, SHG materials must have no center of inversion to yield generation of light at the second harmonic.[6, 11, 19] Yet the ability to conceive single nanostructures, isolated or organized as arrays, that emits specifically light at a harmonic frequency is of interest for the conception of multimodal platforms (a given structure that can yield distinct optical processes), transduction of an input excitation, super resolution microscopy with extreme localization of the SHG emission or to develop nanoscale visible light emitters that can be pumped using near-infrared sources.[20-22]

SHG is a two-photon process that depends on the inherent geometry of a material and its ability to interact with an electromagnetic (EM) stimulus. In general, both surface and bulk SHG must be considered and bulk materials without a center of inversion yield SHG with much higher intensity than its surface counterpart but requires phase matching conditions.

In metals commonly used for plasmonic applications (aluminum, silver, and gold being the most common ones) the atomic lattice is centrosymmetric; thus, no bulk second harmonic generation can be generated. However, the shape of these structures can be finely designed to show no inversion center, a condition for SHG activity.[12, 23] Unlike bulk materials, the SHG of such metallic non-centrosymmetric nanostructures does not come from phase matching conditions due to the small dimensions of these structures

with respect to excitation and second-harmonic wavelength. In nanostructures, the SHG signal rather originates from the surface of the structure and is amplified by the presence of "hot-spot" sites where the electromagnetic field is largely enhanced. Since the intensity of SHG varies quadratically with the excitation, a small increase of the local field is enough to induce a large enhancement of the SHG at the surface.

In this work, SHG measurements involving metamaterials with self-replicating features known and referred to as dendritic fractals are investigated. These fractal structures have demonstrated high tunability in the visible, near-infrared and mid-infrared range [24, 25] but have not been exploited for their nonlinear optical activity. A series of gold dendritic structures organized in arrays has been fabricated in order to show resonances at both the fundamental (λ=800 nm) and the second-harmonic (λ=400 nm) wavelengths and were mapped using an SHG microscope equipped with a femtosecond excitation source. The symmetry of the individual structures was changed from C_3 to C_5 symmetry and the number of generations was varied to evaluate how the fractal generation was altering the SHG signal over the surface of the structures. Further electromagnetic modelling was conducted using the finite-difference time-domain (FDTD) to evaluate both the absorption spectra and the EM enhancement maps of the field at both the fundamental and second-harmonic frequencies.

4.2 Methods

The following methods were used throughout this chapter:

- FDTD Simulations, as described in Chapter 3, section 3.1
- Electron-beam lithography (EBL), as described in Chapter 3, section 3.2.2
- Visible to near-infrared absorption microscopy, as described in Chapter 3, section 3.3.2
- SHG Microscopy, as described in Chapter 3, section 3.4

4.3 Results and Discussion

4.3.1 Shape and symmetry dependence on second harmonic generation.

In order to evaluate the interdependence between the shape, size, and symmetry of the structure and the second-harmonic signal, a first series of disks and triangles with varying sizes were fabricated by electron beam lithography. The left column of Figure 4-1a shows 20 nm-thick gold disks with diameters varying from 50 nm to 800 nm. The disk structures are transitioning to prisms with sharper apices for the structures located on the right column of Figure 4-1a. The largest triangle has a base size of 1.1 micron (bottom right structure of Figure 4-1a).

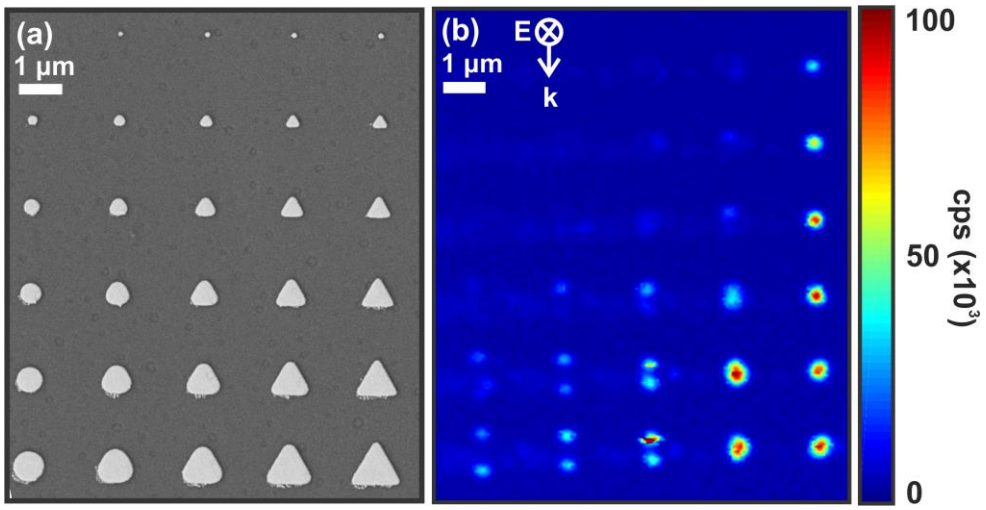

Figure 4-1 SEM image of an array of structures with various geometries and sizes (a), and the corresponding SHG microscopy image for a vertical input polarization and where both orthogonal polarizations were detected and added (b).

The corresponding polarized SHG map is shown in Figure 4-1b for the whole array with an excitation source that was vertically polarized. This first map shows clearly that the most SHG active structures are mostly coming from the prisms structures with dimensions that are comparable to the fundamental wavelength. The disk structures show little activity but nevertheless show dipolar SHG activity on the opposed sides of the disk structures. This simple experiment shows the transition from disk (C_∞ symmetry) to a

prism (C_3 symmetry) and is accompanied by a sharp increase of the SHG. The diffraction limited spatial localization of the SHG emission changes from a dipolar shape to a much more homogenous emission from a single prism structure.

4.4 SHG mapping of C_3, C_4 and C_5-symmetry dendritic structures

Dendritic fractal structures were fabricated to further increase the density of hot spots yielding a stronger surface-SHG enhancement. These structures were chosen for their controllable symmetries, as well as their tunability across a broad spectral range. The fractals structures shown in Figure 4-2a-c have C_3 (a), C_4 (b) and C_5 (c) symmetries and are organized in arrays of (50 × 50) μm^2 shown in Figure 4-2d. When structures with these nanoscale dimensions are near one another, the plasmon resonances will couple with one another resulting in a lattice-like effect. To mitigate this coupling effect, each individual structure composing the array is separated by 800 nm from the adjacent one. For the larger structures shown in figure 4-4b, despite the 800 nm gap, minor coupling can be observed along the x direction. The number of generations of the radially-extended structures varies from 4 generations for the C_3 structure (Figure 4-2a), to 2 generations for the C_4 and C_5 structures (Figure 4-2b,d).

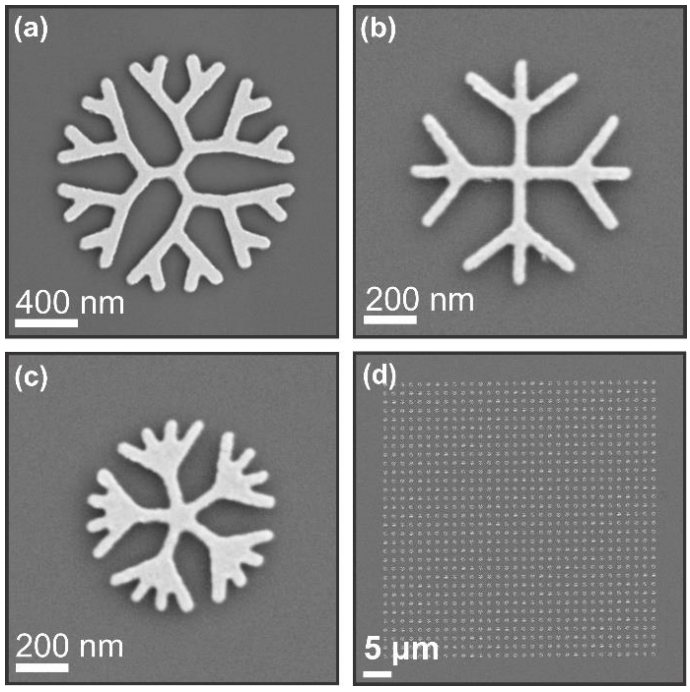

Figure 4-2 SEM images of the dendrimers produced using the EBL method. Demonstrated are three-branched generation 4 (a), four-branched generation 2 (b), five-branched generation 2 (c), and a representative array of structures (d).

The absorption spectra of these three structures were collected to evaluate the position and number of the localized surface plasmon resonances. The measurements were conducted using a specifically developed wide field microscope with a field of view that overlaps only with the inscribed array. The collected unpolarized spectra were ratioed with the background spectra collected on the glass substrate and the resulting absorbance was calculated.

The plasmon resonances of the structures are shown in Figure 4-3. Both C_3 and 4 structures have two clear resonances at 800 nm and around 590 nm corresponding to the dipolar and quadrupolar resonances, respectively. A wider background around 400 nm makes it difficult to infer the plasmonic nature of this very broad resonance. Nonetheless, from these measurements both C_3 and C_4 structures appear to have resonances that are matching the fundamental excitation (λ = 800 nm) used in this work.

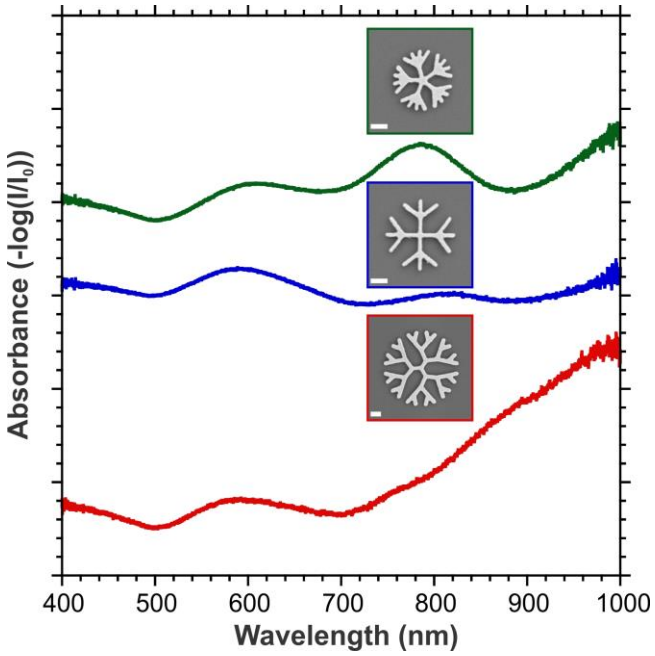

Figure 4-3 Absorption spectra for the three-branched generation four (bottom), four-branched generation 2 (middle), and five-branched generation 2 (top) dendrimers. Insets have the corresponding the dendrimer above the spectrum; the scale bar is 200 nm. The spectra are shifted for clarity.

In the following sections, we focus on the SHG maps of the individual structures for different input polarization of the excitation. For each fractal structure, the calculated maps at the fundamental and the second harmonic were calculated.

4.4.1 Fractal structure with C_3 symmetry

The three-branched structure has the most extended structure with 4 generations. The core dendron is compose of three branches of equal length and for each new generation two branches are added with a 120° angle for the second generation and with smaller angles for the third and fourth generation to avoid overlaps between the branches. The structure is characterized by a C_3 axis at the center of the structure. The maps are first collected with a horizontal polarization oriented along a branch of the core dendron. The SHG maps of 4 individual structures are shown in Figure 4-4a and show SHG activity on both sides of the structure resembling a dipolar mode as measured in spherical particles or in nanohole arrays for a linearly polarized input. The SHG calculated EM maps

(Figure 4-4b) shows a stronger signal coming from the third and fourth generation of the structure along the polarization direction, rather than its core. The FDTD map at the fundamental frequency appears more homogenously distributed over the structure (Figure 4-4c) but overall the outer generation concentrates the field more efficiently. The mapping experiments were also conducted with linear polarized light oriented perpendicularly to one arm of the structure. The resulting SHG maps (Figure 4-4d) and associated calculations (Figures 4e,f) shows a distribution of the SHG that is rotated by 90 degrees. Interestingly this set of experiments shows that the core central dendron does not participate to second-harmonic although it has locally no center of inversion. The signal intensity at the center of the structure is comparable to the background signal. One would expect larger signal coming from the center of the structure; instead, the outer portion of the structure yields larger SHG. This effect may come from the highest density of hot-spots from the periphery of the structure locally enhancing the SHG signal. The branches of the outer structures are sterically closer to each other concentrating the field more efficiently than at the center of the structure where the arms have a 120° angle between them. Furthermore, the absence of strong resonances at either 800 nm or 400 nm limits the efficiency of these structures towards SHG.

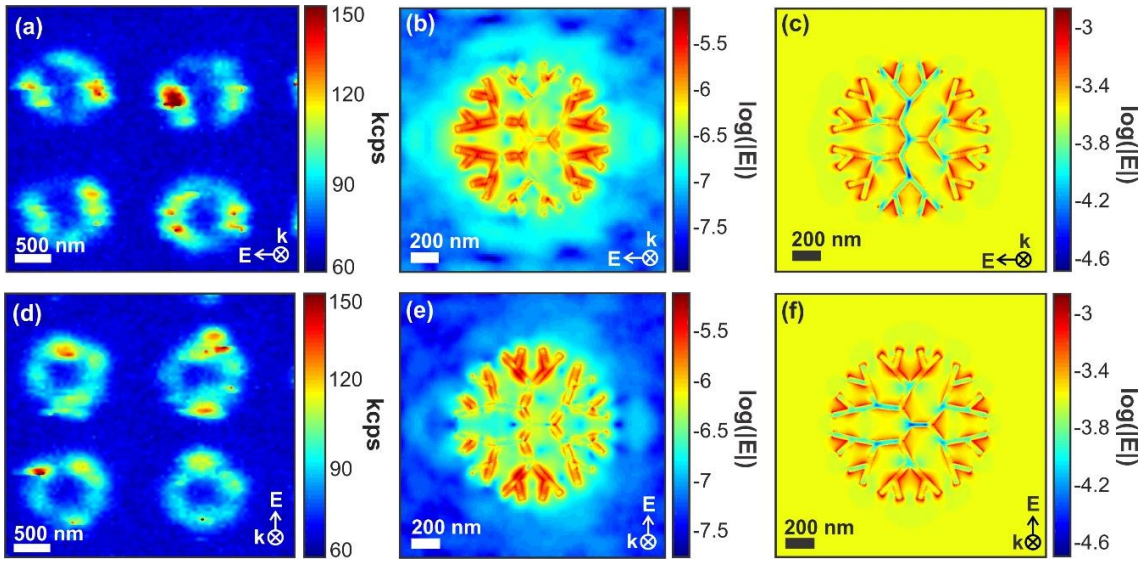

Figure 4-4 SHG images of three-branched generation 4 dendrimers with a branch length of 135 nm with a horizontal (a) and vertical (d) irradiation, FDTD simulations of the electromagnetic enhancement hotspots for the same dendrimer

with a horizontal irradiation for at 400 nm (b) and 800 nm (c), as well as the vertical irradiation at 400 nm (e) and 800 nm (f).

4.4.2 Structures with C_4 symmetry

The C_4 structure (Figure 4-5a) has a clear resonance at 800 nm as shown in Figure 4-3 which will presumably enhance the local excitation field. Nevertheless, the structure shows a center of inversion and should not exhibit any SHG activity. An SHG map (Figure 4-5b) is collected for a horizontal input polarization. A weak SHG signal is collected and the signal appears to be originating from the external dendrons as highlighted in blue in Figure 4-5a. Two SHG lobes along the polarization direction can be observed in Figure 4-5b meanwhile the core dendron does not yield any SHG signal. A series of measurements in similar experimental conditions were conducted on the C_4 core dendron alone (i.e. without the presence of the second generation dendrons). These structures did not yield any SHG signal highlighting that the symmetry selection rule for SHG holds. The presence of the SHG is therefore due to the broken symmetry from the outer dendron sites as well as more efficient field localization in these dendrons that form the second generation as shown in the electromagnetic map at both the fundamental and the second-harmonic wavelengths.

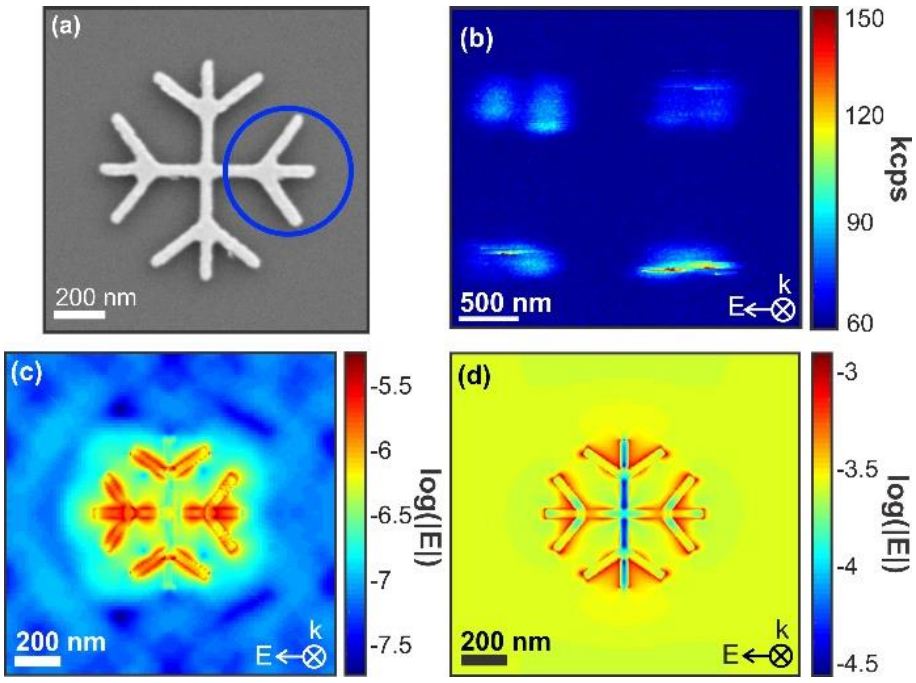

Figure 4-5 SEM image of a four-branched generation 2 dendrimer with an individual branch circled in blue for clarity (a), SHG microscopy image of these structures (b), and the simulated nonlinear enhancement hotspots at 400 nm (c) and 800 nm.

4.4.3 Structures with C_5 symmetry

Here we examine separately a series of five-branched structures considering the central C_5 dendron alone (Figure 4-6), up to the second fractal generation (Figure 4-7). Figure 4-6b shows a SHG signal arising from the core dendron. The signal is weak compared to previous experiments. The EM maps confirm the localization of the field at the center of structure as shown by a mostly circular SHG distribution.

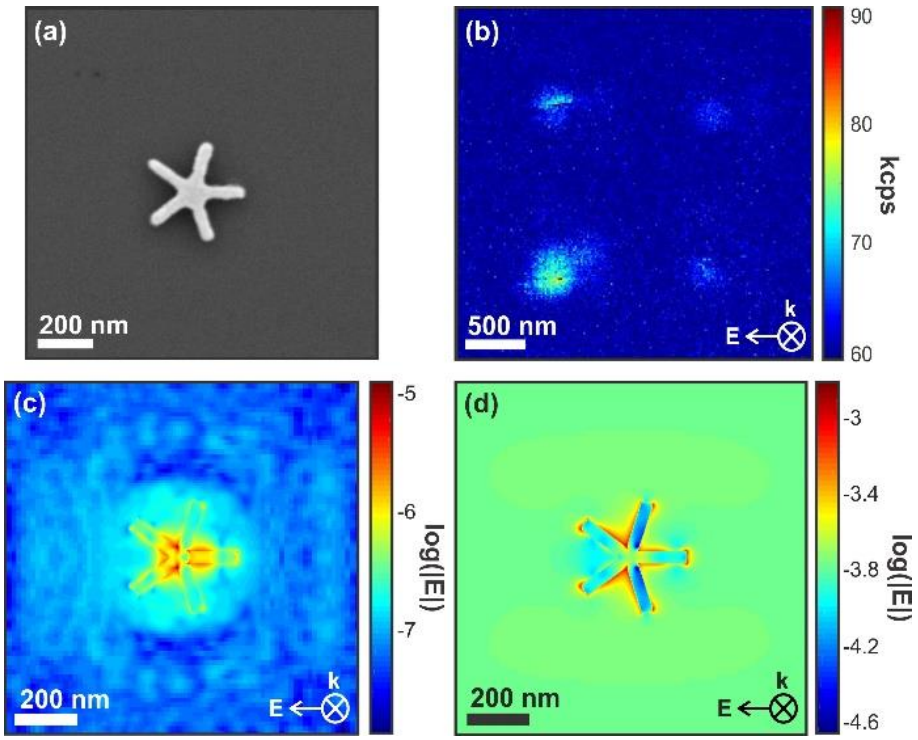

Figure 4-6 SEM image of a five-branched generation 1 dendrimer (a), SHG microscopy was performed on the structures, as demonstrated in (b), simulated electromagnetic enhancement hotspots for the five-branched generation 1 at (c) 400 nm and (d) 800 nm.

FDTD calculations shown in Figure 4-6 for the second-harmonic (c) and the fundamental (d) wavelengths confirm that the structure exhibits electromagnetic enhancement for both the fundamental wavelength of 800 nm and the second-harmonic of 400 nm, with the hotspots confined at the center of the structure. Despite the presence of SHG activity, its strength remains weak.

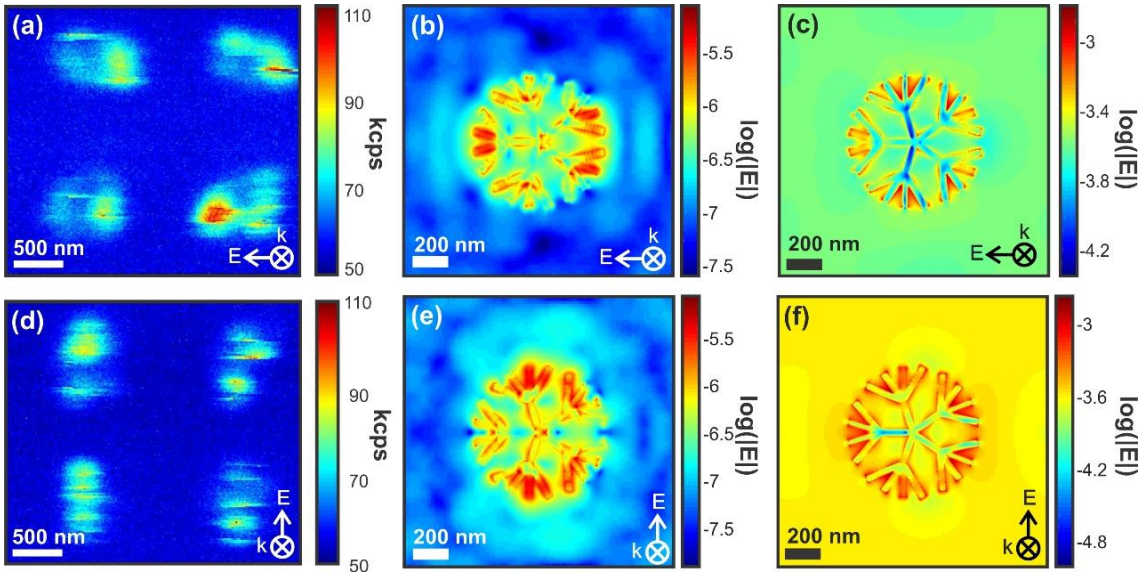

Figure 4-7 SHG images of five-branched generation 2 dendrimers with a branch length of 135 nm with a horizontal (a) and vertical (d) irradiation, FDTD simulations of the electromagnetic enhancement hotspots for the same dendrimer with a horizontal irradiation for at 400 nm (b) and 800 nm (c), as well as the vertical irradiation at 400 nm (e) and 800 nm (f).

Further experiments were conducted on a five-branched structure with the addition of a second generation. Polarization experiments were conducted along the vertical and horizontal directions. For a horizontal input polarization, two intense lobes along the polarization direction (Figure 4-7a) which is confirmed by the EM modelling at 400 nm (Figure 4-7b). For a vertical polarization the two dendrons that are oriented along the polarization direction display SHG. In both cases the field distribution at the fundamental wavelength does not display any particular directionality (Figure 4-7c,f). The dimensions of the outer dendrons were also modified with longer branches lengths of 190 nm and 250 nm. For such characteristics, out of resonance at 800 nm was observed yielding weaker signal.

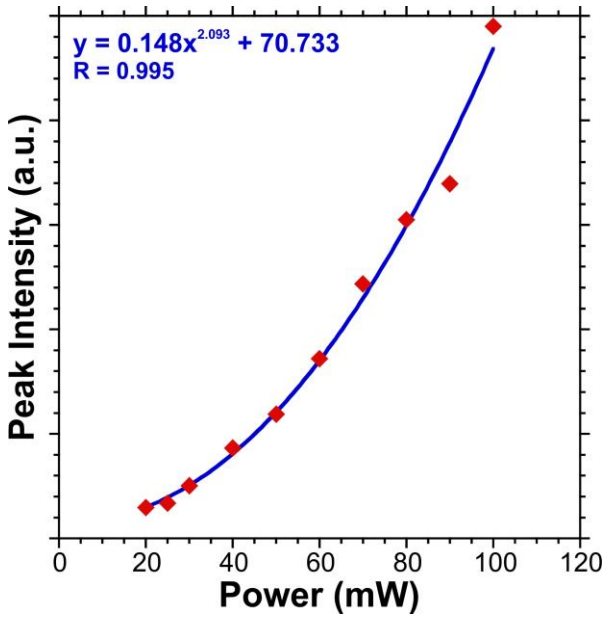

Figure 4-8 Power dependent peak intensity for a five-branched generation two dendrimer with the second order curve fit shown in blue.

Finally, the second order dependency of the SHG intensity relative to the input power of the femtosecond laser. As shown by the blue curve fit with a R value of 0.995, the SHG intensity increases exponentially by a factor of 2 as the power increases. This effectively demonstrates that it is a second-order nonlinear process. It is worth noting that at laser powers above 100 mW, the structures started to melt, therefore data points could not be obtained.

4.5 Conclusion

In the present study, gold metastructures with dendrimer geometries were successfully fabricated in arrays, and their plasmonic properties were finely tuned to place resonances at the desired wavelength. SHG microscopy was carried out on the structures that are both on- and off-resonance at 800 nm, and it was observed that the plasmonics does enhance the nonlinear optical response. Furthermore, in structures with a center of inversion, a breaking of the symmetry was observed in the individual branches, particularly near the outer dendrons, resulting in a localized non-centrosymmetry. These smaller areas of the structures acted as a contributor towards the SHG signal, despite the overall structure having a center of inversion. This localized non-centrosymmetry was

also enhanced by the presence of a plasmonic resonance. Both the structures also exhibited polarization dependence for the SHG process. Simulations were performed to calculate the electromagnetic enhancement hotspots of the dendrimers, and were compared to the absorption data, as well as the SHG emissions. The calculated absorption spectra, shown in the Chapter 3, section 3-5-1, agreed with their experimental counterparts, and it was found that the SHG emissions followed the trends shown by the simulated electromagnetic enhancement hotspots at the second-harmonic wavelength. Finally, the power dependency of the SHG signal was shown to follow a second-order exponential curve.

4.6 References

1. Perozziello, G.; Catalano, R.; Francardi, M.; Rondanina, E.; Pardeo, F.; Angelis, F. D.; Malara, N.; Candeloro, P.; Morrone, G.; Fabrizio, E. D., *Microelectron. Eng.* **2013,** *111*, 314-319.

2. Kumar, R.; Sharma, A.; Kaur, M.; Husale, S., *Adv. Opt. Mater.* **2017,** *5*, 1700009.

3. Shao, D. X.; Guo, X. G.; Zhu, Y. M.; Zhuang, S. L.; Fu, Z. L.; Cao, J. C., *J. Phys. D Appl. Phys.* **2019,** *52*, 035105.

4. Huang, X.; Jain, P. K.; El-Sayed, I. H.; El-Sayed, M. A., *Laser Med. Sci.* **2007,** *23*, 217.

5. Duempelmann, L.; Luu-Dinh, A.; Gallinet, B.; Novotny, L., *ACS Photonics* **2016,** *3*, 190-196.

6. Valev, V. K., *Langmuir* **2012,** *28*, 15454-15471.

7. Ashley, M. J.; Bourgeois, M. R.; Murthy, R. R.; Laramy, C. R.; Ross, M. B.; Naik, R. R.; Schatz, G. C.; Mirkin, C. A., *J. Phys. Chem. C* **2018,** *122*, 2307-2314.

8. Ding, Z.; Stubbs, J. M.; McRae, D.; Blacquiere, J. M.; Lagugné-Labarthet, F.; Mittler, S., *ACS Sensors* **2018,** *3*, 334-341.

9. Garcia-Rico, E.; Alvarez-Puebla, R. A.; Guerrini, L., *Chem. Soc. Rev.* **2018,** *47*, 4909-4923.

10. Wallace, G. Q.; Lagugné-Labarthet, F., *Analyst* **2019**.

11. Butet, J.; Brevet, P.-F.; Martin, O. J. F., *ACS Nano* **2015,** *9*, 10545-10562.

12. Jatirian-Foltides, E.; Escobedo-Alatorre, J.; Márquez-Aguilar, P.; Hardhienata, H.; Hingerl, K.; Alejo-Molina, A., *Rev. Mex. Fis. E* **2016,** *62*, 5-13.

13. Schlickriede, C.; Waterman, N.; Reineke, B.; Georgi, P.; Li, G.; Zhang, S.; Zentgraf, T., *Adv. Mater.* **2018,** *30*, 1703843.

14. Hermann, R. J.; Gordon, M. J., *Annu. Rev. Chem. Biomol.* **2018,** *9*, 365-387.

15. Xiao, L.; Schultz, Z. D., *Anal. Chem.* **2018,** *90*, 440-458.

16. Zhang, L.; Ding, J.; Zheng, H.; An, S.; Lin, H.; Zheng, B.; Du, Q.; Yin, G.; Michon, J.; Zhang, Y.; Fang, Z.; Shalaginov, M. Y.; Deng, L.; Gu, T.; Zhang, H.; Hu, J., *Nat. Commun.* **2018,** *9*, 1481.

17. Zong, C.; Xu, M.; Xu, L.-J.; Wei, T.; Ma, X.; Zheng, X.-S.; Hu, R.; Ren, B., *Chem. Rev.* **2018,** *118*, 4946-4980.

18. Cheng, Z.; Qiu, Y.; Li, Z.; Yang, D.; Ding, S.; Cheng, G.; Hao, Z.; Wang, Q., *Opt. Mater. Express* **2019,** *9*, 860-869.

19. Dadap, J. I.; Shan, J.; Heinz, T. F., *J. Opt. Soc. Am. B* **2004,** *21*, 1328-1347.

20. Butet, J.; Gallinet, B.; Thyagarajan, K.; Martin, O. J. F., *J. Opt. Soc. Am. B* **2013,** *30*, 2970-2979.

21. Czaplicki, R.; Kiviniemi, A.; Huttunen, M. J.; Zang, X.; Stolt, T.; Vartiainen, I.; Butet, J.; Kuittinen, M.; Martin, O. J. F.; Kauranen, M., *Nano Lett.* **2018**.

22. Butet, J.; Russier-Antoine, I.; Jonin, C.; Lascoux, N.; Benichou, E.; Martin, O. J. F.; Brevet, P.-F., *Phys. Rev. B* **2013,** *87*, 235437.

23. Jen, S.-H.; Dai, H.-L.; Gonella, G., *J. Phys. Chem. C* **2010,** *114*, 4302-4308.

24. Gottheim, S.; Zhang, H.; Govorov, A. O.; Halas, N. J., *ACS Nano* **2015,** *9*, 3284-3292.

25. Wallace, G. Q.; Foy, H. C.; Rosendahl, S. M.; Lagugné-Labarthet, F., *J. Phys. Chem. C* **2017,** *121*, 9497-9507.

Chapter 5

5 Enhancing the SHG Response in 2D MoS_2 Flakes

5.1 Introduction to Transition-Metal Dichalcogenides

Transition metal dichalcogenides (TMDs) are a class of two-dimensional (2D) materials whose crystal structure forms semiconducting monolayer flakes with a height between 0.6 and 1 nm.[1] The properties of these 2D materials have gathered interest due to their unique optical and electrochemical properties.[2-4] TMDs are layered materials composed of a layer of transition metals sandwiched between two sheets of sulfur (S) or selenide (Se).[5] Examples of transition metals typically used are molybdenum (Mo), vanadium (V), tungsten (W), and platinum (Pt). Monolayers of TMDs can be obtained by mechanical exfoliation or chemical vapour deposition (CVD), which are top-down and bottom up fabrication methods, respectively.[6] Typically, CVD is used to grow TMDs into either their octahedral crystal phase (yielding hexagonal shaped flakes) or their trigonal prismatic crystal phase (yielding triangular shaped flakes) and is the technique of choice to grow single crystals.[7] These materials also exhibit semiconductor properties that can be leveraged for electrochemical applications.[8] In addition to their conductive properties, TMDs are also photoluminescent materials with interesting linear and nonlinear optical properties.[9] TMDs have been used for a wide variety of applications, including SERS,[10] second-harmonic generation microscopy (SHGM),[11] and photoluminescence detectors.[9, 12]

5.1.1 SHG in TMDs

For MoS_2, two main TMD crystal structures, octahedral (1T) and trigonal prismatic (1H for monolayers and 2H for multilayers), are shown in Figure 5-1.[13] MoS_2 is SHG active when in its hexagonal phase. In its non-centrosymmetric crystal phase, MoS_2 flakes down to a monolayer thickness can be visualized and characterized by SHGM.

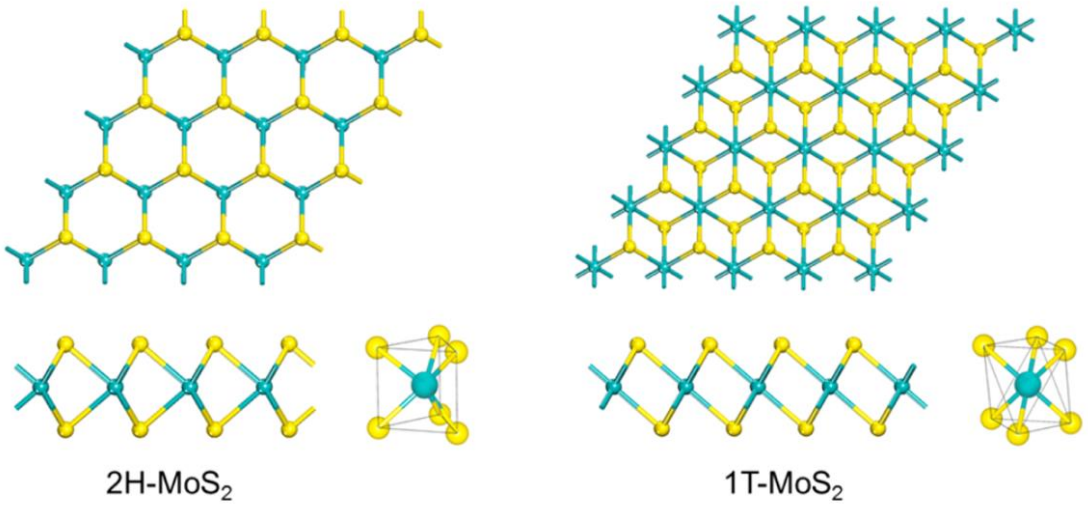

Figure 5-1 Top view (top row) and side view (bottom row) of the 2H (left) and 1T (right) structures for the molybdenum disulfide (MoS_2) monolayer. The trigonal prism coordination for the Mo atom in 2H MoS_2 and the octahedral coordination for the Mo atom in 1T-MoS_2 are also shown. Mo, cyan; S, yellow. Copyright obtained from ACS (https://pubs.acs.org/doi/10.1021/acs.chemmater.5b00986), further permissions related to the material excerpted should be directed to the ACS.

TMD flakes such as MoS_2, $MoSe_2$, WS_2, CdS, and more, have been thoroughly studied for their nonlinear optical properties in their 2H phase.[14-17] These studies have included SHG characterization of various TMD flakes,[18-21] such as WS_2 flakes with spiral structures,[22, 23] as well as higher harmonic sensing such as third-harmonic generation.[24, 25] While a select few studies have reported using plasmonic materials to enhance the photoluminescence properties of MoS_2 flakes,[12, 26] even fewer have reported enhancing the nonlinear optical properties of TMDs.[27] Thus, the main focus of this chapter is the effects of functionalization with an organic dye, which acts in both the abruption of the incident light and subsequently as an energy donor to the MoS_2. The organic dye will therefore influence the SHG emissions of MoS_2 flakes without an observable change to its polarization-dependent SHG.

5.2 Methods

The following methods were used throughout this chapter:

- Flakes were prepared CVD as described in Chapter 3, section 3.2.3.
- MoS_2 flake surfaces were functionalized by soaking the substrate in a 10 mM solution of rhodamine 6G (R6G) dye for 2 hours, rinsing with Milli-Q® (18.2 MΩ/cm^3) water for 10 minutes, and gently drying using nitrogen gas.
- Raman spectra were obtained using a Horiba XploRA^{TM} PLUS confocal Raman spectrometer equipped with a 532 nm excitation wavelength, 100 × (NA = 0.7) objective (Mitutoyo), and 1200 grooves/mm grating.
- SHGM measurements were performed as described in Chapter 3, section 3.4.

5.3 Calculating the MoS_2 Polarization-Dependent SHG Signal

Since the SHG process is dependent on the physical properties of the material under investigation, the polarization-dependent response can be calculated mathematically. As mentioned in Chapter 2, the SHG signal intensity varies with the square of the effective nonlinear susceptibility tensor, $\overleftrightarrow{\chi}^2_{eff}$:

$$\overleftrightarrow{\chi}^2_{eff} = \left(\overleftrightarrow{L}_{2\omega} \cdot E_{2\omega}\right) \cdot \overleftrightarrow{\chi}^{(2)}_S : (\overleftrightarrow{L}_{\omega} \cdot E_{\omega})(\overleftrightarrow{L}_{\omega} \cdot E_{\omega}) \quad [5\text{-}1]$$

and similar to equation [2-7],

$$I(2\omega) \sim \left|\overleftrightarrow{\chi}^{(2)}_{eff}\right|^2 [I(\omega)]^2 \quad [5\text{-}2]$$

where $L_{\omega,2\omega}$ are the Fresnel factor at the fundamental (ω) and second harmonic (2ω) frequencies, $\overleftrightarrow{\chi}^{(2)}_S$ is the nonlinear susceptibility of the crystalline material, and E is the polarization vector at the fundamental (ω) and second harmonic (2ω) frequencies. The theoretical second-order nonlinear susceptibility, $\overleftrightarrow{\chi}^{(2)}_S$, is a 3×3×3 tensor that represents the physical properties of a material and can be written as:

$$\overleftrightarrow{\chi}_S^{(2)} = \begin{bmatrix} \begin{bmatrix} xxx & xyx & xzx \\ xxy & xyy & xzy \\ xxz & xyz & xzz \end{bmatrix} \\ \begin{bmatrix} yxx & yyx & yzx \\ yxy & yyy & yzy \\ yxy & yyz & yzz \end{bmatrix} \\ \begin{bmatrix} zxx & zyx & zzx \\ zxy & zyy & zzy \\ zxz & zyz & zzz \end{bmatrix} \end{bmatrix} \quad [5\text{-}3]$$

The MoS_2 flakes studied in this chapter are in their 2H crystal phase, which have a point group of D_{3h}. For the D_{3h} point group only 4 $\overleftrightarrow{\chi}_S^{(2)}$ tensor elements are non-vanishing:[28]

$$(yyy) = (-yxx) = (-xxy) = (-xyx) \quad [5\text{-}4]$$

By incorporating [5-4] into $\overleftrightarrow{\chi}_S^{(2)}$, the following three-dimensional tensor is obtained:

$$\chi_{D_{3h}}^{(2)} = \begin{bmatrix} \begin{bmatrix} 0 & -yyy & 0 \\ -yyy & 0 & 0 \\ 0 & 0 & 0 \end{bmatrix} \\ \begin{bmatrix} -yyy & 0 & 0 \\ 0 & yyy & 0 \\ 0 & 0 & 0 \end{bmatrix} \\ \begin{bmatrix} 0 & 0 & 0 \\ 0 & 0 & 0 \\ 0 & 0 & 0 \end{bmatrix} \end{bmatrix} \quad [5\text{-}5]$$

From here, there are two possible calculations for the second-harmonic intensity, $I(2\omega)$: the first involves keeping the flake at a fixed angle and rotating the input polarization, while the second involves keeping the input polarization at a fixed angle and rotating the flake itself. For this study, the first option was chosen because it is experimentally easier to rotate the polarization of a laser beam compared to keeping the centre of rotation fixed of a micro-sized single flake. Therefore, the MoS_2 flakes have their long axis as $\theta = 0°$ (Figure 5-2), where θ indicates the rotation of the input polarization with respect to the crystallographic main axis. The output signal is collected along the p-polarization, which is parallel to the long axis of the crystal structure.

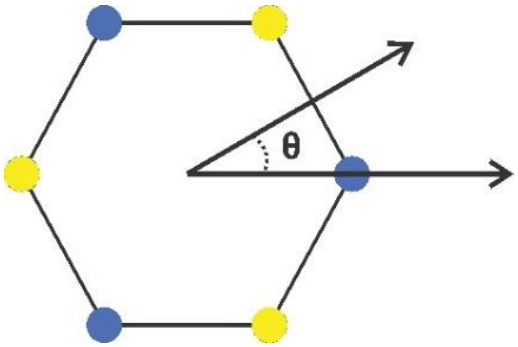

Figure 5-2 A representative crystal lattice of the 2H MoS_2 where the yellow nodes are S atoms, and the blue nodes are Mo atoms. The long (x) axis intersects an Mo atom, and the input polarization angle is indicated by θ.

The rotation of two photons with variable input polarization, $E_{in}(\omega)$, is defined as the vector:

$$E_{in}(\omega) = \begin{bmatrix} A \cdot \cos(\theta) \\ A \cdot \sin(\theta) \\ B \end{bmatrix} \quad [5\text{-}6]$$

where A and B represents the input wavelength intensity and photon propagation direction, respectively. The output photon polarized along the x-axis, $E_{out}(x)$, is defined as:

$$E_{out}(x) = \begin{bmatrix} 1 \\ 0 \\ 0 \end{bmatrix} \quad [5\text{-}7]$$

Similarly, the output photon polarized along the y-axis, $E_{out}(y)$, is defined as:

$$E_{out}(y) = \begin{bmatrix} 0 \\ 1 \\ 0 \end{bmatrix} \quad [5\text{-}8]$$

Multiplying [5-5] by [5-6] twice to account for the 2 photons in the SHG process and the identity matrix, R, (to account for the fixed angle of the flake), defines $I(2\omega)$ as:

$$I(2\omega) = \begin{bmatrix} -2 \cdot A^2 \cdot yyy \cdot \cos(\theta) \cdot \sin(\theta) \\ A^2 \cdot yyy \cdot \sin^2(\theta) - A^2 \cdot yyy \cdot \cos^2(\theta) \\ 0 \end{bmatrix} E_{out} \quad [5\text{-}9]$$

When the output polarization direction is accounted for by multiplying [5-9] by [5-7] as the output analyzer and further multiplied by the resulting transposed vector, $I(2\omega)$ becomes a scalar:

$$I(2\omega) = 4 \cdot A^4 \cdot yyy^2 \cdot \cos^2(\theta) \cdot \sin^2(\theta) \quad [5\text{-}10]$$

Since $4 \cdot \cos^2(\theta) \cdot \sin^2(\theta) = \sin^2(2\theta)$, [5-10] can be simplified to:

$$I(2\omega) = A^4 \cdot yyy^2 \cdot \sin^2(2\theta) \quad [5\text{-}11]$$

Because factors A and yyy are constant, $I(2\omega)$ will vary proportionally to the input polarization angle:

$$I(2\omega) \propto \sin^2(2\theta) \quad [5\text{-}12]$$

Therefore, for a variable polarization along θ and an analyzer oriented along the x-axis, the SHG signal variation follows the $\sin^2(2\theta)$ law, yielding a four-lobed SHG polar plot.[29, 30] However, if the output analyzer was oriented along the y-axis, the SHG signal variation would follow the $\cos^2(2\theta)$ law:

$$I(2\omega) \propto \cos^2(2\theta) \quad [5\text{-}13]$$

The difference between [5-12] and [5-13] is shown in Figure 5-3, which highlights a rotation of the four lobes by 90°. This analysis indicates that the polarization pattern for a MoS_2 flake is expected to show a 4 lobes symmetry. The orientation of the lobes depends on the polarization direction with respect to the 2D crystal symmetry axes.

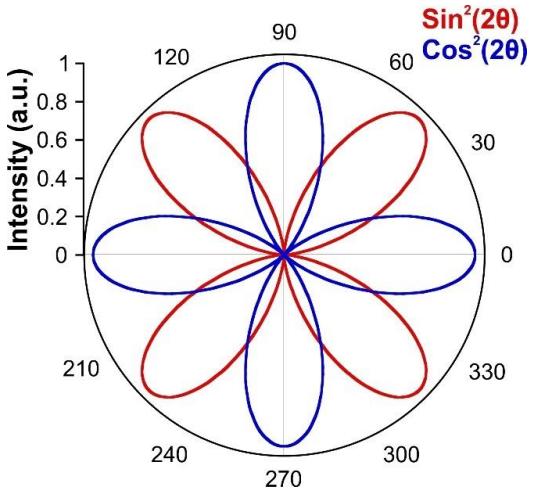

Figure 5-3 Polar plots showing $\sin(2\theta)^2$ (red) and $\cos(2\theta)^2$ (blue).

5.4 Characterization of MoS_2 Flakes

Monolayer TMD flake characterization can be challenging due to their sub-nanometer thickness. The MoS_2 flakes studied here are grown on a SiO_2/Si substrate and are large enough (few to tens of microns) to be visualized by an optical microscope (Figure 5-4a). The SiO_2/Si substrate is also important to observe the flake through reflection from the substrate interface. A thickness of the SiO_2 ranging between 200 to 300 nm enables the observation of a sub nm TMD flake grown on its surface. Further observation by SEM can discern the lateral dimensions of the flakes, but not their height (Figure 5-4b). Atomic force microscopy (AFM), however, provides 3D nanoscale spatial resolution, and was therefore used to study MoS_2 flake height (Figure 5-4c). AFM imaging reveals that mono- and bilayer MoS_2 flakes are 0.8 nm and 1.6 nm thick, respectively (Figure 5-4d). Previous studies have shown that an effective method for functionalizing MoS_2 flake surfaces involves exploiting vacancies in the S layers; however, this method is most successful on mechanically-exfoliated flakes.[31, 32] Balasubramanian et al. have demonstrated gentle, surface-specific functionalization of MoS_2 flakes by soaking substrates in R6G, an organic dye (Figure 5-4e), and rinsing with deionized water.[33] This latter method was therefore used to functionalize MoS_2 monolayer flakes,

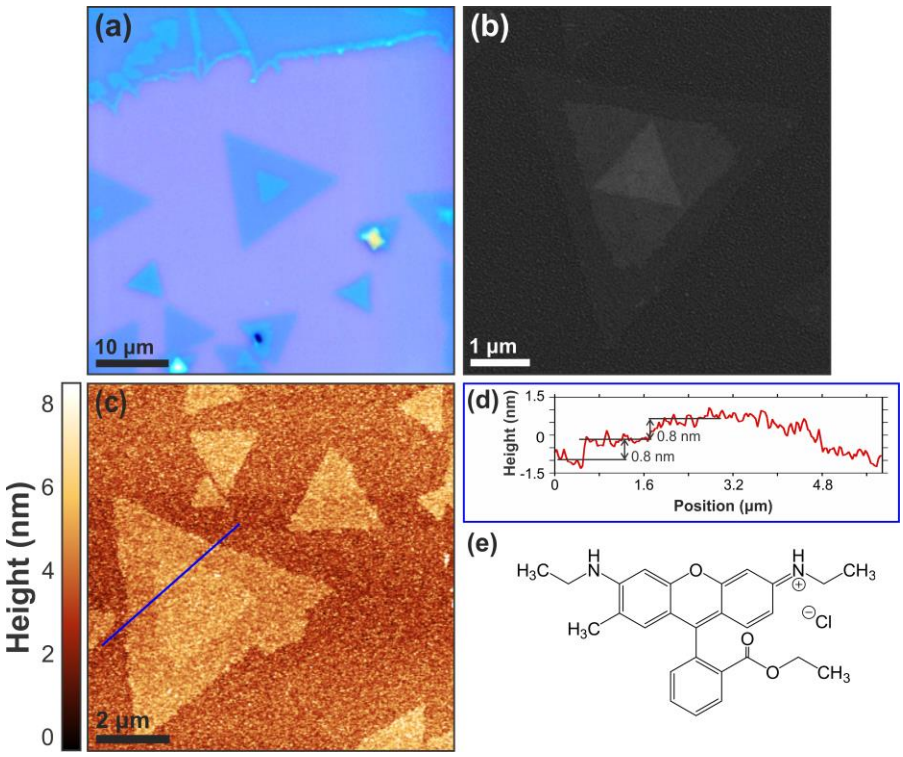

Figure 5-4 (a) An optical, (b) SEM, and (c) AFM image of a multilayered MoS_2 flake. (d) A cross-section along an MoS_2 bilayer, indicated by the blue line in c). (e) The chemical structure of R6G dye.

The SHG signal of a series of MoS_2 flakes was measured prior to functionalization. The SHG map shows the emission of the second harmonic generation detected at 400 nm over the whole flake for an input excitation at 800 nm that is horizontally polarized (Figure 5-5). A crisp SHG signal from the outline and the surface of the flake can be noticed highlighting a better contrast than SEM or AFM (Figure 5-5). An intense signal is located at the centre of the main flake, revealing the nucleation site of a second layer. While most smaller flakes have smooth edges, the larger flake shown in Figure 5-5 contains defects along its edges; despite imperfections, the overall SHG signal has a larger magnitude in larger flakes compared to the SHG signal emitted from the majority of the smaller flakes in the same image.

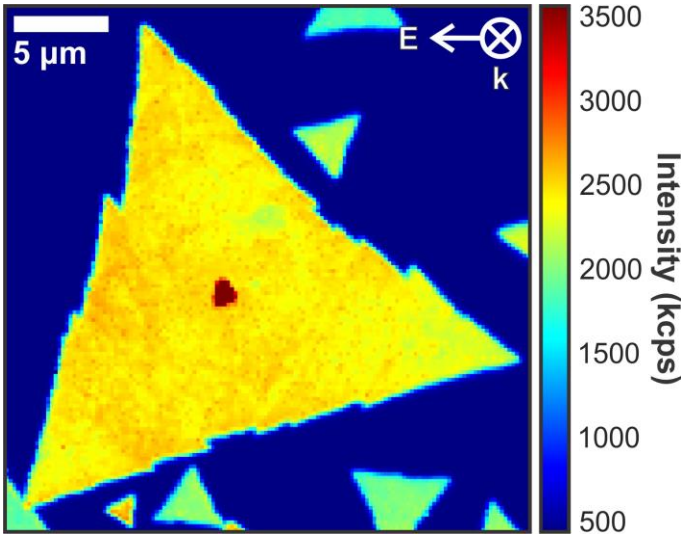

Figure 5-5 SHGM of an MoS_2 flake with a side length of 27 µm.

Multilayer MoS_2 flakes were also studied by SHG microscopy. Zheng et al. have previously reported SHG signals of multilayer TMDs grown by CVD, and demonstrated that SHG signals increase with an increasing number of TMD layers.[34] Other studies have shown artificially-stacked MoS_2 bilayers (i.e., layers that were not naturally grown on top of each other, but mechanically transferred) have constructive and destructive interferences that vary based on whether the base of the flakes are angled from 0° to 60°, respectively, relative to one another.[16, 30] In other words, if the base of an overlayed TMD layer has an angle of 60° relative to the first layer, the SHG signal is effectively canceled out due to destructive interference. However, this is not the case on multi-layered flakes as grown by CVD. Figure 5-6 shows the step-wise increase of the SHG signal relative to the number of layers present, with a cross-section of the SHG map inset as indicated by the dotted white line.

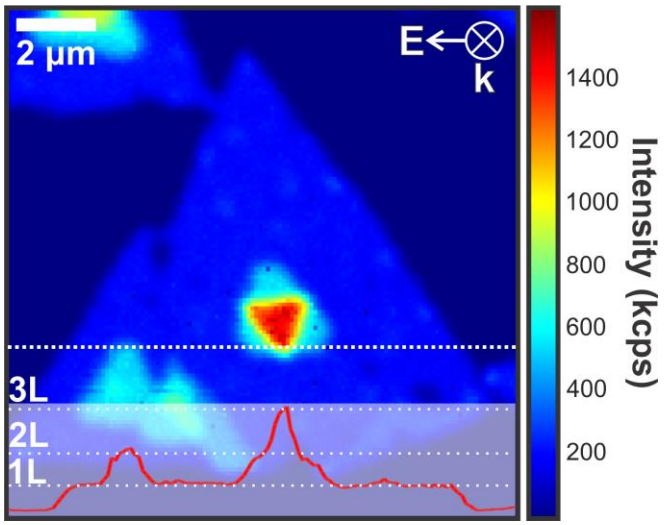

Figure 5-6 SHGM of a multilayer MoS_2 flake with a cross-section of the SHG intensity (shown by the dotted line) inset.

5.5 SHGM of Functionalized MoS_2 Flakes

The two characteristic Raman modes for MoS_2 flakes are located at 383 cm^{-1} and 402 cm^{-1}, which correspond to the E_{2G} (in-plane) and A_{1G} (out-of-plane) modes, respectively. These characteristic peaks were visible in the Raman spectra of MoS_2 flakes both pre- and post-functionalization, which are the red and blue spectra, respectively (Figure 5-7a). The mode at 530 cm^{-1} is the phonon mode of the SiO_2/Si substrate. In the functionalized MoS_2 spectrum, the higher wavenumber modes (i.e., above 520 cm^{-1}) correspond to the vibrational modes of the R6G molecule. Raman shifts of 383 cm^{-1} and 402 cm^{-1} were selected for the confocal Raman mapping of MoS_2 (Figure 5-7b), while the peak at 1362 cm^{-1} (representing aromatic C-C ring stretching) was selected for R6G mapping (Figure 5-7c).[35, 36] These data demonstrate that R6G selectively functionalizes on MoS_2 flake rather than across the entire substrate surface.

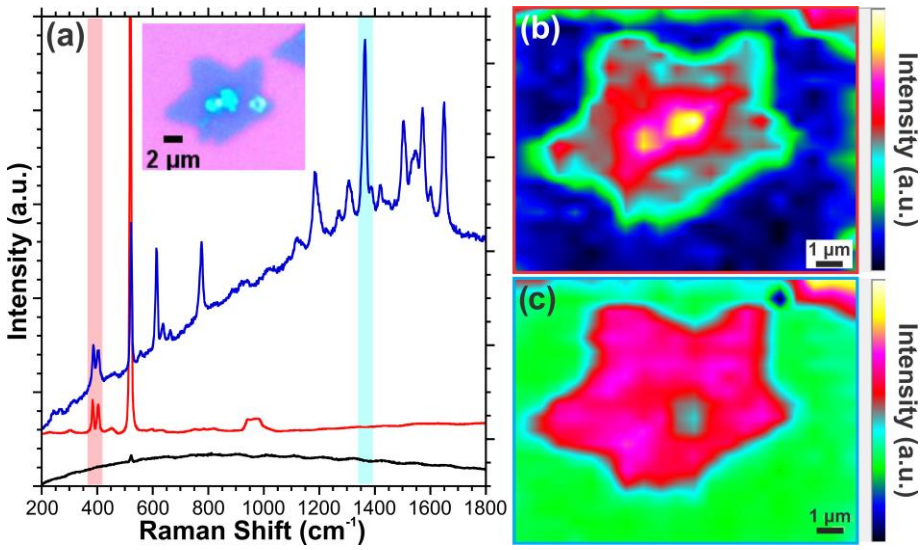

Figure 5-7 (a) Raman Spectra of the Si/SiO_2 substrate (black), bare MoS_2 flakes (red), and MoS_2 flakes after R6G functionalization (blue). The common modes at 520 cm^{-1} is the lattice mode of the Silicon substrate (b) Confocal Raman map of the peaks at 383 cm^{-1} and 402 cm^{-1} (highlighted in red in a) and (c) the peak at 1362 cm^{-1} (highlighted in blue in a).

Fiore et al. have shown that the SHG signal arising from Si and the time-dependent SHG response increase with increasing surface dopant density (past 10^{18} cm^{-3}).[37] A similar response was observed when functionalizing the MoS_2 flakes with R6G: SHG signal enhancement increased from 20% (Figure 5-8a,b) to 50% (Figure 5-8c,d) post-functionalization. When R6G is in close proximity to the MoS_2 surface, MoS_2 photosensitization occurs in conjunction with a charge transfer effect.[33] Taghinejad et al. have also reported the effects of photocarriers on MoS_2 flake nonlinear optical properties; their results demonstrated that interactions between TMDs and light can be controlled and promoted by photocarrier proximity to the surface of the TMD flakes.[38]

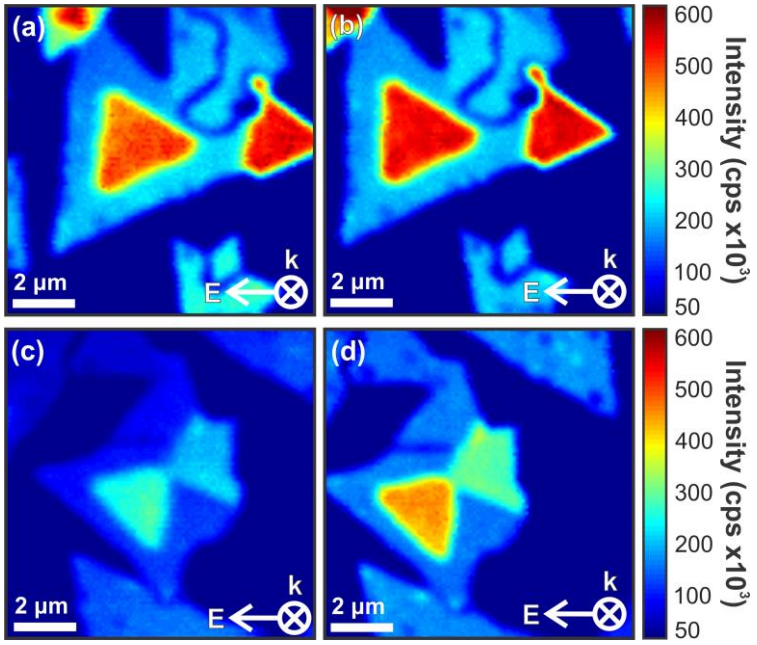

Figure 5-8 SHG maps of an MoS_2 bilayer before (a,c) and after (b,d) functionalization with R6G dye.

Polarization-dependent SHG (PD-SHG) measurements were performed to confirm to compare it with the predictions considering the symmetry of the crystal (Figure 5-9).

In these measurements, the input polarization is varied over 360° and the collected signal is analyzed along the X direction. For each polarization angle, a SHG measurement is collected. Repeating this over 360° yield to polar plots that are shown in Figures 9b-f for selected points over the Si substrate as well as the monolayer, bilayer and trilayer of MoS_2. The polarized SHG emission from the SiO_2/Si substrate shows a circular polarized pattern with no particular structure which is representative of the amorphous SiO_2 layer. Regardless of MoS_2 flake thickness, the SHG polar pattern is a crisp four-lobed shape as expected from the MoS_2 crystal symmetry and described in section 5.3 of this chapter. While a SHG signal magnitude increase of 50% was observed upon R6G functionalization, the polarized polar plots always show 4 lobes as shown in Figure 9c-f. This indicates that the symmetry of the crystal is kept even for bi- and trilayers are grown over the initial layer. This indicates that the multiple layers are grown during the CVD process showing similar orientation or orientation tilted by 60° from the underneath layer. Other orientations of artificially stacked layers would yield possible destructive

interferences and abnormally-shaped PD-SHG signal.[16, 39] The trilayer grown by CVD, despite appearing to be rotated by 60° relative to the flake below it, was nucleated by the bilayer. This will lead to the crystal structure with an orientation similar to the flakes below it, and thus enhancing the SHG signal rather than lower it.

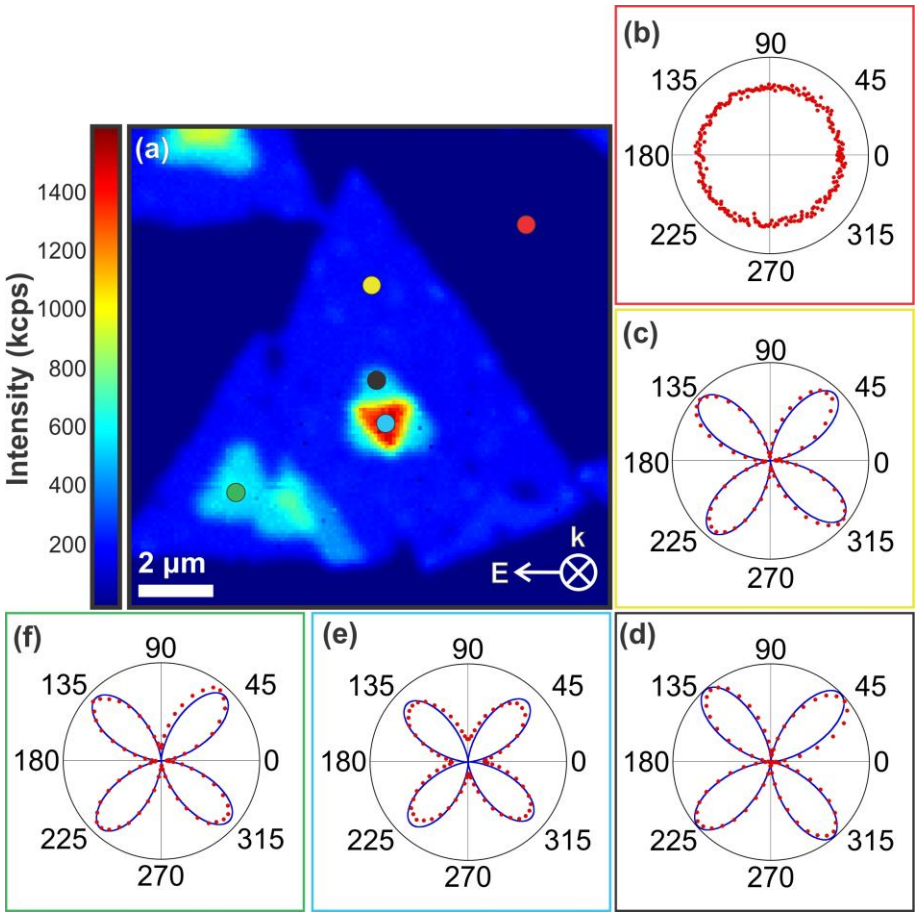

Figure 5-9 (a) An SHGM image of a functionalized MoS_2 trilayer with SHGM intensity polar plots of the (b) substrate and an MoS_2 (c) monolayer, (d) bilayer, and (e) trilayer, as well as (f) a second MoS_2 bilayer. The red data points in (b-f) represent the experimental values, while the blue lines in (c-f) represent the $\sin^2(2\theta)$ fit and were added as a guide to the eye.

5.6 Conclusion

Mono- and multilayer MoS_2 flakes were successfully synthesized by CVD and subsequently characterized by Raman spectroscopy and AFM. The flakes were further

studied by SHGM, and their PD-SHG signals yielded four-lobed polar plots. The flakes were also functionalized with the R6G dye, which enhanced SHG signal intensity by 50%. Lastly, the PD-SHG signal of the dye-sensitized MoS_2 flakes was also for mono-, bi-, and trilayer flakes. These preliminary results from functionalized MoS_2 flakes will lead to future studies on the effects of a range of surface dopants using a range of either homogenous or hybrid TMD flakes to discern and better understand the enhancement mechanisms and to optimize the linear and nonlinear optical properties of the TMD flakes.

5.7 References:

1. Akinwande, D.; Brennan, C. J.; Bunch, J. S.; Egberts, P.; Felts, J. R.; Gao, H.; Huang, R.; Kim, J.-S.; Li, T.; Li, Y.; Liechti, K. M.; Lu, N.; Park, H. S.; Reed, E. J.; Wang, P.; Yakobson, B. I.; Zhang, T.; Zhang, Y.-W.; Zhou, Y.; Zhu, Y., *Extreme Mech. Lett.* **2017,** *13*, 42-77.

2. Yu, S.; Wu, X.; Wang, Y.; Guo, X.; Tong, L., *Adv. Mater.* **2017,** *29*, 1606128.

3. Zhang, X.; Chen, A.; Chen, L.; Zhou, Z., *Adv. Energy Mater.* **2021,** *n/a*, 2003841.

4. Ma, Z.; Tahersima, M. H.; Khan, S.; Sorger, V. J., *IEEE J. Sel. Top. Quantum Electron.* **2017,** *23*, 81-88.

5. Manzeli, S.; Ovchinnikov, D.; Pasquier, D.; Yazyev, O. V.; Kis, A., *Nat. Rev. Mater.* **2017,** *2*, 17033.

6. Samadi, M.; Sarikhani, N.; Zirak, M.; Zhang, H.; Zhang, H.-L.; Moshfegh, A. Z., *Nanoscale Horiz.* **2018,** *3*, 90-204.

7. Berry, J.; Zhou, S.; Han, J.; Srolovitz, D. J.; Haataja, M. P., *Phys. Rev. Mater.* **2018,** *2*, 114002.

8. Ciarrocchi, A.; Avsar, A.; Ovchinnikov, D.; Kis, A., *Nat. Commun.* **2018,** *9*, 919.

9. Severs Millard, T.; Genco, A.; Alexeev, E. M.; Randerson, S.; Ahn, S.; Jang, A. R.; Suk Shin, H.; Tartakovskii, A. I., *NPJ 2D Mater. Appl.* **2020,** *4*, 12.

10. Fraser, J. P.; Postnikov, P.; Miliutina, E.; Kolska, Z.; Valiev, R.; Švorčík, V.; Lyutakov, O.; Ganin, A. Y.; Guselnikova, O., *ACS Appl. Mater. Interfaces* **2020,** *12*, 47774-47783.

11. Beach, K.; Lucking, M. C.; Terrones, H., *Phys. Rev. B* **2020,** *101*, 155431.

12. Yu, S. H.; Lee, Y.; Jang, S. K.; Kang, J.; Jeon, J.; Lee, C.; Lee, J. Y.; Kim, H.; Hwang, E.; Lee, S.; Cho, J. H., *ACS Nano* **2014,** *8*, 8285-8291.

13. Tang, Q.; Jiang, D.-e., *Chem. Mater.* **2015,** *27*, 3743-3748.

14. Zhang, W.; Zhang, Y.; Qiu, J.; Zhao, Z.; Liu, N., *InfoMat* **2021,** *3*, 133-154.

15. Ma, R.; Sutherland, D. S.; Shi, Y., *Mater. Today* **2021,** *50*, 570-586.

16. Kim, Y. C.; Yoo, H.; Nguyen, V. T.; Lee, S.; Park, J.-Y.; Ahn, Y. H., *Nanomaterials* **2021,** *11*, 1786.

17. Wang, Y.; Xiao, J.; Yang, S.; Wang, Y.; Zhang, X., *Opt. Mater. Exp.* **2019,** *9*, 1136-1149.

18. Zimmermann, J. E.; Kim, Y. D.; Hone, J. C.; Höfer, U.; Mette, G., *Nanoscale Horiz.* **2020,** *5*, 1603-1609.

19. Mennel, L.; Paur, M.; Mueller, T., *APL Photonics* **2019,** *4*, 034404.

20. Seyler, K. L.; Schaibley, J. R.; Gong, P.; Rivera, P.; Jones, A. M.; Wu, S.; Yan, J.; Mandrus, D. G.; Yao, W.; Xu, X., *Nat. Nanotechnol.* **2015,** *10*, 407-411.

21. Hsu, W.-T.; Zhao, Z.-A.; Li, L.-J.; Chen, C.-H.; Chiu, M.-H.; Chang, P.-S.; Chou, Y.-C.; Chang, W.-H., *ACS Nano* **2014,** *8*, 2951-2958.

22. Fan, X.; Ji, Z.; Fei, R.; Zheng, W.; Liu, W.; Zhu, X.; Chen, S.; Yang, L.; Liu, H.; Pan, A.; Agarwal, R., *Nano Lett.* **2020,** *20*, 2667-2673.

23. Fan, X.; Jiang, Y.; Zhuang, X.; Liu, H.; Xu, T.; Zheng, W.; Fan, P.; Li, H.; Wu, X.; Zhu, X.; Zhang, Q.; Zhou, H.; Hu, W.; Wang, X.; Sun, L.; Duan, X.; Pan, A., *ACS Nano* **2017,** *11*, 4892-4898.

24. Wen, X.; Gong, Z.; Li, D., *InfoMat* **2019,** *1*, 317-337.

25. Autere, A.; Jussila, H.; Dai, Y.; Wang, Y.; Lipsanen, H.; Sun, Z., *Adv. Mater.* **2018,** *30*, 1705963.

26. Kumar, R.; Sharma, A.; Kaur, M.; Husale, S., *Adv. Opt. Mater.* **2017,** *5*, 1700009.

27. Han, X.; Wang, K.; Persaud, P. D.; Xing, X.; Liu, W.; Long, H.; Li, F.; Wang, B.; Singh, M. R.; Lu, P., *ACS Photonics* **2020,** *7*, 562-568.

28. Boyd, R., Chapter 1. The Nonlinear Optical Susceptibility. 2003; pp 1-65.

29. Balla, N. K.; O'Brien, M.; McEvoy, N.; Duesberg, G. S.; Rigneault, H.; Brasselet, S.; McCloskey, D., *ACS Photonics* **2018,** *5*, 1235-1240.

30. Li, D.; Xiong, W.; Jiang, L.; Xiao, Z.; Rabiee Golgir, H.; Wang, M.; Huang, X.; Zhou, Y.; Lin, Z.; Song, J.; Ducharme, S.; Jiang, L.; Silvain, J.-F.; Lu, Y., *ACS Nano* **2016,** *10*, 3766-3775.

31. Knirsch, K. C.; Berner, N. C.; Nerl, H. C.; Cucinotta, C. S.; Gholamvand, Z.; McEvoy, N.; Wang, Z.; Abramovic, I.; Vecera, P.; Halik, M.; Sanvito, S.; Duesberg, G. S.; Nicolosi, V.; Hauke, F.; Hirsch, A.; Coleman, J. N.; Backes, C., *ACS Nano* **2015,** *9*, 6018-6030.

32. Chiu, N.-F.; Lin, T.-L., *Talanta* **2018,** *185*, 174-181.

33. Balasubramanian, K.; Swaminathan, H., *Sens. Actuators B Chem.* **2018,** *259*, 980-989.

34. Zheng, J.; Yan, X.; Lu, Z.; Qiu, H.; Xu, G.; Zhou, X.; Wang, P.; Pan, X.; Liu, K.; Jiao, L., *Adv. Mater.* **2017,** *29*, 1604540.

35. He, X. N.; Gao, Y.; Mahjouri-Samani, M.; Black, P. N.; Allen, J.; Mitchell, M.; Xiong, W.; Zhou, Y. S.; Jiang, L.; Lu, Y. F., *Nanotechnology* **2012,** *23*, 205702.

36. Van Dyck, C.; Fu, B.; Van Duyne, R. P.; Schatz, G. C.; Ratner, M. A., *J. Phys. Chem. C* **2018,** *122*, 465-473.

37. Fiore, J. L.; Fomenko, V. V.; Bodlaki, D.; Borguet, E., *Appl. Phys. Lett.* **2011,** *98*, 041905.

38. Taghinejad, M.; Xu, Z.; Wang, H.; Taghinejad, H.; Lee, K.-T.; Rodrigues, S. P.; Adibi, A.; Qian, X.; Lian, T.; Cai, W., *Small* **2020,** *16*, 1906347.

39. Psilodimitrakopoulos, S.; Mouchliadis, L.; Paradisanos, I.; Kourmoulakis, G.; Lemonis, A.; Kioseoglou, G.; Stratakis, E., *Sci. Rep.* **2019,** *9*, 14285.

Chapter 6

6 Single-Beam Inscription of Plasmon-Induced Surface Gratings

(A version of this manuscript has been published in *Optical Materials*: Therien, D.A.B.; Ćulum, N.M.; McRae, D.M.; Mazaheri, L.; Lagugné-Labarthet, F. *Opt. Mater.*, **2021**, *112*, 110775. https://doi.org/10.1016/j.optmat.2020.110775)

The formation of gratings on gold nanoprisms arrays by plasmon-mediated reduction of a diazonium salt is investigated. Nanosphere lithography (NSL) is used to produce large surfaces of gold nanoprisms that are effective at reducing diazonium salts by producing hot electrons through excitation of localized surface plasmon resonances (LSPRs). Using single beam irradiation, we report here on the formation of periodic structures formed from the diazonium salts and that follow the NSL structures. On plasmonically active nanoprism substrates, the electric field enhancement promotes chemical reduction and hence modifies the grafting direction and grating properties of the ripples. The nanoprisms act as a plasmon guide which widens the pitch of the self-organized gratings and can even alter it from straight lines into a crisscross pattern.

6.1 Introduction

Highly periodic surface gratings can develop upon single beam illumination on solids and liquids using either continuous-wave (CW) or pulsed lasers, provided that the illumination has a sufficient energy density.[1] Self-organized regular patterns emerge from interaction between an input optical field of the single beam and an initial variation of the physical or electromagnetic properties of the illuminated surface.[2, 3]These self-organized gratings produced under pulsed illumination are usually referred to as laser-induced periodic surface structures (LIPSS) in literature, where the irreversible ripples form lines parallel to the polarization direction.[3-5] The formation process and the subsequent grating properties can differ noticeably depending on the experimental opto-geometric conditions such as laser intensity, polarization state, angle of incidence, wavelength, material roughness and index of refraction of the sample.

The self-organization mechanism is explained considering the formation of a spontaneous interference pattern and its coupling with the substrate that yields the structure formation.[1, 6] Self-organized structures can appear on surfaces which support plasmons modes, polaritons, or surface-standing waves, [7-10] as well as bare dielectric surfaces.[11, 12] Specifically, the formation of self-organized interference patterns is correlated with the coupling between the incident beam and the scattered beam onto the surface of the sample. This self-organization mechanism is analogous to Wood's anomalies in metallic diffraction gratings whereby coupling of one of the primary diffraction orders with the sample is effective at the grazing angle.[1] The sample surface can have initial variation of any optical physical properties. Examples of such surface irregularities include surface roughness, defect density, or gradient of refraction index.

Surface irregularities can be considered as a spatial frequency which diffracts the incident beam into different directions following the Rayleigh diffraction law.[1, 13] The incident beam is perturbated from the surface irregularities and scattered into different directions depending on the incoming wavelengths and the incident angle. One range of surface irregularities with a specific spatial frequency can scatter the beam into the surface of the sample. The interference pattern formed by the input beam and the scattered contribution at the grazing angle will impinge on the sample surface and interact with the material. Light-matter interaction further enhances the surface irregularities in a feedback loop fashion. This spatial frequency of the surface irregularities yields interference patterns that couple with the material and grow in size until it reaches an optimal condition, in which other initial irregularities are washed out and periodic structures are formed.[12] The induction of the periodic structures by self-organized light can have distinct origins such as thermal (e.g., melting, phase transitions, recrystallization, and vaporization), saturable absorption and mass movement, plasma formation, surface chemical changes, refractive index changes, photodegradation, and photoetching.[1, 6, 12, 14]

In this chapter, the self-organization of LIPSS was investigated on two types of surfaces: a bare glass and a plasmonic substrate. These substrates were immersed in a solution containing diazonium salts and irradiated with a single laser beam. Photochemical and plasmon-mediated reactions appear to direct the structure formation in specific fashions.

The possible mechanisms for the reduction of the diazonium salts with metallic nanostructures have been reported, highlighting the role of the shape and the optical properties of the structures. In particular, it was shown that diazonium salts polymerize in polyaryl films predominantly through a radical process in the area where the induction of hot electrons is maximized.[15] In this work, we investigated the formation of a ripple structure at the interface of glass and diazonium salt-containing solution. We further modified the substrate by introducing plasmonically active gold nanoprisms produced by nanosphere lithography (NSL). In this paper, we highlight the difference in the formation of these ripple structures on bare glass and plasmonic substrates.

6.2 Experimental

The following methods were used throughout this chapter:

- Nanosphere Lithography (NSL), as described in Chapter 3, section 3.1
- Single Beam Induced Surface Gratings and Diazonium Salt Grafting, as described in Chapter 3, section 3.6
- Finite-Difference Time-Domain (FDTD) modelling, as described in Chapter 3, section 3.2.1
- Scanning Electron Microscopy (SEM), as described in Chapter 3, section 3.3.1
- Atomic Force Microscopy (AFM): AFM scans were obtained using a BioScope Catalyst atomic force microscope (Bruker). Silicon tips (NCL-50, NanoWorld) with a force constant of 48 N/m and a resonance frequency of 190 kHz were used in tapping mode. Height images were recorded at a scan rate of 0.3 Hz to acquire sample topography. Image processing and extraction of cross-sections were performed using Gwyddion software.

6.3 Results and Discussion

The irradiation of the diazonium salt solution on a bare glass substrate results in the formation of ripples parallel to the direction of the polarization. This particular diazonium salt was chosen for its susceptibility to a dediazonation reaction upon irradiation. The cationic reaction of the diazonium salt in solution, which is commonly referred to as

spontaneous grafting, will result in aggregates of a polyaryl film, while the plasmon-mediated radical reaction will result in controlled growth of the polyaryl film, as shown in Figure 6-1.[15]

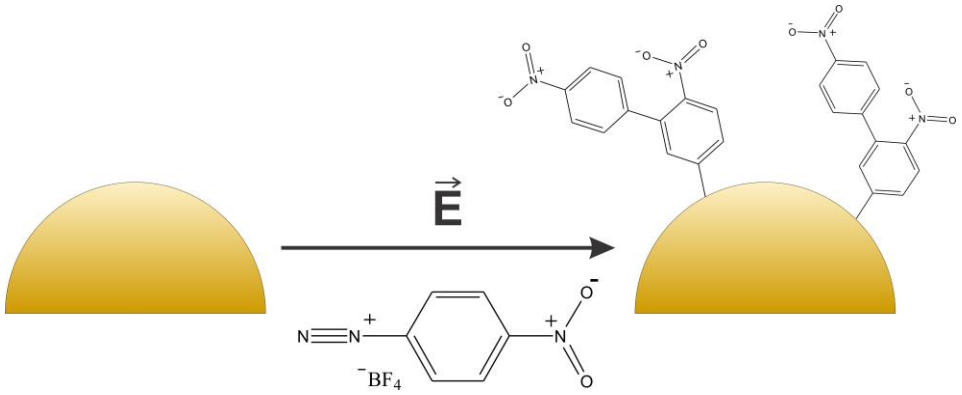

Figure 6-1 Scheme of the functionalization of a generic gold nanomaterial under plasmon excitation with light.

These aggregates can then adhere to the either the glass surface or the plasmonic gold nanomaterials. In this process, which can be induced by heat or light, the heterolytic dediazonation of the salt forms cations that react with one another, resulting in the formation of the initial polyaryl thin film (Figure 6-2a).[16-18] The SEM image of the polyaryl thin film (Figure 6-2a) was treated with color segmentation using Python for a higher contrast to highlight the difference between the polyaryl thin film (blue) and the bare glass (white).

The self-organized grating formation begins when the incident beam is scattered around nanoscale surface irregularities of the polyaryl thin film. The incident beam scattering causes a ripple-like interference pattern across the surface with high and low intensity areas.[14, 19] A longer irradiation time results in the enhanced formation of the periodic structures (Figure 6-2b). A similar process initiates the grating formation on the plasmonic substrates. The hot spots generated by the plasmonic nanostructures act as nucleation sites for the grating formation. The nucleation sites affect both the pitch and the pattern of the grating.

The grating pitch can be determined using the phase matching condition described by Equation [6-1]. When an electromagnetic wave is incident on an interface, Maxwell equations' boundary condition requires that the tangential component of the light be continuous (Figure 6-2b). The longitudinal vector component can then be derived using the dispersion relation shown in Equation [6-2].

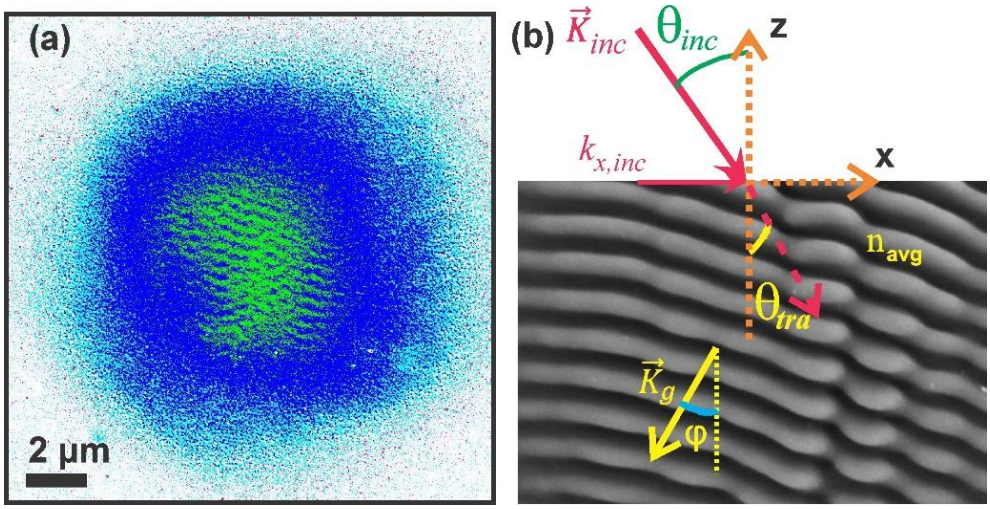

Figure 6-2 (a) A high contrast SEM image of the polyaryl thin film formation on glass substrate after 2 minutes of irradiation. (b) Schematic illustration of the grating k-vector and the light k-vector. The grating is fully formed after 8 minutes of irradiation.

Phase-matching condition:

$$\vec{k}_{tra,x} = \vec{k}_{inc,x} \pm m\vec{k}_{g,x} \quad [6\text{-}1]$$

Dispersion relation:

$$|\vec{k}_{tra,z}|^2 = |n_{avg}\vec{k}_{inc}|^2 - |\vec{k}_{tra,x}|^2 \quad [6\text{-}2]$$

Where n_{avg} is the refractive index just above the material interface, m is the diffraction order, $\mathbf{k}_{inc}$ is the incident light wavevector, $\mathbf{k}_{tra}$ is the light wavevector in the transmission region, and $\mathbf{k}_g$ is the grating wavevector. Considering Eqs 1-2, the grating periodicity Λ becomes equation [6-3]:

$$\Lambda = \frac{\pm m\lambda_{inc} \sin\varphi}{(n_{avg} \sin\theta_m - n_{inc} \sin\theta_{inc})} \quad [6\text{-}3]$$

Where θ_m is the diffraction angle, θ_{inc} is the incident angle, φ is the angle between the normal to plane and the grating vector, and λ_{inc} is the wavelength of incident radiation. For a grating with crests and troughs running perpendicular to electric field (grating vector parallel to the electric field $\varphi = 90^o$), the diffraction at grazing angle $\theta_m = 90^o$ and normal irradiation $\theta_{inc} = 0^o$, the equation can be simplified to:

$$\Lambda = \frac{\lambda}{n_{avg}} \quad [6\text{-}4]$$

6.3.1 Single-beam Inscriptions on Bare Glass

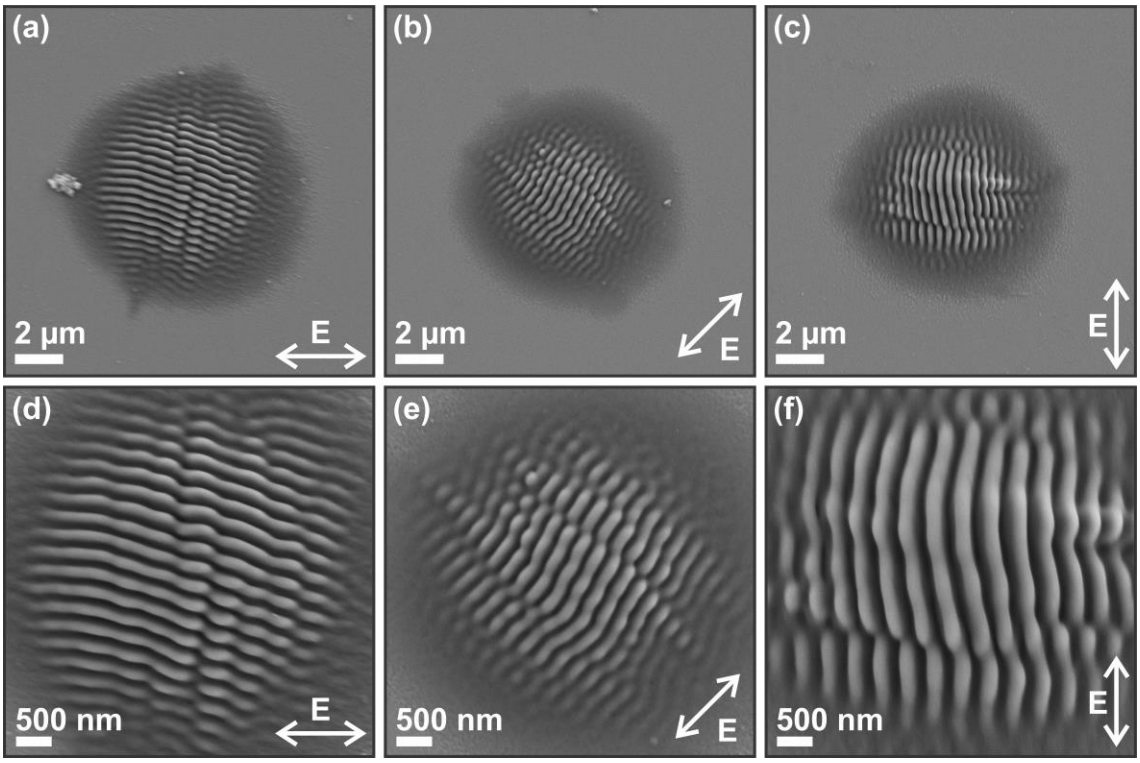

Figure 6-3 (a-c) SEM images of the gratings produced on glass with a polarization of 0°, 45°, and 90°, respectively. (d-f) Higher magnification images of (a-c), respectively. Patterns were obtained after an irradiance of 7.49×10^3 W/cm^2 for 8 minutes.

Three gratings were inscribed onto a bare glass substrate after 8 minutes of irradiation with distinct polarization orientations of the single beam (Figure 6-3). When the input polarization is rotated, the resulting grating orients accordingly. The formation of these gratings is dependent on incident intensity. The 20× microscope objective (N.A. = 0.5) was slightly defocused to increase the beam size at the sample plane. The resulting size of the laser beam was approximately 10 μm. For this defocused beam, the average irradiance across the surface is 7.49×10^3 W/cm^2, much lower than the irradiance corresponding to the focused beam spot (7.49×10^5 W/cm^2). The lower irradiance allowed by the defocused beam results in the formation of periodic ripple structures.

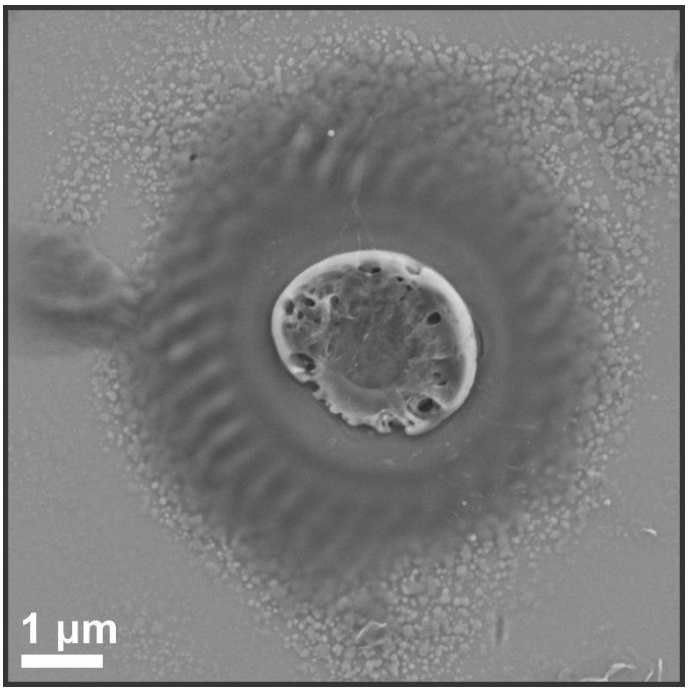

Figure 6-4 SEM image of the amorphous mass generated by the focused laser spot.

In contrast, with a focused beam, the ripples form only around the edges of the laser spot with an irregular structure in the center, as shown in Figure 6-4. Under high irradiance, there is not enough time for the self-organization process. Instead, material deformation occurs over the entire irradiated area, forming irregular structures. Under low irradiance, this surface deformation does not occur. The grating amplitude increases with increasing irradiation time. After 10 minutes of irradiation, more material accumulates, and the ripple structures begin to recombine due to lack of space. Using AFM, we determined

that the overall structure heights produced during the 8-minute irradiation were approximately 1.1 μm (Figure 6-5a-b) at its maximum and the periodicity at the center of the grating of 390±20 nm. Due to the gaussian nature of the laser, the grating structures produced further exhibit a gaussian profile (Figure 6-5b).

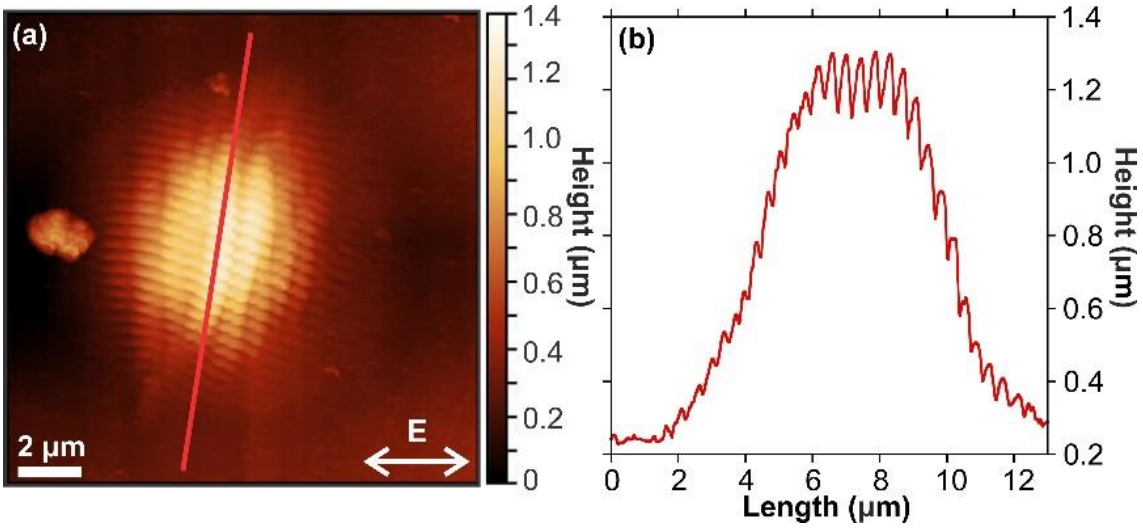

Figure 6-5 (a) AFM scan of the grating produced with a polarization of 0° (same structure as shown in Figure 6-2a. (b) Cross section of (a) as indicated in red.

To ascertain the absence of interference from reflection within the glass, the pitch of the LIPSS was measured on three glass substrates with thicknesses of 130, 600, and 1000 μm, as shown in Figure 6-6.

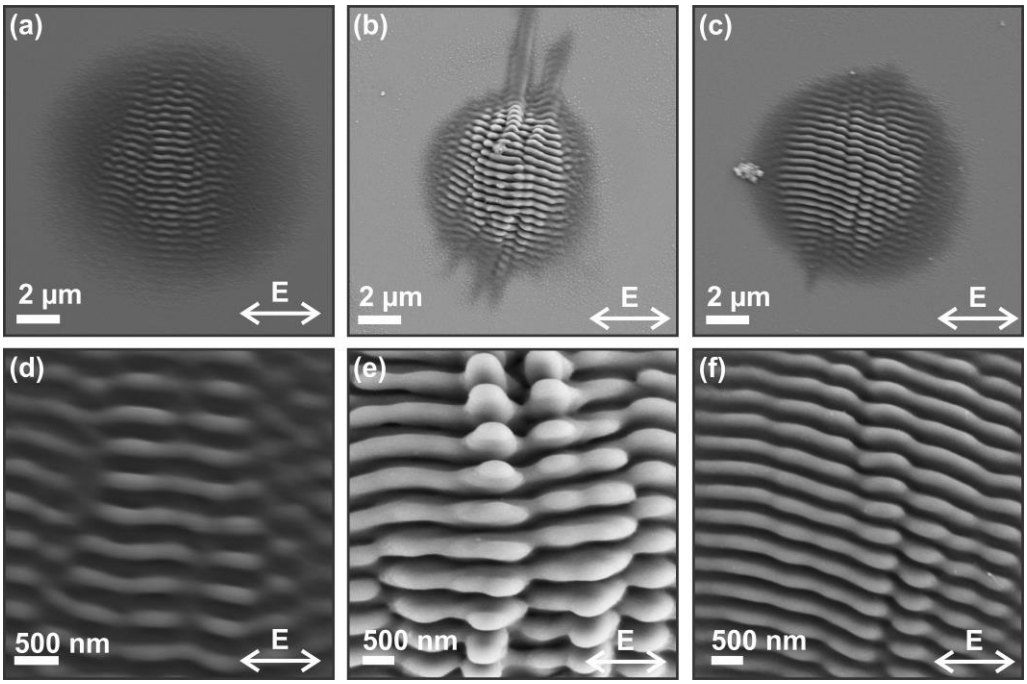

Figure 6-6 SEM images of three different substrate thicknesses: 160 µm (a and d), 600 µm (b and e) and 1000 µm (c and f).

The pitch of the grating on all three substrates were measured to be approximately 375 ± 10 nm. Therefore, we can conclude that the substrate thickness does not influence grating formation. Using equation 6-5, we can theoretically determine that a normal incident beam at the interface of the solution and substrate creates gratings with a pitch of 420 nm, where n_{avg} is 1.5. This differs from the experimental result by 10 %. This error can be explained by the fact the grating equation does not consider material response to the incident beam. Although the refractive index at the interface of the substrate is considered in the equation, the equation does not consider structure growth, which depend on the chemical and physical properties of the material. The intensity dependence of chemical reduction of the diazonium salt are key factors in the structure growth.

6.3.2 Single-Beam Inscriptions on Gold Nanoprisms

Plasmonic gold nanoprisms organized in a hexagonal geometry were produced using NSL to investigate directional control of the reduction of diazonium salts into a polyaryl layer. The plasmon resonance of the NSL substrates was determined to be approximately

640 nm (Figure 6-7a), matching the excitation wavelength of the laser (632.8 nm). This allows for the excitation of the localized surface plasmon resonance on the nanoprism surfaces. Plasmon resonances can be used to induce chemical reactions through several reaction pathways, including thermal and hot-carrier processes.[20, 21] In plasmon-mediated chemical reactions on nanostructures, grafting is dominated by a radical reaction since thermal effects dissipate very quickly in the solution.[22] In the radical reaction, hot electrons generated by light excitation are transferred from the gold structures to the diazonium cation, resulting in the formation of aryl radicals. These radicals react with the surface to form an aryl layer which continues to grow into a thin polymer film. The thickness of this polymer film varies with the irradiation conditions and local field enhancements. The formation of the polymer thin film is more efficient in the area where the field is maximum. This plasmon-mediated chemistry also eliminates the need for a catalyst to be present, indicating that the reactions are plasmon-induced.[23, 24] In Figure 6-7b, we show the plasmon-induced functionalization in the vicinity of gold nanoprisms upon irradiation at 632.8 nm.

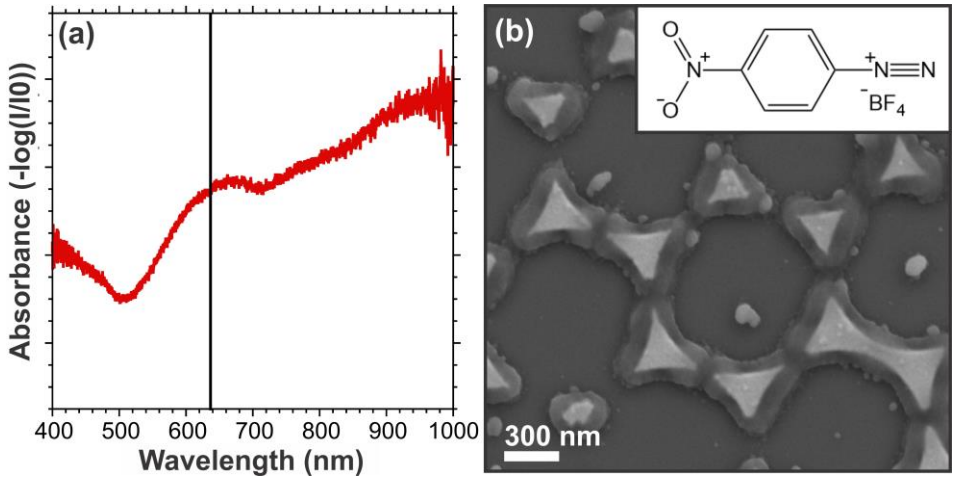

Figure 6-7 (a) Absorbance measurements of the NSL substrates with the 632.8 nm irradiation wavelength indicated by the black line. (b) An SEM image of the inset molecule grafted to the surface using a 632.8 nm laser after 3 minutes of irradiation with an irradiance of 7.49×10^3 W/cm^2.

The diazonium salt appears to form a polyaryl layer coating around the individual gold nanostructures. Noticeably, when two triangles are facing each other, the small gap

between the triangle where the field is the most concentrated further enhance the photoinduced grafting with larger amounts of grafted material.

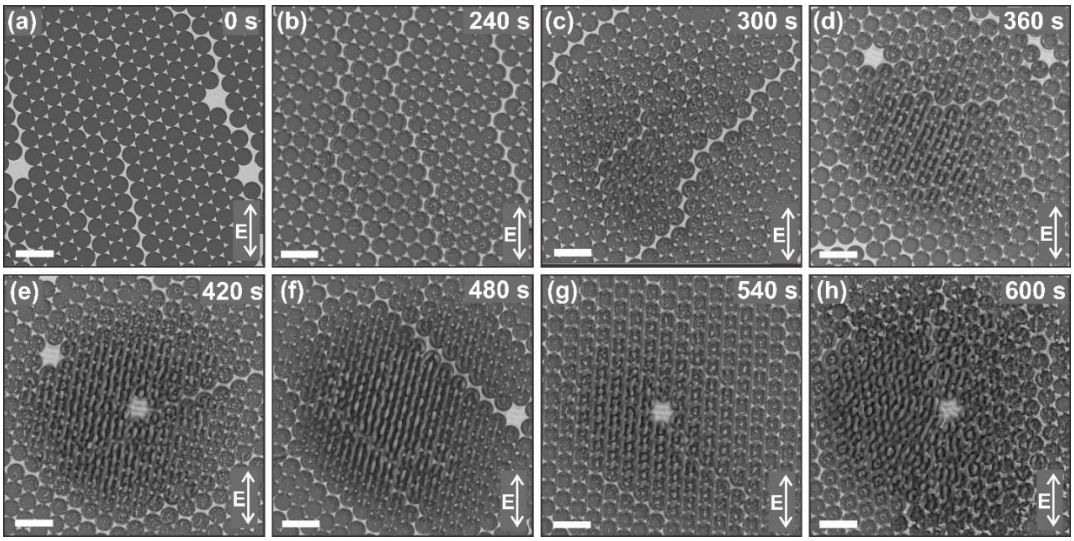

Figure 6-8 SEM images of the grating produced on an NSL substrate for different irradiation times, as indicated in the top right of each panel. The scale bar is 2 µm.

As the irradiation time of diazonium salt-containing solution on the NSL structures increases, self-organized gratings emerge (Figure 6-8). After 4 minutes of irradiation, the diazonium salt grafting to the surface is noticeable (Figure 6-8b) compared to the non-irradiated section (Figure 6-8a). After 5 minutes of irradiation, an even larger grafting amount is visible (Figure 6-8c). A wider grating pitch of roughly 455 ± 10 nm compared to 375 nm on a glass substrate is observed after 6 minutes of irradiation (Figure 6-8d). While the gratings along the edges of the nanoprisms form more quickly, the ridges between the structures take longer to form. This is highlighted in Figure 6-8d, where prominent grating line alternates with a line of smaller amplitude. For longer irradiation times, the grating produced becomes more uniform (Figure 6-8f, g). The accumulation of material away from the nanoprisms after 10 minutes of irradiation seems to influence the structure pattern resulting in a loss of order (Figure 6-8h).

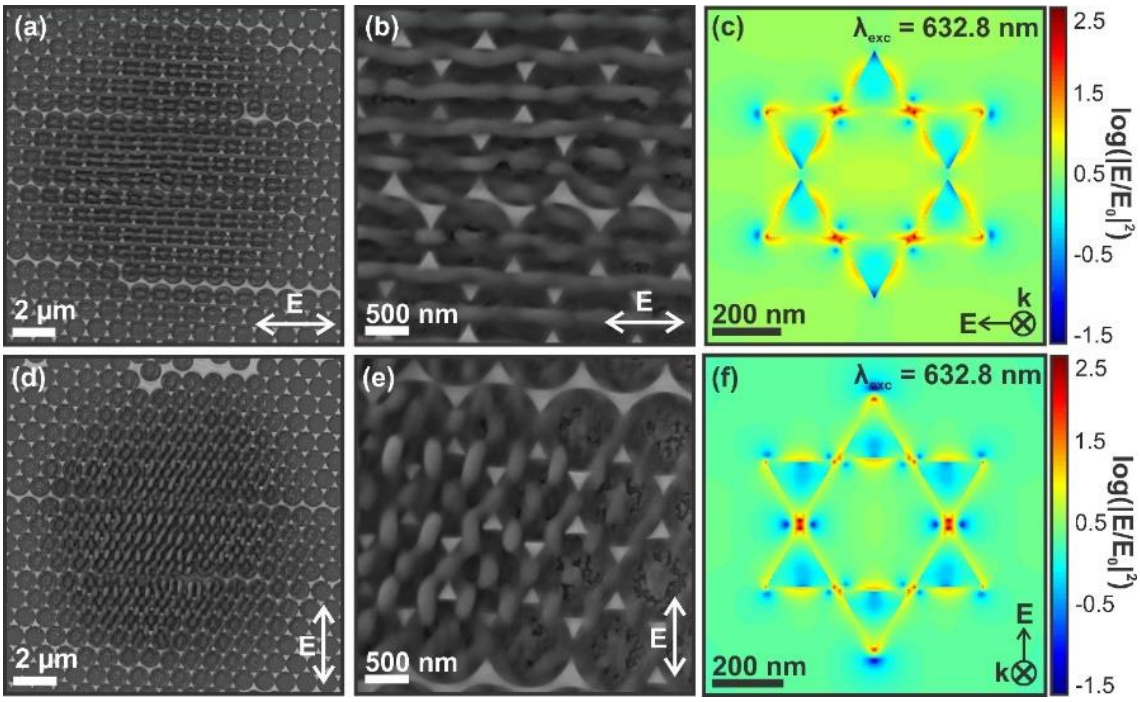

Figure 6-9 SEM images and FDTD calculations for grafting on an NSL substrate for horizontal (a-c) and vertical (d-f) polarizations.

The spatial distribution of the electromagnetic enhancement was investigated using FDTD modelling to follow the grating growth and evaluate the polarization dependence (Figure 6-9c, f). Gratings were inscribed using horizontal (Figure 6-9a-c) and vertical polarizations (Figure 6-9d-f). When the polarization of the excitation source is along the base of the nanoprisms (Figure 6-9c), the coupling between the plasmons at the apices of the adjacent nanoprisms is efficient and forms a series of aligned hotspots. When the input polarization is oriented along the height of the nanoprisms, two main hot spots can be observed at the junction between nanoprisms (Figure 6-9f), and the center of the hexagonal lattice does not show any significant enhancement. In both cases, an enhancement of the electric field is observed, and a significantly higher enhancement factor is present at the apices of the triangles. These plasmon resonances can be used as guides to effectively direct plasmon-mediated chemical reactions in the vicinity of the metallic nanotriangles, and to even modify the pitch of the self-organized ripples.

When the polarization is aligned with the bases of the triangles (Figure 6-9a, b), the ripple structures are fully formed with a wider pitch as compared with bare substrate due

to the alignment of the structures with the direction of plasmon-guided reactions. The electric field enhancement from the nanoprisms directs the pitch of the gratings. When the electric field enhancement is aligned along the base of the triangles, the nanoprisms perturbate the nucleation of the gratings by acting as a barrier and disturb the initial process of the interference pattern formation. However, when the polarization is aligned along the height of a triangle, a crisscross pattern is observed (Figure 6-9d, e). The coupling between the plasmon resonances of the nanoprism apices acts as a physical guide to the reduction of the diazonium salts to the substrate surface. In a polarization configuration perpendicular to the triangle bases, the nucleation for the grating deviates from straight lines to a crisscross pattern. At the center of the lattices, the self-organization process follows the polarization direction in a similar fashion as on bare glass substrate. At the junction between nanoprisms, the hotspot generations perturbate the self-organization process and induce a different direction for grating formation.

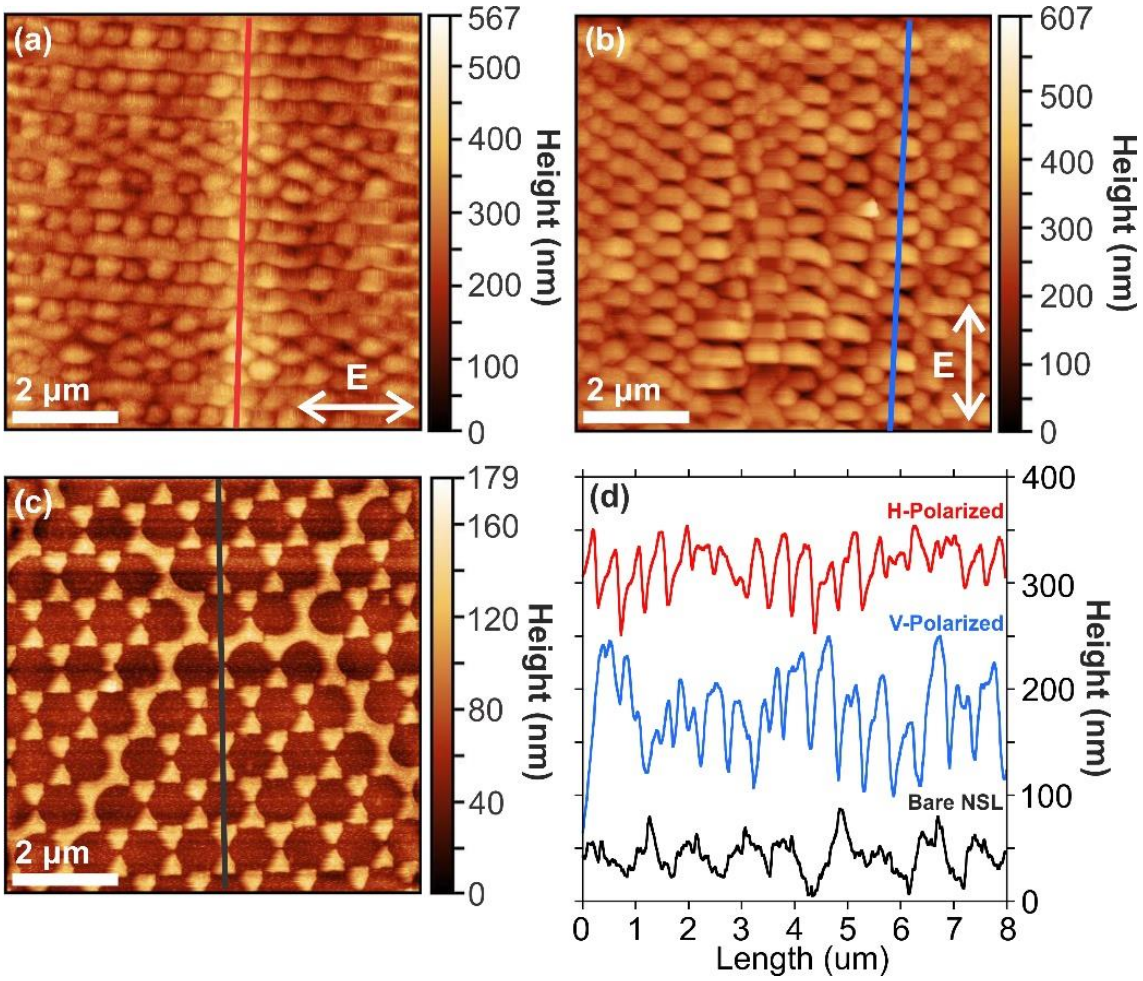

Figure 6-10 AFM scans of the grafting produced on the NSL substrates using (a) a horizontally polarized laser and (b) a vertically polarized laser, as well as (c) the bare NSL substrate. (d) The cross sections for (a), (b), and (c) are shown in red, blue, and black, respectively. The cross sections have been shifted in the y-axis for clarity.

The height profiles of the gratings produced on the NSL were obtained using AFM (Figure 6-10d). The grafting on both the horizontally- (Figure 6-10a) and vertically-polarized (Figure 6-10b) irradiated substrates show a height roughly 100 nm higher than the bare nanoprisms (Figure 6-10c). This indicates that the accumulated material that comprises the polyaryl film is roughly 100 nm in height. Furthermore, the gratings produced with both polarizations no longer show a Gaussian profile. This further indicates that the nanoprisms actively direct the grafting occurring at the surface.

This simple self-developing and polarization-dependent procedure makes these single beam structures possible candidates for a variety of photonic applications. The process of self-organization on solids and in liquids can be used for polarization sensitive devices.[25] Furthermore, the sensitivity of the self-organized gratings on plasmonic substrates make them interesting candidates for plasmonic sensors.[23, 26] The self-organized grafting of the diazonium salt on the nanoprisms demonstrates the effectiveness of plasmon-mediated chemistry to trigger spatially controlled and polarization-dependent surface reactions.[27-29] This process can potentially be used to graft molecules with distinct chemical functions into periodic gratings over nanostructures at specific wavelengths.

6.4 Conclusion

Herein, we report grafting and self-organized grating formation triggered by plasmon-mediated reduction of a diazonium salt. Irradiation of the diazonium salt solution on NSL structures initially results in homogenous grafting around the nanoprisms. Longer irradiation times facilitate the self-organization of periodic ripples. The ripple structures on a bare glass substrate follow a self-organization process. The pitch of the ripples follows the grating equation derived with the incident laser wavelength and the refractive index of the diazonium salt solution at the interface with the glass. In the presence of metallic nanostructures, localized field enhancement at the apices of the triangles disturb the initial growth of the self-organized interference pattern, resulting in the chemical reduction of diazonium salts into polyaryl layers. When the polarization is aligned with the triangle bases ripples form with a larger periodicity compared to those on the glass substrates. When the polarization is aligned perpendicular to the triangle bases, a crisscross pattern is instead formed. More complex metallic structures could be fabricated by more sophisticated nanolithographic techniques such as electron beam lithography to further investigate plasmon-mediated patterning. Additionally, other wavelengths and distinct polarization states can be explored, opening the possibility of multiplexing polymers onto nanostructures using light with moderate intensity.

6.5 References

1. Siegman, A.; Fauchet, P., *IEEE J. Quant. Electron.* **1986,** *22*, 1384-1403.

2. Bonse, J.; Krüger, J.; Höhm, S.; Rosenfeld, A., *J. Laser Appl.* **2012,** *24*, 042006.

3. Bonse, J.; Höhm, S.; Kirner, S. V.; Rosenfeld, A.; Krüger, J., *IEEE J. Sel. Top. Quantum Electron.* **2017,** *23*, 9000615.

4. Hong, L.; Rusli; Wang, X. C.; Zheng, H. Y.; Wang, H.; Yu, H. Y., *Appl. Surf. Sci.* **2014,** *297*, 134-138.

5. Zhang, H.; Colombier, J.-P.; Witte, S., *Phys. Rev. B* **2020,** *101*, 245430.

6. Sipe, J.; Young, J. F.; Preston, J.; Van Driel, H., *Phys. Rev. B* **1983,** *27*, 1141.

7. Elson, J.; Ritchie, K., *Phys. Status Solidi B* **1974,** *62*, 461-468.

8. Rudenko, A.; Mauclair, C.; Garrelie, F.; Stoian, R.; Colombier, J.-P., *Nanophotonics* **2019,** *8*, 459-465.

9. Fuentes-Edfuf, Y.; Sánchez-Gil, J. A.; Florian, C.; Giannini, V.; Solis, J.; Siegel, J., *ACS Omega* **2019,** *4*, 6939-6946.

10. He, X.; Datta, A.; Nam, W.; Traverso, L. M.; Xu, X., *Sci. Rep.* **2016,** *6*, 35035.

11. Buividas, R.; Mikutis, M.; Juodkazis, S., *Prog. Quant. Electron.* **2014,** *38*, 119-156.

12. Mazaheri, L.; Sabat, R. G.; Lebel, O.; Nunzi, J.-M., *Opt. Mater.* **2016,** *62*, 378-391.

13. Leblond, H.; Barille, R.; Ahmadi-Kandjani, S.; Nunzi, J.-M.; Ortyl, E.; Kucharski, S., *J. Phys. B-At. Mol. Opt.* **2009,** *42*, 205401.

14. Bonse, J.; Gräf, S., *Laser Photonics Rev.* **2020,** *14*, 2000215.

15. Tijunelyte, I.; Kherbouche, I.; Gam-Derouich, S.; Nguyen, M.; Lidgi-Guigi, N.; Lamy de la Chapelle, M.; A., L.; Levi, G.; Aubard, J.; Chevillot-Biraud, A.; Mangeney, C.; Felidj, N., *Nanoscale Horiz.* **2018,** *3*, 53-57.

16. Pinson, J.; Podvorica, F., *Chem. Soc. Rev.* **2005,** *34*, 429-439.

17. Mesnage, A.; Lefèvre, X.; Jégou, P.; Deniau, G.; Palacin, S., *Langmuir* **2012,** *28*, 11767-11778.

18. Jayasundara, D. R.; Cullen, R. J.; Colavita, P. E., *Chem. Mater.* **2013,** *25*, 1144-1152.

19. Rudenko, A.; Colombier, J.-P.; Höhm, S.; Rosenfeld, A.; Krüger, J.; Bonse, J.; Itina, T. E., *Sci. Rep.* **2017,** *7*, 1-14.

20. Baffou, G.; Bordacchini, I.; Baldi, A.; Quidant, R., *Light Sci. Appl.* **2020,** *9*, 108.

21. Mesnage, A.; Lefèvre, X.; Jégou, P.; Deniau, G.; Palacin, S., *Langmuir* **2012,** *28*, 11767-11778.

22. Guselnikova, O.; Postnikov, P.; Chehimi, M. M.; Kalachyovaa, Y.; Svorcik, V.; Lyutakov, O., *Langmuir* **2019,** *35*, 2023-2032.

23. Nguyen, V.-Q.; Ai, Y.; Martin, P.; Lacroix, J.-C., *ACS Omega* **2017,** *2*, 1947-1955.

24. Busson, M.; Berisha, A.; Combellas, C.; Kanoufi, F.; Pinson, J., *Chem. Commun.* **2011,** *47*, 12631-12633.

25. Chen, R.; Lee, Y. H.; Zhan, T.; Yin, K.; An, Z.; Wu, S. T., *Adv. Opt. Mater.* **2019,** *7*, 1900101.

26. Nair, S.; Escobedo, C.; Sabat, R. G., *ACS Sensors* **2017,** *2*, 379-385.

27. Nguyen, M.; Tijunelyte, I.; de la Chapelle, M. L.; Mangeney, C.; Felidj, N., Plasmon-driven surface functionalization of gold nanoparticles. In *Plasmonics in Chemistry and Biology*, 1st ed.; de la Chapelle, M. L.; Felidj, N., Eds. Jenny Stanford Publishing: New York, 2019; pp 1-32.

28. Kherbouche, I.; Luo, Y.; Felidj, N.; Mangeney, C., *Chem. Mater.* **2020,** *32*, 5442–5454.

29. Luo, Y.; Xiao, Y.; Onidas, D.; Iannazzo, L.; Etheve-Quelquejeu, M.; Lamouri, A.; Félidj, N.; Mahouche, S.; Brulé, T.; Eilstein, N.; Gazeau, F.; Mangeney, C., *Chem. Commun.* **2020,** *56*, 6822-6825.

Chapter 7

7 Three-Color Plasmon-Mediated Reduction of Diazonium Salts over Metasurfaces.

(A version of this work has been published in the journal *Nanoscale Advances*: Therien, D.A.B.; McRae, D.M.; Mangeney, C..; Félidj, N.; Lagugné-Labarthet, F. *Nanoscale Adv.*, **2021**, *3*, 2501-2507.)

Surface plasmon-mediated chemical reactions are of great interest for a variety of applications ranging from micro- and nanoscale device fabrication to chemical reactions of societal interest for hydrogen production or carbon reduction. In this chapter, a crosshair-like nanostructure is investigated for its ability to induce local enhancement of the local electromagnetic field at three distinct wavelengths corresponding to three plasmon resonances. The structures are irradiated in presence of a solution containing diazonium salts at wavelengths that match the resonance positions at 532 nm, 632.8 nm, and 800 nm. The resulting grafting shows polarization and wavelength-dependent growth patterns at the nanoscale. The plasmon-mediated reactions over arrays of the crosshair structures are further investigated using scanning electron microscopy and supported by finite domain time domain modelling revealing the wavelength and polarization specific reactions. Such approach enables nanoscale molecular printing using light source opening multiplexing applications where different analytes can be grafted under distinct opto-geometric conditions.

7.1 Introduction

Excitation of localized surface plasmon resonances (LSPRs) is an effective method for enhancing the local optical fields which can in turn be used for a variety of applications such as in enhanced spectroscopies and plasmonic sensing where both sensitivity and spatial resolution can be drastically improved through a plasmon effect.[1-4] In discrete nanostructures, LSPRs are generally spatially confined in specific areas and can be excited with selected set of wavelength and polarization of the impinging field. In ideal opto-geometric configuration, the electric field is typically enhanced by a 10-100 fold factor which is enough to yield large enhancement factors and which can in turn be used

for a variety of sensing applications through surface enhanced mechanisms in Raman,[2, 3, 5-7] infrared,[8-10] fluorescence,[11-14] and nonlinear optical measurements.[15-18]

This spatial confinement can also be used to promote chemical reactions through the generation and ejection of hot electrons.[19] Metallic nanomaterials that contain LSPRs have shown a wide applicability for plasmon-mediated reactions.[20-22] Such reactions include chain-linking of gold nanoparticles,[23] fabrication of biosensors,[24] plasmon mediated drilling,[22] and performing surface chemistry such as CO_2 reduction,[25-27] water splitting for hydrogen production,[28-30] single oxygen production,[14] and artificial photosynthesis.[31] Multiplexed functionalization is of particular interest when several analytes can be spatially grafted over metallic structures solely using light irradiation. Such reactions have been studied on gold nanodisks by grafting both a carboxyphenyl diazonium salt and a hydroxyethyl phenyl diazonium salt to a single surface using orthogonal irradiation polarizations.[32] A polymer formulation containing two different light-emitting quantum dots was grafted to the surface of a nanomaterial at two different polarizations, highlighting the possibility to graft quantum dots in orthogonal directions keeping at a nanoscale resolution.[33] Other plasmon-mediated reactions includes local polymerization in the vicinity of the metallic nanostructures and temperature-responsive gold/polymer hybrid structures.[34, 35] Such light-induced nanoscale printing opens many perspectives in device fabrication. The main limitation in multi-analyte functionalization is the number of plasmon resonances that can be tackled independently with different wavelengths. A nanostructure with n discrete resonances will theoretically open the possibility to use n wavelengths of irradiation. Each resonance being associated with a unique spatial pattern of the electromagnetic confinement will subsequently yield a defined pattern upon irradiation with the matching wavelength. Such structures with multiple resonances have been demonstrated in fractal structures with resonances ranging from the visible to the mid-infrared and highlighting the hybridization between the successive fractal generations.[3, 21]

In this chapter, arrays of gold metastructures with crosshair geometries and that display three resonances in the visible range are studied. This crosshair structure was developed to introduce a metamaterial containing multiple exploitable plasmon resonances in the

visible to near-infrared spectral range. It combines the longitudinal plasmon modes of nanorods as repeating features on a longer branch, as well as the transverse mode arising from the width of both the features and the overall branches. The nanostructures were made by electron beam lithography and displays three resonances centered around 532, 632 and 785 nm. Specifically, the spatial grafting of 4-nitrobenzenediazonium tetrafluoroborate was investigated and has shown excellent reactivity when subject to light irradiation in the vicinity of metallic nanostructures and form a thin polymer film that can be readily observed by electron microscopy.

7.2 Materials and Methods

The following methods were used throughout this chapter:

- Finite Domain Time Domain (FDTD) modelling, as described in Chapter 3, section 3.1
- Electron Beam lithography (EBL), as described in Chapter 3, section 3.2.2
- Diazonium salt grafting, as described in Chapter 3, section 3.6
- Scanning Electron Microscopy (SEM), as described in Chapter 3, section 3.3.1

7.3 Results and Discussion

7.3.1 FDTD Modelling

Crosshair-like nanostructures, dendrimer-like structures with C4 symmetry, were first designed and simulated using FDTD calculations, allowing their plasmon resonances to be fine-tuned prior to fabrication.

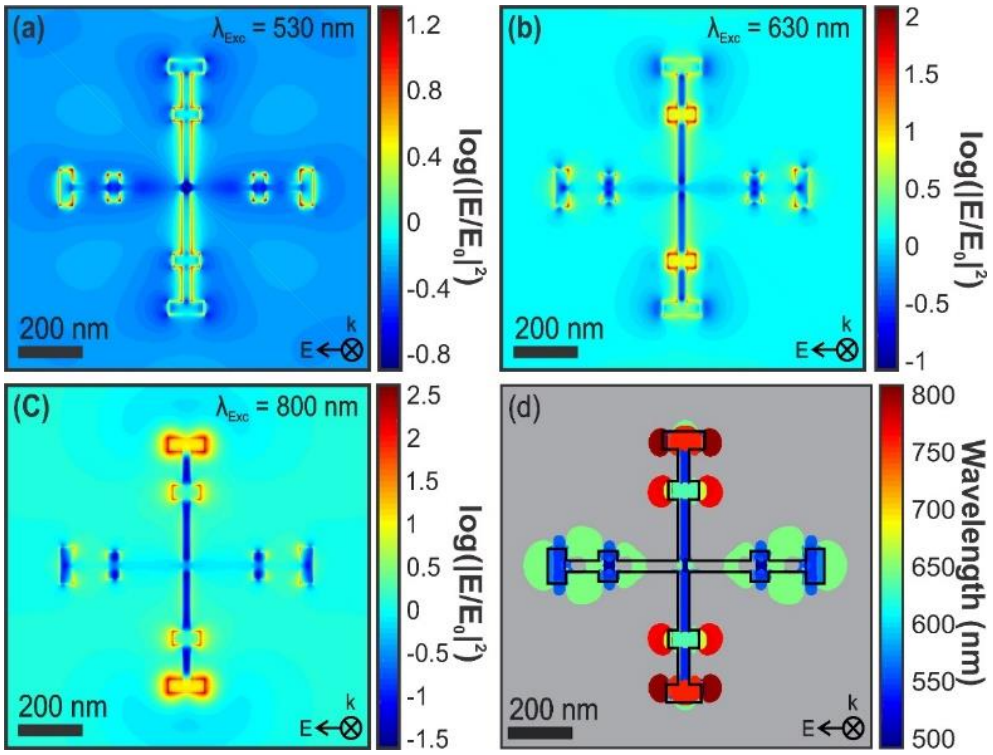

Figure 7-1 Distribution of the near-field at 530 nm (a), 630 nm (b) and 800 nm (c) for a horizontal polarization. The corresponding isowavelength map is shown in (d) and represent the spatial distribution of the field for wavelengths varying from 500 nm to 800 nm with a crosshair structure outlined in black.

The near-field distribution of the EM field around the structure has been calculated at 530 nm, 630 nm and 800 nm for a horizontal polarization over the crosshair structures that are composed of orthogonal major rods with length of 800 nm and with two minor rod across each arm of the structure. Irradiation at 530 nm (Figure 7-1a) shows confinement of the field along all rods, major and minor, that are orthogonal to the polarization. At 630 nm (Figure 7-1b), the two minor rods located in the middle of the branch orthogonal to the input polarization display field confinement while at 800 nm (Figure 7-1c) the two minor rods located at the extremity of the branch on the arms perpendicular to the polarization direction concentrate the field the most. The isowavelength map shown in Figure 7-1d provides a snapshot of the different zones where the field is locally enhanced for the three selected wavelengths. The dark blue, green and red colors indicate the field confinement at 532 nm, 632 nm and 800 nm, respectively. The structure being isotropic with a C_4

symmetry axis, a rotation of the polarization by 90° will rotate the distribution pattern accordingly.

7.3.2 Characterization and Functionalization

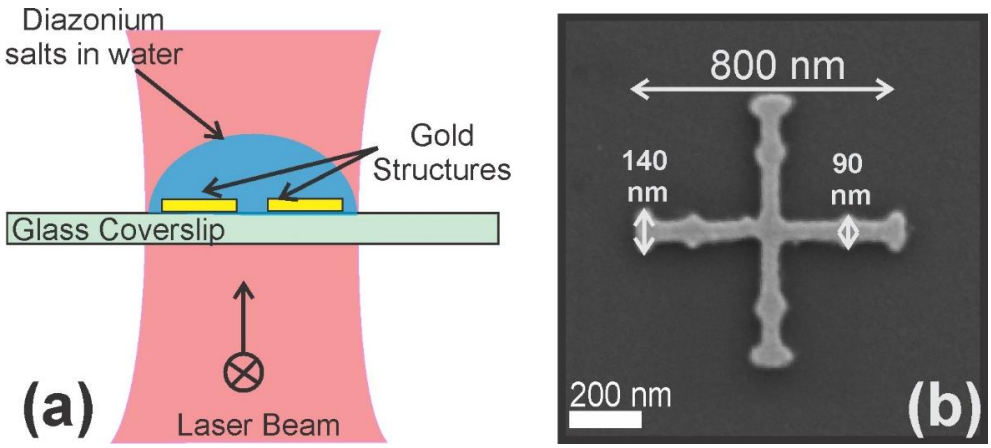

Figure 7-2 (a) Depiction of a grafting experiment. (b) SEM image of an individual structure.

Two distinct optical setups were used to investigate the three LSPRs. An 800 nm femtosecond-pulsed laser is used to irradiate a single structure at a time without burning or destroying them. This setup also uses a piezoelectric nanopositioning stage combined with a 100× objective (N.A.=0.95). This combination allows the 1 μm laser spot to be precisely positioned onto a single structure at a time. The CW lasers at 532 nm and 632.8 nm were coupled to a distinct setup that uses a 20x objective (N.A.=0.5) that is slightly defocused producing a spot size of approximately 8 μm and irradiating multiple structures at the same time. While this setup has the advantage of irradiating many structures at once, the Gaussian nature of the beam produces varying results from the center of the spot towards the edge, which will be discussed further. A typical irradiation experiment is shown in Figure 7-2a together with a single nanostructure produced by electron-beam lithography (Figure 7-2b).

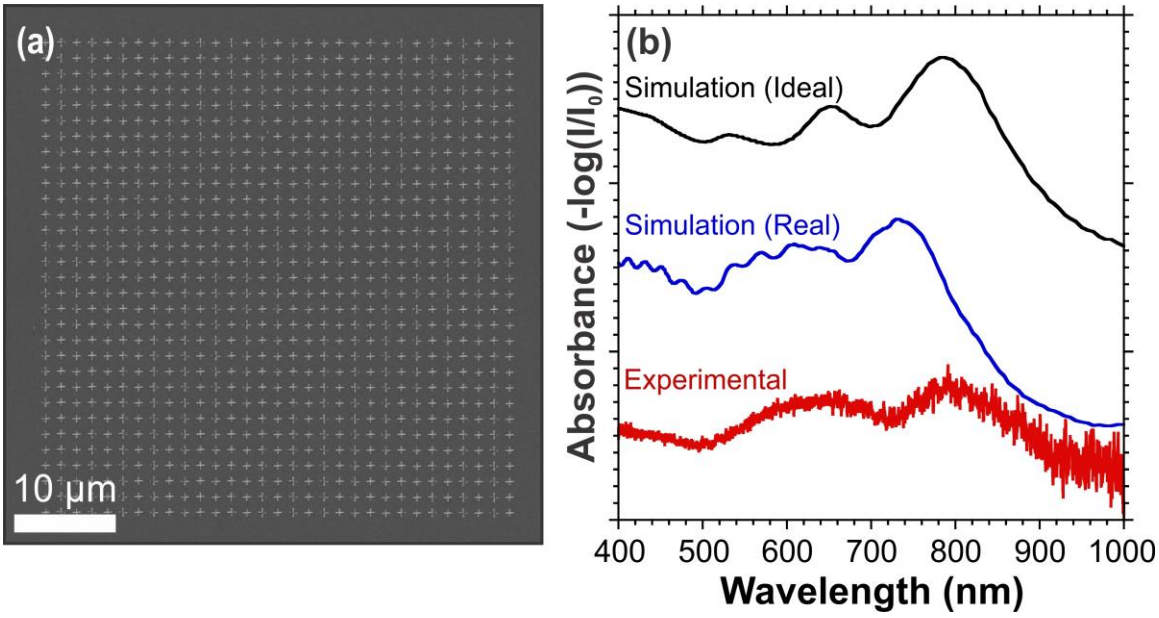

Figure 7-3 (a) Representative SEM image of an array of dendrimers used for grafting with a single structure shown in the inset. (b) FDTD far-field scattering for ideal (defect-free) and real structures (as shown in Figure 7-1b) and experimental absorption measurements for a linearly polarized light oriented horizontally or vertically with respect to the structure axes.

Using electron beam lithography, arrays of structures were produced in (50×50) μm^2 patches, as shown in Figure 7-3a. The individual crosshairs major axes measure 800 nm in length with 90 nm and 140 nm minor notches oriented perpendicularly to the longer branches (Figure 7-2b). Three broad plasmon resonances can be identified in the far-field FDTD modelling at central wavelengths of 530 nm, 630 nm, and 800 nm (Figure 7-3b). The experimental extinction spectrum only shows 2 resonances including a broader one centered at 610 nm that shows a shoulder around 550 nm.

7.3.3 Irradiation at 800 nm

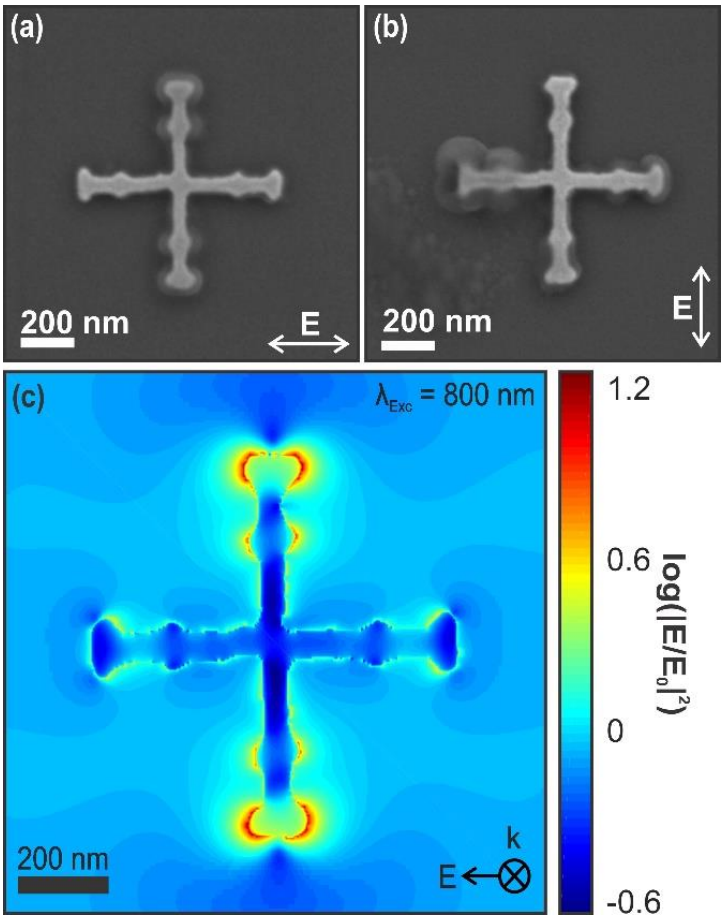

Figure 7-4 SEM images of the dendrimers after irradiation under an 800 nm fs-pulsed laser, for both (a) horizontally and (b) vertically polarized light. (c) FDTD modelling of the near-field distribution upon irradiation at 800 nm for the real structure with a horizontal polarization.

The crosshair structures were first irradiated at 800 nm for 60 seconds under a power of 10 mW. The material grafted is composed of a thin film formed from 4-nitrobenzenediazonium tetrafluoroborate,[36] through either a cationic or a radical plasmon-induced polymerization pathway.[37] Briefly, in the cationic process, heating in room temperature conditions or light-induced decomposition of the solution-containing salt induces the formation of cations by heterolytic dediazoniation that react with gold surfaces. Other aryl cations present in solution further react with the first grafted groups forming polyaryl layer on the surface.[38] This cation-induced reaction is generally referred

as a spontaneous grafting and may lead to the formation of monolayer at the surface of the substrate.[37, 39] In the radical process, plasmon-induced electron transfers from the gold structures to the diazonium cation yield the formation of aryl radicals that in turn react with the surface to form an aryl molecular layer. Other radicals react with the first layer to form a thin polymer film which thickness varies with the irradiation conditions and local field enhancements. Both mechanisms presumably yield the formation of polymer thin films in the area where the field is maximum. However, local heating effect from a cationic process will dissipate very quickly in the solution and because of the good thermal conductivity of the gold structures, the grafting will be more homogeneous over the surface of the structure. Additionally, the light decomposition of the salts occurs predominantly in the ultra-violet range and should be limited upon exposure at 800 nm. The grafting at 800 nm should essentially be driven by a radical mechanism. Shown in Figures 7-4a,b are the SEM images after irradiation at λ=800 nm with a horizontal and vertical polarization, respectively. The polarization dependence is the most apparent here, where the orthogonal irradiations produced similar grafting patterns rotated by 90°. These experimental results can be compared to the FDTD calculations shown in Figure 7-1c and Figure 7-4c for ideal and real structures, respectively. The plasmon-induced grafting of the diazonium salts is predominantly localized around the two minor notches on the perpendicular branch with respect to the input polarization. While the irradiance is higher on the 800 nm setup (by a factor of 100 – 1000), the femtosecond pulses allow the structures to be irradiated without burning or melting them.

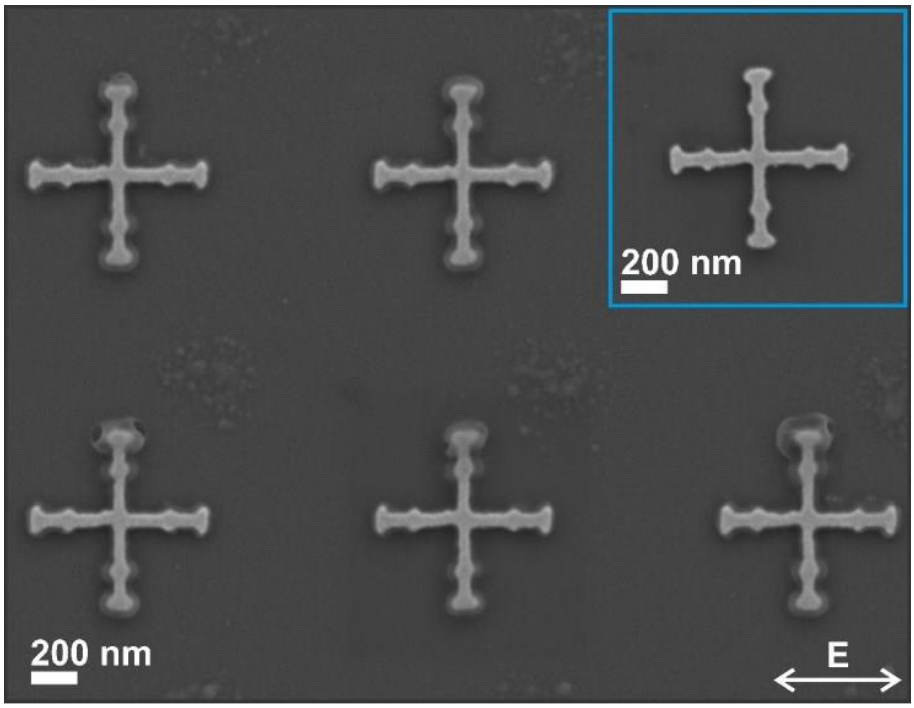

Figure 7-5 A representative array of five structures, each individually irradiated under an 800 nm fs-pulsed laser with a horizontal polarization in the presence of the diazonium-containing solution. In this experiment, the 800 nm laser beam is focused to 1 micron and the sample is scanned using a piezo electric stage. Each structure is irradiated for 60s with the beam centered over the structure. The inset (blue box) shows a structure immersed in the same diazonium-containing solution but without any exposure to laser irradiation.

The same localized molecular patterning can be done over an array of structures irradiated in similar conditions, as shown in Figure 7-5, highlighting the reproducibility and homogeneity of the plasmon-induced reaction. Furthermore, as shown in the inset of Figure 7-5 with a reference structure immersed with the same solution but without any laser irradiation, this experiment indicates that there is no evidence of spontaneous grafting at the surface of the crosshairs and that the grafting is only plasmon-driven, as expected.

7.3.4 Irradiation at 632.8 nm

Similar structures were irradiated with a continuous-wave laser at 632.8 nm with a spot size of approximately 8 μm in diameter. A manual control stage was used, allowing for the irradiation of multiple structures at a time. This led to some variety in the grafting development based on the energy dose that each structure received relative to its position in the laser spot.

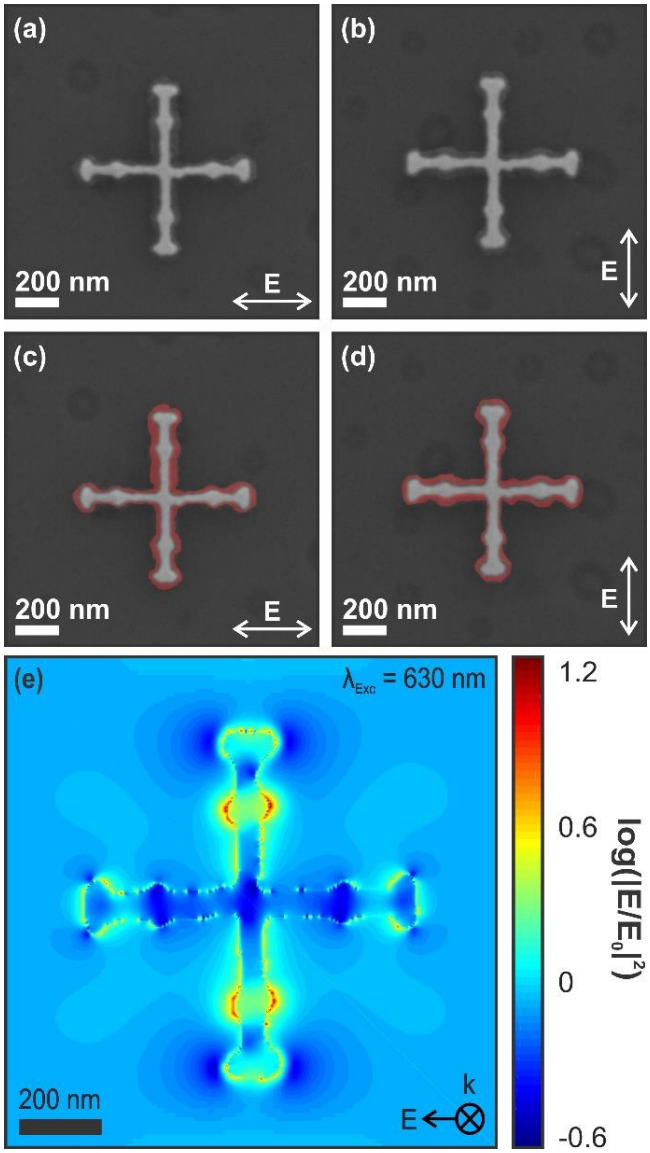

Figure 7-6 SEM images of the structures after irradiation under a 632.8 nm continuous-wave laser, for both (a) horizontally and (b) vertically polarized light. (c,d) represents the same images but colorized in red to highlight the areas on which

grafting mainly occurred. (e) FDTD modelling of the near-field distribution upon irradiation at 630 nm for the real structure with a horizontal polarization.

Shown in Figures 7-6a,b are the polarization dependent grafting spatial distributions for both horizontally (Figure 7-6a) and vertically (Figure 7-6b) polarized fields. The grafted material has been colorized for the corresponding polarizations in Figure 7-6c,d. Remarkably, the grafting occurs on both axes. However, the major axis orthogonal to the input polarization show the thicker grafting. This is again in agreement with the FDTD calculation of Figure 7-1b for the ideal and real structures and Figure 7-6e for the real structure where both major axes show areas of large confinement yet with larger confinement on the axes orthogonal to the input polarization. In order to estimate the effect of the irradiation power over the grafting, functionalized areas were imaged at the center of the beam and in the outer edge of the Gaussian beam.

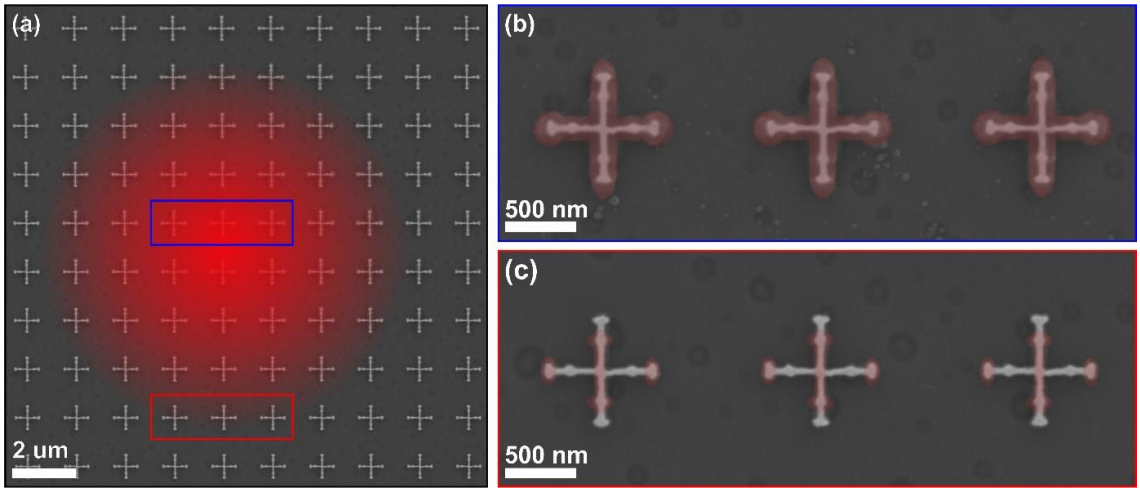

Figure 7-7 (a) an SEM image of an array of crosshairs irradiates at 632.8 nm in the presence of diazonium salts. The blue box is near the center of the beam and the red box is near the edge. The difference in grafting is shown in more detail in (b) and (c).

At the center of the 632.8 nm beam (Figure 7-7a,b) the grafting is homogeneous over the whole structure and it is difficult to differentiate the areas with different field enhancements. In contrast, Figure 7-7a,c corresponds to the area at the edge of the 632.8 nm Gaussian beam, the functionalization is partial and shows grafting along the

orthogonal axis up to the first notch and around the larger notch of the axis parallel to the input polarization, in good agreement with Figure 7-1b. This indicates that the threshold for plasmon-mediated grafting is relatively low. By fine tuning the energy density at the surface, the amount of material grafted can be controlled. This can be achieved by either reducing the irradiation time or the irradiance.

7.3.5 Irradiation at 532 nm

Finally, the last experiment was done with an irradiation at 532 nm, a wavelength for which FDTD predicts a third but weaker resonance. The extinction spectra (Figure 7-2b) show that the resonance appears to be superimposed with a broader resonance centered at 630 nm.

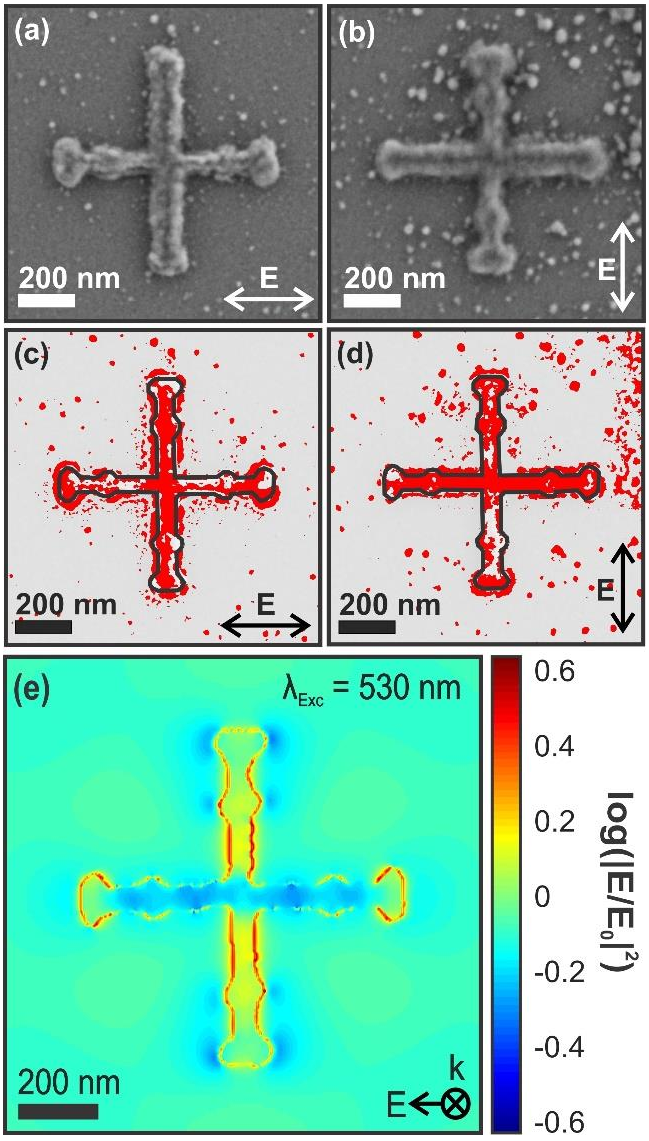

Figure 7-8 SEM images of the crosshairs after irradiation under a 532 nm laser both (a) horizontally and (b) vertically polarized. (c) and (d) are the colorized images of (a) and (b), respectively, with the outline of the cross in black as a guide for the eye. (e) FDTD modelling of the near-field distribution upon irradiation at 530 nm for the real structure with a horizontal polarization. Reference background image used to generate (c) and (d) is provided shown in the inset of Figure 7-5.

Shown in Figure 7-8a,b are the SEM images of individual nanostructures after irradiation in the presence of the diazonium solution with a horizontal and a vertical polarization, respectively. Figures 7-8c,d are treated images obtained by subtracting the bare non-

functionalized structure and that shows the spatial distribution of the polyaryl films. Both major arms appear to experience grafting yet with predominant grafting along the major arms that are orthogonal to the input polarization. In both case the gold structure is entirely covered by the polyaryl layers derived from the diazonium salt which appear thicker than when irradiated at 800 or 632.8 nm. Interestingly, the irradiation at 532 nm appears to induce polymerization on the substrate as well, as shown by the numerous aggregates located around the structures. The presence of such aggregates is not observed in any of the experiments performed at 632 nm and 800 nm. Presumably the presence of these aggregates over the gold structure and the glass surface is facilitated by spontaneous grafting enabled by the higher energy 532 nm photons that would yield more thermally induced decomposition and subsequent grafting through the cationic process.

The LSPR present at 532 nm originates from the width of the structures themselves (Figure 7-1a and Figure 7-8e), which is perpendicular to the irradiation polarization. This can be seen by the growth occurring on all the outer features, and predominantly on the entire arm, perpendicular to the irradiation polarization as highlighted in red in Figure 7-8a-d where the notches cannot be distinguished anymore since they are completely covered by the polyaryl layer.

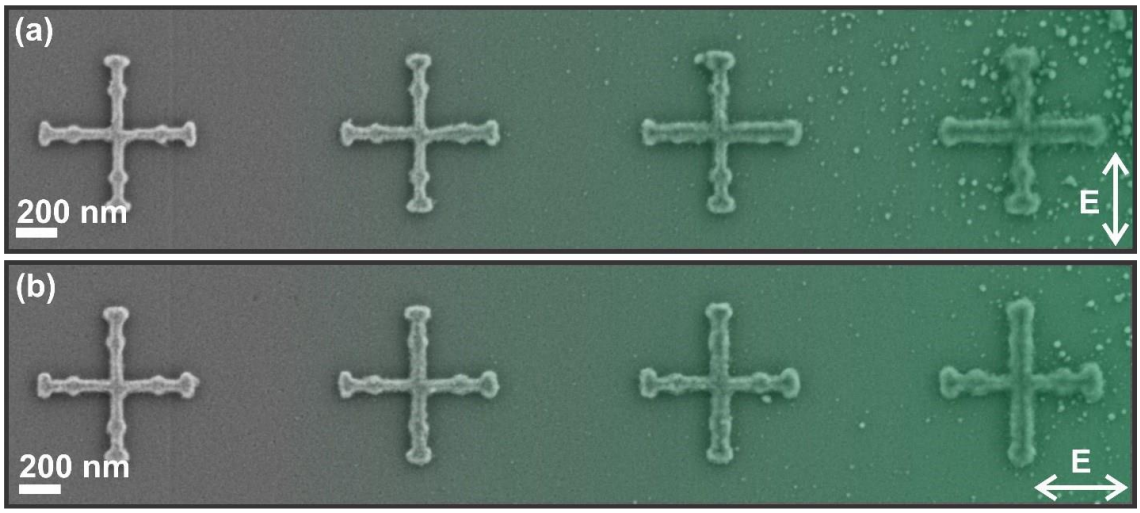

Figure 7-9 SEM images of the 532 nm irradiated crosshairs with a (a) vertical and (b) horizontal polarization with increasing laser intensity from left to right. The first structure on the left of (a,b) has not been irradiated as a reference.

The polarization dependent grafting demonstrates the effectiveness of the nanostructure's response upon irradiation. Shown in Figure 7-9 are a series of crosshair structures located at the edge of the irradiation beam polarized vertically (Figure 7-9a) and horizontally (Figure 7-9b) with intensity increasing from left to right.

The bare structures on the left-most of Figure 7-9a,b are out of the beam while it transitions to irradiation with the highest power on the right. These experiments show again that the major axes oriented perpendicular to the polarization of the impinging beam experience the most functionalization where the grafted molecules completely cover the major axis masking even the two smaller orthogonal notches.

The progression of the grafting across the surface indicates that the density of hot electrons generated upon irradiation at 532 nm are proportional to the energy dose. It can also be seen in these images that the structures on the left have no molecules adhered to either the surface of the structures, or the glass substrate itself. On the right, however, there is a large grafting visible on the structures as well as organic aggregates adsorbed on the surface. This demonstrates that all the grafting is occurring due to the irradiation, and not spontaneously. While the 532 nm grafting had the lowest irradiance of the three tests at 1.79×10^3 W/cm^2, the grafting was more prominent for equivalent irradiation times (60s). This is caused by the LSPR, which covers a larger surface area of the crosshair structure than the other two resonances, in synergy with the cationic process as evidenced by the numerous organic deposits observed at the surface of the glass coverslip closer to the center of the laser spot.

In summary, the different grafting patterns based on the irradiation wavelength are shown. The electromagnetic enhancement hotspots from the plasmon resonances play an important role when comparing these different grafting patterns. By changing the irradiation source as well as the polarization, molecules were grafted to specific areas of the surface. Although this chapter considers only a selected diazonium salt, there is potential to use these structures to graft up to six different molecules onto the same surface using three wavelengths and two polarization states. This versatility can be taken advantage of for molecular patterning. This opens new applications in molecular

electronics and biosensing where distinct grafted molecules within a nanoscale structure can display different functions.

7.4 Conclusion

Crosshair nanostructures with three plasmon resonances were designed and fabricated in order to facilitate plasmon-mediated reactions in the visible wavelength region. The structures were successfully employed for the surface specific grafting of a diazonium salt to the surface using wavelengths of 532 nm, 633 nm, and 800 nm. For each of the wavelengths, distinct grafting patterns can be observed around the structures. The polarization dependence of the grafting was also tested for these three wavelengths to which the structures responded according to the incident polarization. These nanostructures offer a platform for a multitude of applications in both chemistry and nanoscale surface patterning due to the possibility to spatially control the functionalization of distinct molecules with a selected set of wavelength and polarization. Based on this approach, multimodal platforms for combined SERS/SEF/SHGM can be developed to study target analytes with these techniques in parallel on a single platform such as the bioconjugation of different cells of interest could be developed.

7.5 References

1. Ong, T. T. X.; Blanch, E. W.; Jones, O. A. H., *Sci. Total. Environ.* **2020,** *720*, 137601.

2. Kurouski, D.; Dazzi, A.; Zenobi, R.; Centrone, A., *Chem. Soc. Rev.* **2020,** *49*, 3315-3347.

3. Wallace, G. Q.; Lagugné-Labarthet, F., *Analyst* **2019,** *144*, 13-30.

4. Zen, F.; Karanikolas, V. D.; Behan, J. A.; Andersson, J.; Ciapetti, G.; Bradley, A. L.; Colavita, P. E., *Langmuir* **2017,** *33*, 4198-4206.

5. Zhou, J.; Yang, T.; Chen, J.; Wang, C.; Zhang, H.; Shao, Y., *Coord. Chem. Rev.* **2020,** *410*, 213218.

6. Zhang, H.; Duan, S.; Radjenovic, P. M.; Tian, Z.-Q.; Li, J.-F., *Acc. Chem. Res.* **2020,** *53*, 729-739.

7. Sharifi, M.; Hosseinali, S. H.; Hossein Alizadeh, R.; Hasan, A.; Attar, F.; Salihi, A.; Shekha, M. S.; Amen, K. M.; Aziz, F. M.; Saboury, A. A.; Akhtari, K.; Taghizadeh, A.; Hooshmand, N.; El-Sayed, M. A.; Falahati, M., *Talanta* **2020,** *212*, 120782.

8. Wallace, G. Q.; Read, S. T.; McRae, D. M.; Rosendahl, S. M.; Lagugné-Labarthet, F., *Adv. Opt. Mater.* **2018,** *6*, 1701336.

9. Wallace, G. Q.; Foy, H. C.; Rosendahl, S. M.; Lagugné-Labarthet, F., *J. Phys. Chem. C* **2017,** *121*, 9497-9507.

10. Bareza, N., Jr.; Gopalan, K. K.; Alani, R.; Paulillo, B.; Pruneri, V., *ACS Photonics* **2020,** *7*, 879-884.

11. Li, J.-F.; Li, C.-Y.; Aroca, R. F., *Chem. Soc. Rev.* **2017,** *46*, 3962-3979.

12. Bauch, M.; Toma, K.; Toma, M.; Zhang, Q.; Dostalek, J., *Plasmonics* **2014,** *9*, 781-799.

13. Ming, T.; Zhao, L.; Yang, Z.; Chen, H.; Sun, L.; Wang, J.; Yan, C., *Nano Lett.* **2009,** *9*, 3896-3903.

14. Tavakkoli Yaraki, M.; Daqiqeh Rezaei, S.; Tan, Y. N., *Phys. Chem. Chem. Phys.* **2020,** *22*, 5673-5687.

15. Therien, D. A. B.; Hou, R.; Lagugné-Labarthet, F., *Plasmonics* **2020,** *15*, 507-515.

16. McRae, D. M.; Therien, D. A. B.; Hou, R.; Wallace, G. Q.; Lagugné-Labarthet, F., *ACS Appl. Nano. Mater.* **2020,** *3*, 3922-3929.

17. Lin, X.; Liu, Y.; Wang, K.; Wei, C.; Zhang, W.; Yan, Y.; Li, Y. J.; Yao, J.; Zhao, Y. S., *ACS Nano* **2018,** *12*, 689-696.

18. Butet, J.; Brevet, P.-F.; Martin, O. J. F., *ACS Nano* **2015,** *9*, 10545-10562.

19. Yu, S.; Jain, P. K., *Angew. Chem. Int. Edit.* **2020,** *59*, 2085-2088.

20. Ha, M.; Kim, J.-H.; You, M.; Li, Q.; Fan, C.; Nam, J.-M., *Chem. Rev.* **2019,** *119*, 12208-12278.

21. Bicket, I. C.; Bellido, E. P.; McRae, D. M.; Lagugné-Labarthet, F.; Botton, G. A., *ACS Photonics* **2019,** *6*, 2974-2984.

22. McRae, D. M.; Jeon, K.; Lagugné-Labarthet, F., *ACS Omega* **2018,** *3*, 7269-7277.

23. Pal, S.; Dutta, A.; Paul, M.; Chattopadhyay, A., *J. Phys. Chem. C* **2020,** *124*, 3204-3210.

24. Hetemi, D.; Noel, V.; Pinson, J., *Biosensors* **2020,** *10*, 4.

25. Wallentine, S.; Bandaranayake, S.; Biswas, S.; Baker, L. R., *J. Phys. Chem. A* **2020,** *124*, 8057-8064.

26. Lu, C.; Li, J.; Yan, J.; Li, B.; Huang, B.; Lou, Z., *Appl. Mater. Today.* **2020,** *20*, 100744.

27. Yu, S.; Jain, P. K., *Nature Commun.* **2019,** *10*, 2022.

28. Sang, Y.; Liu, B.; Tao, T.; Jiang, D.; Wu, Y.; Chen, X.; Luo, W.; Ye, J.; Zhang, R., *Semicond. Sci. Tech.* **2020,** *35*, 025017.

29. Huang, Y.-S.; Hsiao, Y.-C.; Tzeng, S.-H.; Wu, Y.-H.; Perng, T.-P.; Lu, M.-Y.; Chueh, Y.-L.; Chen, L.-J., *Nano Energy* **2020,** *77*, 105267.

30. Ghosh, D.; Roy, K.; Sarkar, K.; Devi, P.; Kumar, P., *ACS Appl. Mater. Inter.* **2020,** *12*, 28792-28800.

31. Kumar, D.; Park, C. H.; Kim, C. S., *J. Mater. Chem. A* **2020,** *8*, 5734-5743.

32. Tijunelyte, I.; Kherbouche, I.; Gam-Derouich, S.; Nguyen, M.; Lidgi-Guigui, N.; de la Chapelle, M. L.; Lamouri, A.; Lévi, G.; Aubard, J.; Chevillot-Biraud, A.; Mangeney, C.; Felidj, N., *Nanoscale Horiz.* **2018,** *3*, 53-57.

33. Zhou, X.; Wenger, J.; Viscomi, F. N.; Le Cunff, L.; Béal, J.; Kochtcheev, S.; Yang, X.; Wiederrecht, G. P.; Colas des Francs, G.; Bisht, A. S.; Jradi, S.; Caputo, R.; Demir, H. V.; Schaller, R. D.; Plain, J.; Vial, A.; Sun, X. W.; Bachelot, R., *Nano Lett.* **2015,** *15*, 7458-7466.

34. Gehan, H.; Fillaud, L.; Chehimi, M. M.; Aubard, J.; Hohenau, A.; Felidj, N.; Mangeney, C., *ACS Nano* **2010,** *4*, 6491-6500.

35. Wang, Y.; Wang, S.; Zhang, S.; Scherman, O. A.; Baumberg, J. J.; Ding, T.; Xu, H., *Nano Research* **2018,** *11*, 6384-6390.

36. Pinson, J.; Podvorica, F., *Chem. Soc. Rev.* **2005,** *34*, 429-439.

37. Mesnage, A.; Lefèvre, X.; Jégou, P.; Deniau, G.; Palacin, S., *Langmuir* **2012,** *28*, 11767-11778.

38. Nguyen, M.; Lamouri, A.; Salameh, C.; Levi, G.; Grand, J.; Boubekeur-Lecaque, L.; Mangeney, C.; Felidj, N., *Nanoscale* **2016,** *8*, 8633-8640.

39. Jayasundara, D. R.; Cullen, R. J.; Soldi, L.; Colavita, P. E., *Langmuir* **2011,** *27*, 13029-13036.

Chapter 8

8 Conclusions and Outlook

In this thesis, we have investigated the linear and nonlinear optical properties of metamaterials and transition metal dichalcogenides 2D materials. After a general introduction of the field of plasmon-enhanced SHG and plasmon-mediated chemistry theoretical descriptions are provided in Chapter 2. Therein, the principles of FDTD electromagnetic modelling and their applications to meta- and nanomaterials are described. The background on localized plasmon resonances and their link to metamaterials is introduced, followed by the fundamentals of nonlinear optics, with a focus on second-harmonic generation and its symmetry-based selection rules in crystals as well as in nano- and metamaterials. Finally, plasmon-mediated chemistry through hot-electron decay is described including examples of surface specific plasmon-mediated grafting on nanomaterials.

Following these introductory remarks, the experimental methods used throughout the thesis are described in detail. The FDTD modelling is thoroughly described, as it is a pivotal piece of information for Chapters 4, 6, and 7. The fabrication methods for the nano- and metamaterials used throughout the thesis, including nanosphere lithography, electron-beam lithography, and chemical vapor deposition as well as the characterization methods used, are described. This includes SEM, vis-NIR absorbance measurements, and SHGM. To tune the metamaterials' optical properties to specific wavelengths, key opto-geometric parameters are introduced and further discussed. Finally, the experimental setups for the plasmon-mediated chemistry in chapters 6 and 7 are detailed.

Once the background information was established, Chapters 4 and 5 are focusing on specific metamaterials and bulk materials that are both SHG-active. Chapter 4 elaborates on the inherent symmetry of a metamaterial and on its effect on the SHG activity. This includes the study of fractal-like dendrimer nanomaterials which are known to exhibit tunable LSPR modes ranging from the visible to the mid-infrared range.[1, 2] Furthermore, the effects of plasmon enhancement on these multibranched metamaterials are described according to the considered fractal generation.

Chapter 5 elaborates on the SHG activity of MoS_2 2D flakes. The polarized SHG response of these 2D materials is both mathematically described and measured experimentally. The MoS_2 flakes were also functionalized with an organic dye, and its effects on the intensity of the SHG signal are explained.

In Chapter 6, a single beam was used to create surface relief grating through the grafting of a diazonium salt to the surface of a bare glass substrate at different incident polarizations.[3] Following this approach, the same diazonium salt was further grafted to the surface of a metallic array of Au nanotriangles under distinct polarization conditions. This resulted in surface patterning where different structures were obtained. The plasmon-induced functionalization yielded the formation of structures of polyaryl resulting from the diazonium salts and promoted by the generation of hot electron through plasmon excitation.

The principles of plasmon-mediated chemistry are further expanded in Chapter 7, involving the crosshair metamaterials. These materials were designed to produce three distinct LSPR modes in the visible region which were then fabricated by EBL. The crosshair structures were tested at three different wavelengths, and the spatial distribution of the grafted polyaryl film was compared to the area of higher enhancement as anticipated by FDTD modelling.

There is a broad spectrum of applications of metamaterials, as described throughout this thesis. The FDTD calculations proved to be a practical method for modelling the LSPR modes of metamaterials prior to fabrication.[4] The crosshair metamaterials fabricated have the potential for multiplexing different patterns at the surface and offer a series of tunable LSPR modes which could be used in sensing technology.[4] As previously shown, multiplexing of different polymer formulations containing light-emitting quantum dots at the surface of a material is a promising pathway to surface specific light emissions.[5] Multiplexing three different quantum dots to the surface of the crosshair structures would be a logical follow-up experiment that opens up the possibility of collaborations with groups working on either electron-sensitive polymers or light-emitting quantum dots. Another practical application explored within the Lagugné-Labarthet's group is the

trapping and characterization of biological samples using nanohole arrays. These studies involve a device with nanoscale holes in them that are used to trap, characterize, and differentiate healthy and cancerous exosomes excreted from cells.[6-9]

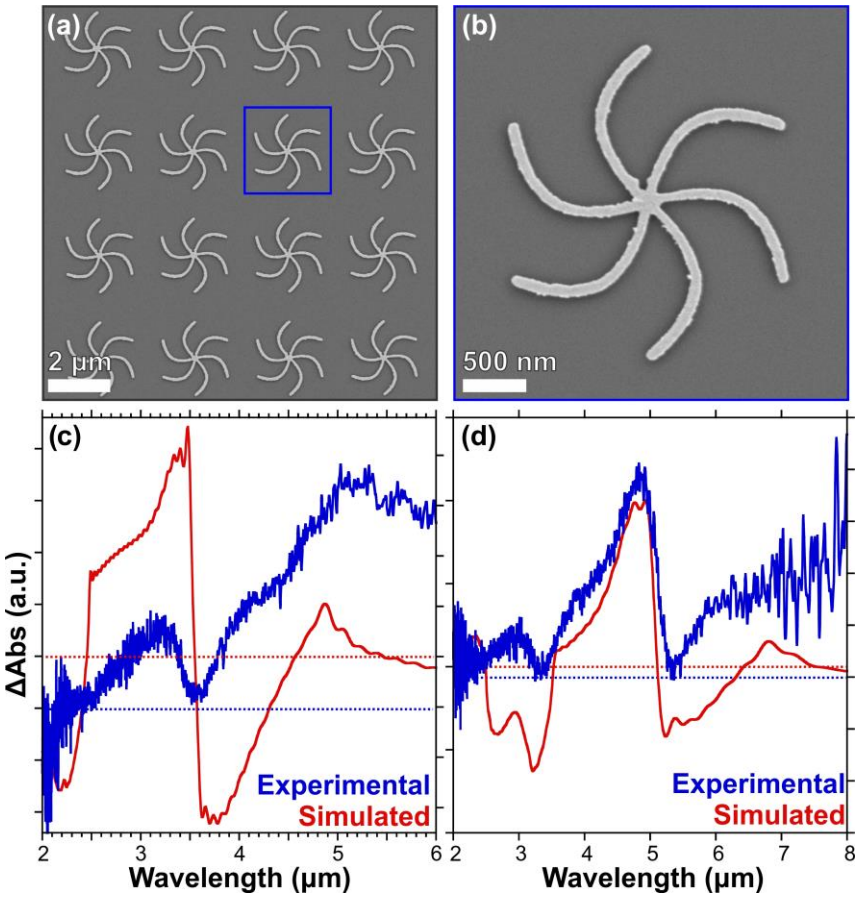

Figure 8-1 (a) A scanning electron micrograph of an array of truncated spiral structures and with an individual structure (highlighted in blue) shown in (b). (c) and (d) shows the simulated (red) and experimental (blue) ΔAbs spectra for a truncated spiral structure with a diameter of 2.5 and 4 μm, respectively (Manuscript accepted in the Journal of Israel Chemistry: Therien, D. A. B.; Read, S. T.; Rosendahl, S. M.; Lagugné-Labarthet, F., Isr. J. Chem. 2022. https://doi.org/10.1002/ijch.202200007) © 2022 WILEY-VCH Verlag GmbH & Co. KGaA, Weinheim.

Another application of metamaterials includes the development of chiral structures that will respond differently depending on the handedness of a circularly polarized light. The

chiral metamaterials shown in Figure 8-1 were modelled using the FDTD method prior to fabrication. The spirals were fabricated by EBL and the resulting circular dichroism was measured at the mid-infrared beamline of the Canadian Light Source in Saskatoon, SK, Canada.

The current interest for plasmonic metamaterials and plasmon-mediated chemistry is still a very fertile research field as demonstrated by the consistently number of manuscripts published in chemistry and physics journals. The understanding of the fundamentals of plasmonics is continually expanding and has shown great potential for applications. This encompasses applications in a variety of fields in chemistry, such as sensing,[10, 11] surface chemistry,[12, 13] optics,[14, 15] and more.[16-18] The exploration of these applications has already shown significant improvement since its inception, with more improvements being published each day.[19-21]

8.1 References

1. Therien, D. A. B.; Hou, R.; Lagugné-Labarthet, F., *Plasmonics* **2020,** *15*, 507-515.

2. Wallace, G. Q.; McRae, D. M.; Lagugné-Labarthet, F., *Opt. Lett.* **2019,** *44*, 3865-3868.

3. Therien, D. A. B.; Ćulum, N. M.; McRae, D. M.; Mazaheri, L.; Lagugné-Labarthet, F., *Opt. Mater.* **2021,** *112*, 110775.

4. Therien, D. A. B.; McRae, D. M.; Mangeney, C.; Félidj, N.; Lagugné-Labarthet, F., *Nanoscale Adv.* **2021,** *3*, 2501-2507.

5. Zhou, X.; Wenger, J.; Viscomi, F. N.; Le Cunff, L.; Béal, J.; Kochtcheev, S.; Yang, X.; Wiederrecht, G. P.; Colas des Francs, G.; Bisht, A. S.; Jradi, S.; Caputo, R.; Demir, H. V.; Schaller, R. D.; Plain, J.; Vial, A.; Sun, X. W.; Bachelot, R., *Nano Lett.* **2015,** *15*, 7458-7466.

6. Ćulum, N. M.; Cooper, T. T.; Lajoie, G. A.; Dayarathna, T.; Pasternak, S. H.; Liu, J.; Fu, Y.; Postovit, L.-M.; Lagugné-Labarthet, F., *Analyst* **2021,** *146*, 7194-7206.

7. Ćulum, N. M.; Cooper, T. T.; Bell, G. I.; Hess, D. A.; Lagugné-Labarthet, F., *Anal. Bioanal. Chem.* **2021,** *413*, 5013-5024.

8. Kaufman, L.; Cooper, T.; Wallace, G.; Hawke, D.; Betts, D.; Hess, D.; Lagugné-Labarthet, F., *Trapping and SERS identification of extracellular vesicles using nanohole arrays*. SPIE: 2019; Vol. 10894.

9. Gomes, J.; Lucien, F.; Cooper, T. T.; Kim, Y.; Williams, K. C.; Liao, X.; Kaufman, L.; Lagugné-Labarthet, F.; Kenyon, O.; Boysen, J.; Kay, N. E.; McIntyre, C. W.; Leong, H. S., *Thromb. Haemost.* **2018,** *118*, 1612-1624.

10. Liu, Y.; Peng, W., *J. Light. Technol.* **2021,** *39*, 3781-3791.

11. Yesudasu, V.; Pradhan, H. S.; Pandya, R. J., *Heliyon* **2021,** *7*, e06321.

12. Stewart, S.; Wei, Q.; Sun, Y., *Chem. Sci.* **2021,** *12*, 1227-1239.

13. Su, Q.; Jiang, C.; Gou, D.; Long, Y., *ACS Appl. Bio Mater.* **2021,** *4*, 4684-4705.

14. Philip, A.; Kumar, A. R., *Coord. Chem. Rev.* **2022,** *458*, 214424.

15. Shi, J.; Guo, Q.; Shi, Z.; Zhang, S.; Xu, H., *Appl. Phys. Lett.* **2021,** *119*, 130501.

16. Balitskii, O. A., *Mater. Today Energy* **2021,** *20*, 100629.

17. Ravindran, N.; Kumar, S.; M, Y.; S, R.; C A, M.; Thirunavookarasu S, N.; C K, S., *Crit. Rev. Food Sci. Nutr.* **2021**, 1-23.

18. Wang, Q.; Liu, Z., *Eur. J. Med. Chem. Rep.* **2021,** *1*, 100003.

19. Alharbi, R.; Irannejad, M.; Yavuz, M., *Sensors* **2019,** *19*, 862.

20. Hou, W.; Cronin, S. B., *Adv. Funct. Mater.* **2013,** *23*, 1612-1619.

21. Hoa, X. D.; Kirk, A. G.; Tabrizian, M., *Biosens. Bioelectron.* **2007,** *23*, 151-160.

Appendix A: Copyrights and Permissions

Appendix A: Copyrights and permissions granted from their respective holders.

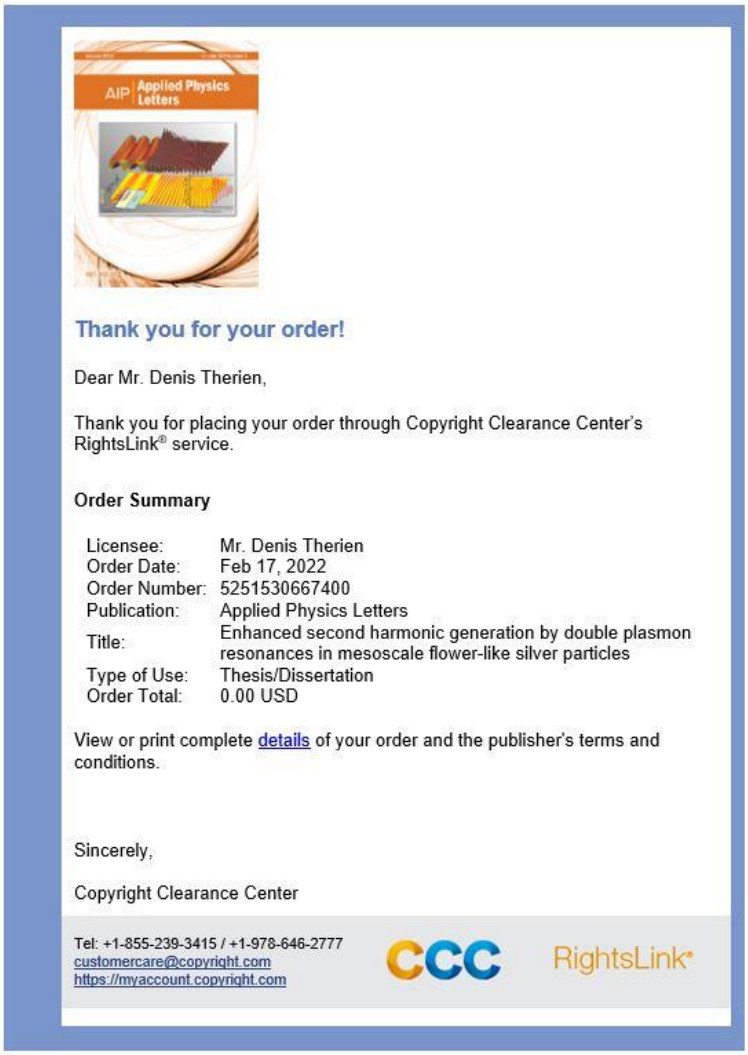

ACS Publications
Most Trusted. Most Cited. Most Read.

Second Harmonic Generation from Artificially Stacked Transition Metal Dichalcogenide Twisted Bilayers

Author: Wei-Ting Hsu, Zi-Ang Zhao, Lain-Jong Li, et al
Publication: ACS Nano
Publisher: American Chemical Society
Date: Mar 1, 2014

Copyright © 2014, American Chemical Society

PERMISSION/LICENSE IS GRANTED FOR YOUR ORDER AT NO CHARGE

This type of permission/license, instead of the standard Terms and Conditions, is sent to you because no fee is being charged for your order. Please note the following:

- Permission is granted for your request in both print and electronic formats, and translations.
- If figures and/or tables were requested, they may be adapted or used in part.
- Please print this page for your records and send a copy of it to your publisher/graduate school.
- Appropriate credit for the requested material should be given as follows: "Reprinted (adapted) with permission from {COMPLETE REFERENCE CITATION}. Copyright {YEAR} American Chemical Society." Insert appropriate information in place of the capitalized words.
- One-time permission is granted only for the use specified in your RightsLink request. No additional uses are granted (such as derivative works or other editions). For any uses, please submit a new request.

If credit is given to another source for the material you requested from RightsLink, permission must be obtained from that source.

BACK CLOSE WINDOW

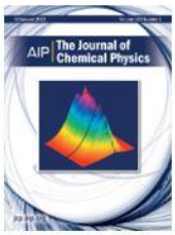

Thank you for your order!

Dear Mr. Denis Therien,

Thank you for placing your order through Copyright Clearance Center's RightsLink® service.

Order Summary

Licensee:	Mr. Denis Therien
Order Date:	Feb 17, 2022
Order Number:	5251530244807
Publication:	Journal of Chemical Physics
Title:	Multiband enhanced second-harmonic generation via plasmon hybridization
Type of Use:	Thesis/Dissertation
Order Total:	0.00 CAD

View or print complete details of your order and the publisher's terms and conditions.

Sincerely,

Copyright Clearance Center

Tel: +1-855-239-3415 / +1-978-646-2777
customercare@copyright.com
https://myaccount.copyright.com

CCC RightsLink®

ACS Publications
Most Trusted. Most Cited. Most Read.

Mapping the Electromagnetic Near-Field Enhancements of Gold Nanocubes

Author: Claire Deeb, Xuan Zhou, Ryan Miller, et al
Publication: The Journal of Physical Chemistry C
Publisher: American Chemical Society
Date: Nov 1, 2012

Copyright © 2012, American Chemical Society

PERMISSION/LICENSE IS GRANTED FOR YOUR ORDER AT NO CHARGE

This type of permission/license, instead of the standard Terms and Conditions, is sent to you because no fee is being charged for your order. Please note the following:

- Permission is granted for your request in both print and electronic formats, and translations.
- If figures and/or tables were requested, they may be adapted or used in part.
- Please print this page for your records and send a copy of it to your publisher/graduate school.
- Appropriate credit for the requested material should be given as follows: "Reprinted (adapted) with permission from {COMPLETE REFERENCE CITATION}. Copyright {YEAR} American Chemical Society." Insert appropriate information in place of the capitalized words.
- One-time permission is granted only for the use specified in your RightsLink request. No additional uses are granted (such as derivative works or other editions). For any uses, please submit a new request.

If credit is given to another source for the material you requested from RightsLink, permission must be obtained from that source.

BACK CLOSE WINDOW

ACS Publications
Most Trusted. Most Cited. Most Read.

Two-Color Single Hybrid Plasmonic Nanoemitters with Real Time Switchable Dominant Emission Wavelength

Author: Xuan Zhou, Jérémie Wenger, Francesco N. Viscomi, et al
Publication: Nano Letters
Publisher: American Chemical Society
Date: Nov 1, 2015

Copyright © 2015, American Chemical Society

PERMISSION/LICENSE IS GRANTED FOR YOUR ORDER AT NO CHARGE

This type of permission/license, instead of the standard Terms and Conditions, is sent to you because no fee is being charged for your order. Please note the following:

- Permission is granted for your request in both print and electronic formats, and translations.
- If figures and/or tables were requested, they may be adapted or used in part.
- Please print this page for your records and send a copy of it to your publisher/graduate school.
- Appropriate credit for the requested material should be given as follows: "Reprinted (adapted) with permission from {COMPLETE REFERENCE CITATION}. Copyright {YEAR} American Chemical Society." Insert appropriate information in place of the capitalized words.
- One-time permission is granted only for the use specified in your RightsLink request. No additional uses are granted (such as derivative works or other editions). For any uses, please submit a new request.

If credit is given to another source for the material you requested from RightsLink, permission must be obtained from that source.

BACK CLOSE WINDOW

ACS Publications
Most Trusted. Most Cited. Most Read.

Mapping Photoemission and Hot-Electron Emission from Plasmonic Nanoantennas

Author: Richard G. Hobbs, William P. Putnam, Arya Fallahi, et al
Publication: Nano Letters
Publisher: American Chemical Society
Date: Oct 1, 2017

Copyright © 2017, American Chemical Society

PERMISSION/LICENSE IS GRANTED FOR YOUR ORDER AT NO CHARGE

This type of permission/license, instead of the standard Terms and Conditions, is sent to you because no fee is being charged for your order. Please note the following:

- Permission is granted for your request in both print and electronic formats, and translations.
- If figures and/or tables were requested, they may be adapted or used in part.
- Please print this page for your records and send a copy of it to your publisher/graduate school.
- Appropriate credit for the requested material should be given as follows: "Reprinted (adapted) with permission from {COMPLETE REFERENCE CITATION}. Copyright {YEAR} American Chemical Society." Insert appropriate information in place of the capitalized words.
- One-time permission is granted only for the use specified in your RightsLink request. No additional uses are granted (such as derivative works or other editions). For any uses, please submit a new request.

If credit is given to another source for the material you requested from RightsLink, permission must be obtained from that source.

BACK CLOSE WINDOW

ACS Publications
Most Trusted. Most Cited. Most Read.

Optical Second Harmonic Generation in Plasmonic Nanostructures: From Fundamental Principles to Advanced Applications

Author: Jérémy Butet, Pierre-François Brevet, Olivier J. F. Martin
Publication: ACS Nano
Publisher: American Chemical Society
Date: Nov 1, 2015

Copyright © 2015, American Chemical Society

PERMISSION/LICENSE IS GRANTED FOR YOUR ORDER AT NO CHARGE

This type of permission/license, instead of the standard Terms and Conditions, is sent to you because no fee is being charged for your order. Please note the following:

- Permission is granted for your request in both print and electronic formats, and translations.
- If figures and/or tables were requested, they may be adapted or used in part.
- Please print this page for your records and send a copy of it to your publisher/graduate school.
- Appropriate credit for the requested material should be given as follows: "Reprinted (adapted) with permission from {COMPLETE REFERENCE CITATION). Copyright {YEAR} American Chemical Society." Insert appropriate information in place of the capitalized words.
- One-time permission is granted only for the use specified in your RightsLink request. No additional uses are granted (such as derivative works or other editions). For any uses, please submit a new request.

If credit is given to another source for the material you requested from RightsLink, permission must be obtained from that source.

BACK CLOSE WINDOW

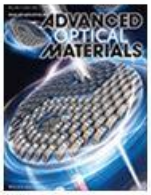

Thank you for your order!

Dear Mr. Denis Therien,

Thank you for placing your order through Copyright Clearance Center's RightsLink® service.

Order Summary

Licensee:	Mr. Denis Therien
Order Date:	Feb 17, 2022
Order Number:	5251541152191
Publication:	Advanced Optical Materials
Title:	Second Harmonic Generation Manipulation Enabled by Electromagnetic Coupling in Bianisotropic Metamolecules
Type of Use:	Dissertation/Thesis
Order Total:	0.00 CAD

View or print complete details of your order and the publisher's terms and conditions.

Sincerely,

Copyright Clearance Center

Tel: +1-855-239-3415 / +1-978-646-2777
customercare@copyright.com
https://myaccount.copyright.com

CCC RightsLink®

ACS Publications
Most Trusted. Most Cited. Most Read.

Nanosphere Lithography: A Versatile Nanofabrication Tool for Studies of Size-Dependent Nanoparticle Optics

Author: Christy L. Haynes, Richard P. Van Duyne
Publication: The Journal of Physical Chemistry B
Publisher: American Chemical Society
Date: Jun 1, 2001

Copyright © 2001, American Chemical Society

PERMISSION/LICENSE IS GRANTED FOR YOUR ORDER AT NO CHARGE

This type of permission/license, instead of the standard Terms and Conditions, is sent to you because no fee is being charged for your order. Please note the following:

- Permission is granted for your request in both print and electronic formats, and translations.
- If figures and/or tables were requested, they may be adapted or used in part.
- Please print this page for your records and send a copy of it to your publisher/graduate school.
- Appropriate credit for the requested material should be given as follows: "Reprinted (adapted) with permission from {COMPLETE REFERENCE CITATION}. Copyright {YEAR} American Chemical Society." Insert appropriate information in place of the capitalized words.
- One-time permission is granted only for the use specified in your RightsLink request. No additional uses are granted (such as derivative works or other editions). For any uses, please submit a new request.

If credit is given to another source for the material you requested from RightsLink, permission must be obtained from that source.

BACK CLOSE WINDOW

SPRINGER NATURE

Thank you for your order!

Dear Mr. Denis Therien,

Thank you for placing your order through Copyright Clearance Center's RightsLink® service.

Order Summary

Licensee:	Mr. Denis Therien
Order Date:	Feb 17, 2022
Order Number:	5251551424045
Publication:	Plasmonics
Title:	Second-Harmonic Generation from Dendritic Fractal Structures
Type of Use:	Thesis/Dissertation
Order Total:	0.00 USD

View or print complete details of your order and the publisher's terms and conditions.

Sincerely,

Copyright Clearance Center

Tel: +1-855-239-3415 / +1-978-646-2777
customercare@copyright.com
https://myaccount.copyright.com

CCC RightsLink®

ACS Chemistry for Life®

Short Description: Rights and Permissions

Priority: 3 - Moderate

Click here to view the case: LINK

Comments:

02-20-2022 07:21:37 PM EST - Simran Mehra Additional comments
Please note the below mentioned email was sent to you.

Dear Denis Therien,

Your permission requested is granted and there is no fee for this reuse. In your planned reuse, you must cite the ACS article as the source, add this direct link https://pubs.acs.org/doi/10.1021/acs.chemmater.5b00986 and include a notice to readers that further permissions related to the material excerpted should be directed to the ACS.

If you need further assistance, please let me know.

Best regards,
Simran Mehra

Simran Mehra
ACS Publications Support
Customer Services & Information
Website: https://acs.service-now.com/acs
Email: support@services.acs.org
Phone: 800-227-9919 | 202-872-(HELP) 4357

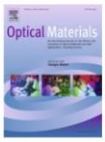

Single-beam inscription of plasmon-induced surface gratings

Author: Denis A.B. Therien,Nina M. Ćulum,Danielle M. McRae,Leila Mazaheri,François Lagugné-Labarthet
Publication: Optical Materials
Publisher: Elsevier
Date: February 2021

© 2020 Elsevier B.V. All rights reserved.

Journal Author Rights

Please note that, as the author of this Elsevier article, you retain the right to include it in a thesis or dissertation, provided it is not published commercially. Permission is not required, but please ensure that you reference the journal as the original source. For more information on this and on your other retained rights, please visit: https://www.elsevier.com/about/our-business/policies/copyright#Author-rights

BACK CLOSE WINDOW

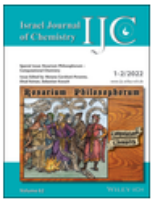

Thank you for your order!

Dear Mr. Denis Therien,

Thank you for placing your order through Copyright Clearance Center's RightsLink® service.

Order Summary

Licensee:	Mr. Denis Therien
Order Date:	Apr 25, 2022
Order Number:	5296210354530
Publication:	Israel Journal of Chemistry
Title:	Optical Resonances of Chiral Metastructures in the Mid-infrared Spectral Range
Type of Use:	Dissertation/Thesis
Order Total:	0.00 CAD

View or print complete details of your order and the publisher's terms and conditions.

Sincerely,

Copyright Clearance Center

Tel: +1-855-239-3415 / +1-978-646-2777
customercare@copyright.com
https://myaccount.copyright.com

RightsLink®

Curriculum Vitae

Name: Denis Alexander Brian Therien

Education

05/2018 – Present	Doctor of Philosophy candidate in Physical and Analytical Chemistry *University of Western Ontario, London, ON* Thesis supervisor: Prof. François Lagugné-Labarthet Scope of thesis: Simulating, designing, and fabricating nanomaterials by electron-beam lithography for plasmon-based linear and nonlinear applications. Expected to defend in April 2022.
05/2017 – 04/2018	Master of Science candidate in Physical and Analytical Chemistry *University of Western Ontario, London, ON* Thesis supervisor: Prof. François Lagugné-Labarthet Degree not conferred; fast-tracked to Ph.D.
09/2012 – 04/2017	Honours Bachelor of Science in Chemistry, Co-op option *University of Ottawa, Ottawa, ON* Thesis supervisor: Prof. Eva Hemmer Scope of thesis: Synthesizing inorganic nanomaterials that incorporate rare earth metals for solar cell-based applications.

Graduated *Cum Laude.*

Related Work experience

09/2017 – 12/2021 **Graduate Teaching Assistant**

University of Western Ontario, London, ON

Related Honours and Awards

11/2021 Outstanding Poster Prize

Ryerson University, Toronto, ON

06/2021 Microscopical Society of Canada - Microscopy Imaging Competition (1st place)

McMaster University, Hamilton, ON

04/2020 NSERC Post-Graduate Scholarship - Doctoral (PGS D)

University of Western Ontario, London, ON

04/2020 Ontario Graduate Scholarship

University of Western Ontario, London, ON

11/2019 Poster Prize (2nd place)

York University, Toronto, ON

Publications

6. **Therien, D.A.B.**; Lagugné-Labarthet, F. Optical Resonances of Chiral Metastructures in the Mid-infrared Spectral Range. *Isr. J. Chem.* (Accepted: ijch.202200007.)

5. **Therien, D.A.B.**; McRae, D.M.; Mangeney, C.; Félidj, N.; Lagugné-Labarthet, F. Three-Color Plasmon-Mediated Reduction of Diazonium Salts over Metasurfaces. *Nanoscale Adv.* 2021, *3*, 2501-2507. DOI: 10.1039/d0na00862a.

4. **Therien, D.A.B.**; Ćulum, N.M.; McRae, D.M.; Mazaheri, L.; Lagugné-Labarthet, F. Single-Beam Inscription of Plasmon-Induced Surface Gratings. *Opt. Mater.* 2021, *112*, 110775. DOI: 10.1016/j.optmat.2020.110775.

3. McRae, D.M.; **Therien, D.A.B.**; Hou, R.; Wallace, G.Q.; Lagugné-Labarthet, F. Sierpiński Fractals as Plasmonic Metastructures for Second-Harmonic Generation. *ACS Appl. Nano. Mater.* 2020, *3*, 3922-3929. DOI: 10.1021/acsanm.0c00711.

2. **Therien, D.A.B.**; Hou, R.; Lagugné-Labarthet, F. Second-Harmonic Generation from Dendritic Fractal Structures. *Plasmonics* 2020, *15*, 507-515. DOI: 10.1007/s11468-019-01080-y.

1. Cappello, D.; **Therien, D.A.B.**; Staroverov, V.N.; Lagugné-Labarthet, F.; Gilroy, J.B. Optoelectronic, Aggregation, and Redox Properties of Double-Rotor Boron Difluoride Hydrazone Dyes. *Chem. Eur. J.* 2019, *25*, 5994-6006. DOI: 10.1002/chem.201900383.

Presentations:

Oral:

5. **Therien, D.A.B.**; Farhat, P.; Lagugné-Labarthet, F. (2021) Second-Harmonic Generation of Dye Sensitized MoS_2 Flakes. Canadian Chemistry Conference and Exhibition, Virtual Event, Montreal, QC, Canada.

4. **Therien, D.A.B.**; McRae, D.M.; Lagugné-Labarthet, F. (2020) Plasmon-Mediated Reduction of Diazonium Salts in Gold Nanostructures. Microscopical Society of Canada Virtual Conference, Sherbrooke University, Sherbrooke, QC, Canada.

3. **Therien, D.A.B.**; McRae, D.M.; Lagugné-Labarthet, F. (2019) Surface-Specific Chemistry: Plasmon-Mediated Reduction Reactions. Electrochemical Society Student Symposium, University of Western Ontario, London, ON, Canada.

2. **Therien, D.A.B.**; McRae, D.M.; Ireland-Adkin, C.; Lagugné-Labarthet, F. (2019) Plasmon-Mediated Reduction of Diazonium Salts on Metallic Metastructures. 10th Annual Nano Ontario Conference, York University, Toronto, ON, Canada.

1. **Therien, D.A.B.**; Hemmer, E. (2016) Thèse en 3 Minutes : Conversion Additive Rouge et Vert par des Nanostructures de TiO2 Dopé avec des Lanthanides comme Candidat pour des Applications Solaires. 28e Colloque de Chimie de L'Université de Sherbrooke, Sherbrooke University, Sherbrooke, QC, Canada.

Poster:

9. **Therien, D.A.B.**; McRae, D.M.; Lagugné-Labarthet, F. (2021) Enhanced Nonlinear Optical Response of Dye-Sensitized MoS_2 Monolayer Flakes. 11th Annual Nano Ontario Conference, Ryerson University, Toronto, ON, Canada (Virtual).

8. **Therien, D.A.B.**; Farhat, P.; Lagugné-Labarthet, F. (2021) Dye-Sensitized Transition Metal Dichalcogenides for Enhanced Optical Processes. Center for Advanced Materials and Biomaterials Research Symposium, University of Western Ontario, London, ON (Virtual).

7. **Therien, D.A.B.**; Farhat, P.; Lagugné-Labarthet, F. (2021) Second-Harmonic Generation of Dye Sensitized MoS_2 Flakes. Microscopical Society of Canada Virtual Conference, McMaster University, Hamilton, ON (Virtual).

6. **Therien, D.A.B.**; Farhat, P.; Lagugné-Labarthet, F. (2020) Plasmon-Mediated Reduction of Diazonium Salts Using Gold Nanostructures. 47th Annual Conference of Federation of Analytical Chemistry and Spectroscopy Studies, Reno, NV (Virtual).

5. **Therien, D.A.B.**; McRae, D.M.; Ireland-Adkin, C.; Lagugné-Labarthet, F. (2019) Plasmon-Mediated Reduction of Diazonium Salts on Metallic Metastructures. 10th Annual Nano Ontario Conference, York University, Toronto, ON, Canada.

4. **Therien, D.A.B.**; Lagugné-Labarthet, F. (2019) Second-Harmonic Generation in Dendritic Fractals Functionalized with a Diazonium Salts. 4th International Conference

on Enhanced Spectroscopies (ICES), University of Western Ontario, London, ON, Canada.

3. **Therien, D.A.B.**; Lagugné-Labarthet, F. (2019) Nonlinear Optical Microscopy of Functionalized Fractal Metastructures. 102nd Canadian Chemistry Conference and Exhibition (CCCE), Québec City, QC, Canada.

2. **Therien, D.A.B.**; Lagugné-Labarthet, F. (2019) Nonlinear Optical Microscopy of Fractal Metastructures. Center for Advanced Materials and Biomaterials Research (CAMBR) Symposium, University of Western Ontario, London, ON, Canada.

1. **Therien, D.A.B.**; Lagugné-Labarthet, F. (2018) Nonlinear Optical Microscopy of Fractal Metastructures. 9th Annual Nano Ontario Conference, Carleton University, Ottawa, ON, Canada.